Morphodynamics of Ebb-Tidal Deltas

A thesis
submitted in fulfilment
of the requirements for the degree
of
Doctor of Philosophy
in
Earth Sciences
at
The University of Waikato
by
Shawn Robert Harrison

THE UNIVERSITY OF
WAIKATO
Te Whare Wānanga o Waikato

2015

Abstract

The purpose of this study was to learn more about the significant drivers of ebb-tidal delta morphology using observational methods and fundamental physical relationships between forcing conditions and morphological response. Two techniques were adapted in a novel way to study the dynamics of geomorphic features at an ebb-tidal delta. A 5-year long record of video imagery was used to observe a natural mixed-energy ebb-tidal delta in the field. A semi-analytical ebb-jet model, which was coupled to an exploratory morphological model, was developed and used to explore the interactions between tidal currents, waves, and morphology, and to test the sensitivity of morphological development and response to changes in forcing conditions.

A detailed video-based observational record was used to identify and track geomorphic features over 5 years at an ebb-tidal delta on the energetic west coast of New Zealand at Raglan by using depth-limited wave-breaking patterns as a proxy for the position of shallow sandbars. Oblique 20-minute averaged time-exposure images were geo-rectified to provide detailed spatial measurements of ebb-tidal delta features such as the terminal lobe, mouth bar, channel margin linear bars (or levees), and swash bars over the 5-year duration. Movements of these features were quantified and related to wave and tidal forcing, including seasonal and interannual trends in wave climate. In general, the low-energy restorative summer waves led to a more cuspate terminal lobe, while in the high-energy erosive winter waves straightened the terminal lobe and moved it further seaward than the long-term average. Movements throughout the delta were intermittent between less active periods, with the fastest swash bar migrations occurring during the transition between seasons, namely winter to spring and summer to autumn.

A semi-analytical model for ebbing tidal jet flow was developed based on the balance of momentum between inertia, bed friction, turbulent mixing, and wave effects. Previous analytical jet models (*Özsoy and Ünlüata*,

1982; *Joshi*, 1982) were extended to include the effects of directly opposing breaking waves. The model was calibrated and compared with scaled laboratory measurements (*Ismail and Wiegel*, 1983) and numerical simulations (*Nardin et al.*, 2013) of river jets flowing over flat bathymetry with non-breaking waves, and with detailed field measurements of jet flow and wave dissipation at New River Inlet, North Carolina (e.g. *Wargula et al.*, 2014). The jet model demonstrated the influence of opposing breaking waves on ebb-jet currents and jet width, along with the emergence of a point of flow convergence. The contribution of wave effects to the momentum balance were shown to impact the rapid slowing of jet flow, overall extent of an ebb-jet, and increase the jet width agreeing with previous studies (*Nardin and Fagherazzi* 2012; *Nardin et al*., 2013; *Olabarrietta et al*., 2014). Using a channelization parameter to emulate the ability of channel levees to constrain jet spreading, the model was calibrated over nine and validated over sixty-one ebb-events, respectively, to flow and wave measurements at New River Inlet. The model predicted the jet conditions well, receiving an overall excellent skill score. However, the model over-predicted the dissipative effects to jet flow of depth-limited wave breaking over the shallow ebb-shoal. The calibrated friction coefficient was roughly an order of magnitude higher than measured in the field, suggesting that the friction term was absorbing underrepresented processes. Pressure gradient was a neglected process identified as potentially significant, but was effectively included in the jet spreading term.

The jet model was coupled to sediment transport formulae to form an exploratory type morphological model for exploring the sensitivities of ebb-tidal shoal and channel morphology to changes in forcing conditions and sediment characteristics. Equilibrium ebb-shoal morphology was formed over many model iterations and shown to be morphologically dependent on forcing conditions. Wave-dominant conditions developed ebb-shoals in closer proximity to the tidal inlet, with wider channels at their seaward end, than jet-dominant conditions. Increases in jet velocity increased the rate of development of the delta more than did increases in wave height. Sediment characteristics had very little influence on the equilibrium

morphology, but did influence the rate of development. Short-term morphological responses of established morphology were sensitive to the initial channel width, with wide channels being most susceptible to the effects of waves and jet interaction. A double-barred ebb-shoal was shown to develop under mixed-energy conditions, with a shoreward bar being influenced by jet-flow and the seaward bar being influenced by wave breaking.

The observational data and modelling tools are used to explore ebb-tidal delta morphodynamics. Themes include the dependence on environmental conditions, transitions from equilibrium, and the competing influence of jet currents and opposing waves on ebb-shoal and channel morphology. The work asserts that ebb-tidal delta morphology forms as a result of dynamic balance between the dominant forces responsible for sediment transport, namely the ebbing tidal jet currents and opposing waves.

Forward

During Christmas holidays in 2004, something new came to my attention. I was living in Raglan, New Zealand, at the time and familiar with the excited faces of drippy-haired surfers recently returned to town from the local point-break or beach. But this time, there was something different happening. Between the indistinguishable colloquial surfer lingo and excited but hushed murmurs typical of someone trying to keep a secret, I could make out the words, "…the Bar is pumping!" I had been around Raglan long enough to know that there was a large accumulation of sand seaward of the entrance to the harbour, and that the locals referred to it as 'The Bar', so I went to the lookout to see what I could see. Waves break on the Bar almost every day and usually would break too quickly for surfing, but this time they were different. This time, countless lines of well-organized ground-swell approached at $18\text{-}20\ \mathrm{s}$ period and started breaking one by one along the shallow sandbars on the southern half of the Bar (Figure F.1). The sandbars at the Bar had moved into a position such that these plunging breakers peeled slowly enough along the crest of waves to allow for perfect surfing conditions. Looking closely, surfers were riding inside double-overhead sized barrelling waves with rides lasting over $800\ \mathrm{m}$. The sandbars remained surfable in this position for a few weeks after which the surfability deteriorated as the sandbars moved. I share this story not because I was interested in the surf, but because it was this event that initially motivated me to undertake this research. I was interested in understanding more about how and why these sandbar features move into various arrangements, and try to find order in a system that seemed mysterious and unknown.

Figure F.1. Waves breaking at the Raglan Bar on Boxing Day 2004 (photo courtesy of Aussie Pete).

Acknowledgements

Special thanks to Karin Bryan and Julia Mullarney for the weekly meetings and special attention. Thank you for guidance, encouragement, and patience. Direction was also kindly provided by Willem de Lange and Christian Winter whom shared their great knowledge.

Financial support made this research possible, for which I am grateful. The University of Waikato Doctoral Scholarship and the INTERCOAST Scholarship enabled me to live. The New Zealand Coastal Society Student Award and the Broad Memorial Award helped with field work expenses and made life more comfortable. The Terry Healy Memorial Award enabled me to present this research at a conference in Hawaii, and a travel grant from the Ministry of Research, Science and Technology (MoRST) allowed me to study for 3 months in Germany.

Dirk Immenga and Dean Sandwell provided field assistance at Raglan. It was great to learn new techniques from such skilled and thorough technicians. Also, I am thankful for the chance to join Declan Stubbing and Jimmy Van Der Pauw (Discovery Marine Limited) during the multibeam hydrographic survey of the Raglan Bar and Harbour. Thanks to Ed Atkin for shuttling us across the harbour with loads of bamboo and survey equipment, and to François Gabarrot for assistance gathering ground control points along the northern beaches.

Waikato Regional Council provided funding and access to bathymetry data, water level data, and the Raglan Cam-Era video data, for which I am very grateful. Thank you for your trust and helpfulness.

Thanks to Alex Port for always being present and willing to help others, to Steve Hunt for helpful ideas about Raglan Harbour and assistance creating new maps, and to all of the INTERCOAST and Coastal Marine Group whanau for your support and friendship: Arohanui!

I am thankful for the chance to collaborate with Britt Raubenheimer and Steve Elgar. They provided access to high-quality processed field measurements at New River Inlet, North Carolina and provided many useful comments and suggestion to improve the application of the semi-analytical jet model, valuable editorial assistance, and positive encouragement along the way. Thanks to the personnel from the US Army Corps of Engineers Field Research Facility for providing the bathymetric data and logistical support, the PVLAB (WHOI) field crew for deploying, maintaining, and recovering the instruments, and Jim Thompson (UW-APL) for fruitful discussions that improved the study at New River Inlet.

Thanks to the scientists formerly known as ASR Ltd, namely Jose Borrero, Dougal Greer, James Frazerhurst, Laurent Lebreton, Cyprien Bosserelle, Shaw Mead, and Kerry Black for introducing me to this field, and for nurturing my interest in beaches and waves. Also, thank you for providing access to bathymetry, instrument data, and constructive discussions. Your friendships have been positive and meaningful.

Thank you Terry Healy for fond memories and encouragement to complete a PhD at University of Waikato. Also, many thanks to Vernon Pickett for your enthusiasm and support with data, contacts, and friendship.

Thanks to D. Murray Hicks (NIWA) and William Nardin (Boston University) for your helpful feedback and suggestions while examining this thesis.

Many thanks to Guy Gelfenbaum (USGS – PCMSC) and Albert Kettner (CSDMS) for the stimulating conversations and helpful ideas.

Most importantly, I thank my family for being supportive and tolerating my extended absence and late nights. Thank you Cassie for travelling to New Zealand with me and giving me beautiful children. Your support and encouragement have been essential throughout this journey. Thank you Hannah and Henry for joining us on this journey, you have helped me learn about priorities, patience, and unconditional love. And thanks to my mom for your personal sacrifices to ensure opportunities were available to me and your continual encouragement to reach high.

Table of Contents

List of Figures

List of Tables

List of Symbols

The following symbols are used in this paper:

$2\mathrm{D}$ = Two-dimensional;

$3\mathrm{D}$ = Three-dimensional;

A_{sb} = Bed-load multiplication factor [-];

A_{ss} = Suspended-load multiplication factor [-];

ARMAE = Adjusted Relative Mean Absolute Error [-];

a = coefficient of entrainment, representing inflow across the jet boundary [-];

B = wave breaking intensity, or 'breaker coefficient' [-];

B_{JD} = wave breaking intensity for jet-dominated conditions [-];

B_{WD} = wave breaking intensity for wave-dominated conditions [-];

b = jet half-width [m];

b_0 = jet half-width at the inlet (model shoreward boundary) [m];

C = Chézy roughness coefficient [$m^{1/2}$ s^{-1}];

C_f = drag coefficient due to current (in SvR) [-];

C_{bed} = speed of propagating bed forms [m s^{-1}];

CFL_{MF} = Courant-Friedrichs-Lewy criterion for morphological changes [m s^{-1}];

c = wave phase velocity [m s^{-1}];

c_f = friction factor [-];

$c_{f\mathrm{JD}}$ = friction factor for jet-dominated conditions [-];

$c_{f\mathrm{WD}}$ = friction factor for wave-dominated conditions [-];

c_g = wave group velocity [m s^{-1}];

c_t = turbulence factor for dissipation due to turbulent mixing [-];

$c_{t\mathrm{JD}}$ = turbulence factor for jet-dominated events [-];

$c_{t\mathrm{WD}}$ = turbulence factor for wave-dominated events [-];

D_* = dimensionless sediment grain diameter [-]

D_{50} = median sediment grain diameter [m]

D_{90} = 90th percentile of the mass of sediment distribution by grain diameter [m]

dt = discretization of time, or 'time step' [s];

dx = discretization of space along the x-axis [m];

E = wave energy = $\rho g H_{rms}^2/8$ [N m^{-1}];

Ec_g = wave energy flux [J m^{-1} s^{-1}];

$\bar{F}_{t,x}$ = x-component of vertically-averaged momentum loss due to turbulence mixing [N m^{-2}];

$\bar{F}_{t,y}$ = y-component of vertically-averaged momentum loss due to turbulence mixing [N m^{-2}];

$F_{t,x}$ = x-component of vertically- and laterally-averaged momentum loss due to turbulence mixing [N m^{-2}];

$F_{t,y}$ = y-component of vertically- and laterally-averaged momentum loss due to turbulence mixing [N m^{-2}];

$\bar{F}_{w,x}$ = x-component of vertically-averaged wave forces $= -\partial S_{xx}/\partial x - \partial S_{yx}/\partial y$ [N m^{-2}];

$\bar{F}_{w,y}$ = y-component of vertically-averaged wave forces $= -\partial S_{xy}/\partial x - \partial S_{yy}/\partial y$ [N m^{-2}];

$F_{w,x}$ = x-component of vertically- and laterally-averaged wave forces $= -\partial\left(E\left(2c_g/c - 1/2\right)\right)/\partial x$ [N m^{-2}];

$F_{w,y}$ = y-component of vertically- and laterally-averaged wave forces [N m^{-2}];

g = gravitational acceleration [m s^{-2}];

H_{rms} = root-mean squared wave height (from trough to crest) [m];

H_b = root-mean squared wave height at wave breaking [m];

h = height of the water column [m];

h_b = height of the water column at wave breaking [m];

I_1 = *area* of normalized jet half-width profile $= \int_0^1 J(\zeta)d\zeta$ [-];

I_2 = *volume* of normalized jet half-width profile $= \int_0^1 J^2(\zeta)d\zeta$ [-];

$J(\zeta)$ = similarity profile across jet width [-];

k = wave number [radians m^{-1}];

M_x^s = Wave-induced mass flux [kg m^{-1} s^{-1}];

$\mathrm{Meas}_i =$ measurement at sensor i;

$\mathrm{MF} =$ morphological acceleration factor [-]; i;

$\mathrm{Pred}_i =$ prediction at sensor i;

$Q_{bx} =$ locally-advected bed load sediment transport rate [kg m^{-3}];

$Q_{sx} =$ locally-advected suspended sediment transport rate [kg m^{-3}];

$r =$ jet core half-width [m];

$S_{xx} =$ principal component of radiation stress [N m^{-1}];

$S_{xy} = S_{yx} =$ radiation shear stress [N m^{-1}];

$S_{yy} =$ transverse component of radiation stress [N m^{-1}];

SvR = Soulsby-van Rijn (sediment transport formulation);

$T_p =$ peak wave period [s];

$t =$ time [s];

$u =$ vertically-averaged current velocity in the x-direction (cross-shore) [m s^{-1}];

$u_0 =$ vertically-averaged current velocity in the x-direction at the inlet, or shoreward model boundary [m s^{-1}];

$u_c =$ vertically-averaged current velocity in the x-direction along the jet centreline [m s^{-1}];

$u_{orb} =$ near-bottom wave orbital velocity in the x-direction [m s^{-1}];

$u^s =$ Stokes drift [m s^{-1}];

$v =$ vertically-averaged current velocity in the y-direction [m s^{-1}];

$v_p =$ bed porosity, or void space of the seabed composition [-];

$x =$ cross-shore distance [m];

$x' =$ distance along channel thalweg from inlet (sensor 04) [m];

$y =$ alongshore distance [m];

$\gamma =$ the ratio of wave height to depth at breaking, 'breaker index' [-];

$\Delta =$ the relative sediment density [-];

$\Delta\mathrm{Meas}_i =$ the adjustment term for ARMAE, accuracy of measurements;

$\varepsilon_b =$ dissipation of wave energy flux from breaking [J s^{-1}];

$\zeta =$ distance in the cross-jet dimension normalized by jet width [-];

$\bar{\zeta} =$ normalized cross-jet dimension in ZOFE ($\bar{\zeta} = \zeta$ when $r = 0$) [-];

$\eta =$ water level surface above a horizontal datum, e.g. mean sea level [m];

$\theta =$ Angle of wave propagation with respect to current flow [°];

$\kappa =$ median sediment grain diameter [m]

$\nu =$ kinematic viscosity, assumed here to be 0.40 [-];

$\xi =$ multiplicative factor governing power of sediment transport relation [-];

$\rho =$ density of water, assumed here to be 1027 [kg m^{-3}];

$\rho_s =$ material density of sediment [kg m^{-3}];

$\sigma =$ intrinsic angular wave frequency [rad s^{-1}];

$\bar{\tau}_{b,x} =$ bed shear-stress in the x-component, $= \rho c_f (u^2 + v^2) u$ [N m^{-2}];

$\bar{\tau}_{b,y} =$ bed shear-stress in the y-component, $= \rho c_f (u^2 + v^2) v$ [N m^{-2}];

$\tau_b =$ total bed shear-stress [N m^{-2}];

$\tau_{b,x} =$ laterally-averaged x-component (streamwise) of bed shear-stress [N m^{-2}];

$\tau_{b,y} =$ laterally-averaged y-component of bed shear-stress [N m^{-2}];

$\omega =$ absolute angular frequency [radians s^{-1}];

Chapter 1

General Introduction

1.1 Background

The Raglan Bar is an example of a geomorphic feature known as an 'ebb-tidal delta' which is a subclass of the more general 'delta' feature which is broadly described as an accumulation of sediment in a receiving basin. Deltas develop at the boundary between zones in which alluvial processes and basin processes dominate. The first use of the term 'delta' to refer to these sediment accumulations was attributed to the ancient Greek historian Herodotus who used the term to describe the Nile river delta because its triangular shape resembled the Greek letter 'Δ' (*Herodotus*). *Fagherazzi and Overeem* (2007) give a detailed review on deltas.

This research, however, is focused more specifically on *ebb-tidal* deltas, which are large accumulations of sediment seaward of the mouth of a river, harbour or other type of tidal constriction where (ebb) tidal currents have deposited sand over time (*Van der Vegt et al.*, 2006). Ebb-tidal deltas are found along coastlines all around the world. Along the North Sea Frisian coast for example, a vast series of ebb-tidal deltas extend into the sea from tidal constrictions between barrier islands (see Figure 1.1a). The entrances to most of the estuaries in New Zealand are characterised by an ebb-tidal delta (e.g. *Hicks and Hume*, 1996).

In general, ebb-tidal deltas are characterised by the occurrence of a main ebb-shoal, or mound of sediment that accumulates seaward of a main (ebb-dominant) channel (shown in Figure 1.1b). Typically a main channel is bounded laterally by channel margin linear bars (or 'levees') as it cuts seaward through the main body of sediment often called a swash platform, over the shallow ebb-shoal, and opening to the sea. The seaward end of the ebb-shoal is called the terminal lobe. Often, sandbars form on top of the swash platform and migrate shoreward eventually joining the adjacent beaches.

Ebb-tidal deltas play a significant role in moving sediment around coastal littoral cells. The shallow shoals shelter inlets by dissipating wave energy offshore and redirecting waves onto adjacent beaches (e.g. *Fitzgerald*, 1984). Ebb-tidal deltas provide a mechanism for sediment to bypass an inlet (*Syvitski and Saito*, 2007), and can function as temporary and long-term sand storage, exchanging sediment between the adjacent beaches, nearshore and inlet mouth (e.g. *Fitzgerald et al*., 1984; *Gelfenbaum*, 1999). In many cases, ebb-tidal deltas also impact the morphology of neighbouring coastlines (e.g. *Ashton and Giosan*, 2011). For example, the East Frisian Islands shown in Figure 1.1 have been observed over the past 400 years to change shape and position through inlet sediment

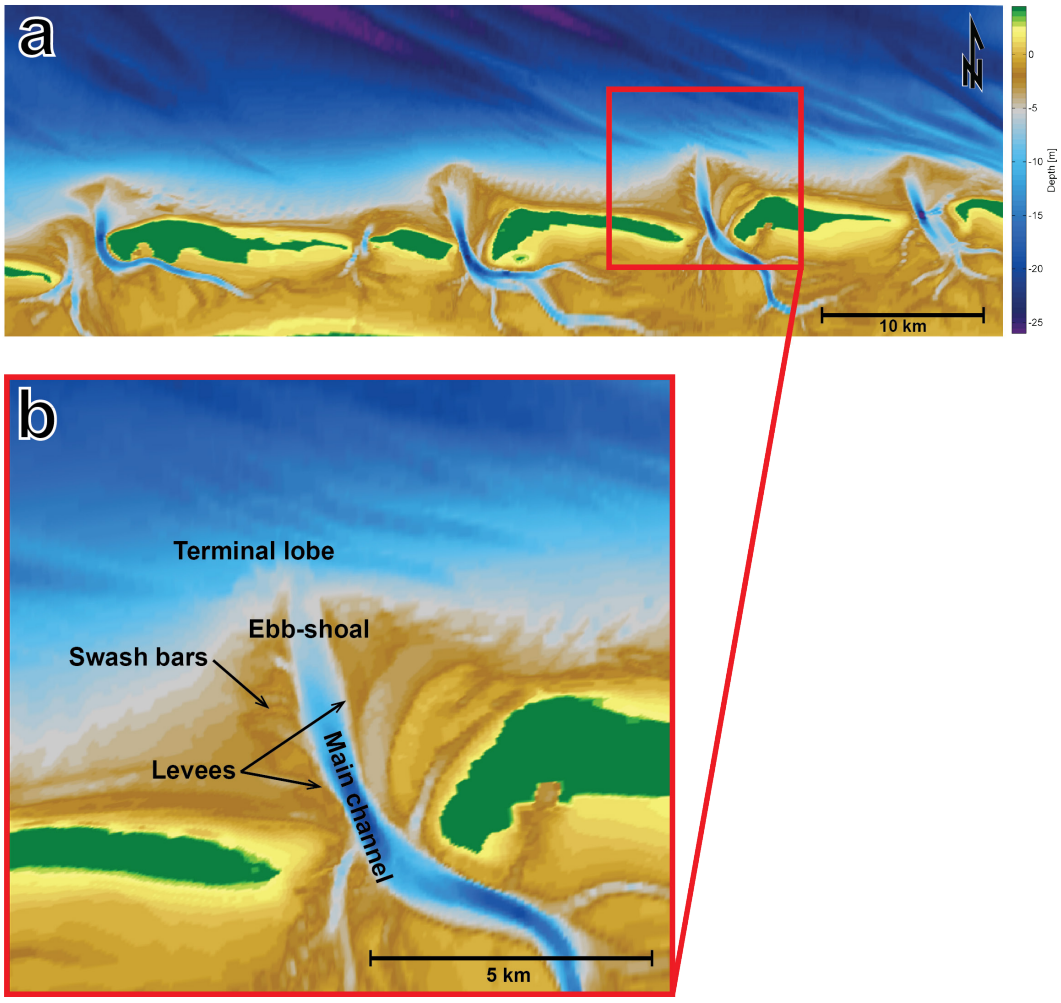

Figure 1.1. (a) Ebb-tidal deltas seaward of tidal constrictions between barrier islands along the East Frisian Islands of Germany, and (b) a close up of the features common to ebb-tidal deltas (see text for details). Bathymetry data courtesy of Gerald Herrling.

bypassing services of the ebb-tidal deltas (*Fitzgerald et al.*, 1984).

Despite the useful services ebb-tidal deltas provide to their adjacent coastlines, human accounts are often less desirable. Historical literature is filled with stories and colourful accounts of navigating by boat across the shallow sandbars at ebb-tidal deltas (commonly referred to as 'bar crossings'). Usually these stories tend to have a grave tone and associate bar crossing with danger and mystery (e.g. *Philip*, 1871; *De Jong*, 1998). For example, the poem 'Crossing the Bar' (*Tennyson*, 1889) uses an extended metaphor to compare death to sailing past an ebb-tidal delta, which is positioned between the ebbing tidal-stream (or river), which represents life, and the ocean, which represents the boundless depth and unknowns of death.

The sense of danger attributed to ebb-tidal deltas in stories is well founded as many ship wrecks occur while crossing the shallow sandbars of ebb-tidal deltas while attempting to enter (or exit) harbours. Often large waves shoal unsuspectingly on unseen shallow bars (e.g. Figure 1.2). For

Figure 1.2. Large waves about to overwhelm US Coast Guard vessel during training exercises at the ebb-shoal of Morro Bay, California. Photo courtesy of Gary Robertshaw, 2007.

example, the ‘worst maritime tragedy to occur in New Zealand waters’ (*Otago Witness*, March 7, 1863, p7) occurred as the HMS *Orpheus* ran aground on a submerged sandbar at the entrance to Manukau Harbour before being overwhelmed by the power of the surf and surging sea, killing 189 British sailors. Even in present times, harbour bar crossing is a major hazard and the focus of recent efforts in New Zealand to educate boaters about risks and safety precautions associated with transiting an ebb-tidal delta (*Waikato Regional Council*, 2013).

For harbours where major shipping is important, regular maintenance dredging to clear channels is required for safe transit across ebb-tidal deltas. For example, the US government is currently spending roughly $300M to maintain safe passage of the Columbia River ebb-tidal delta, which supports $20B in international trade, 42 million tons of cargo and more than 40,000 maritime-related jobs each year (*USACE*, 2012).

Perhaps the association in historical literature of ebb-tidal deltas with mystery is reasonable, as there are many things about them that we still do not understand. The interaction of fast-moving currents and waves influence the movement of sediment and sandbars while the sandbars impact the waves and currents, leading to conditions that are difficult (at best) to predict. The nonlinear effects of wave-current interaction, shoaling and breaking waves, and turbulent processes occurring at multiple scales limit our understanding of the hydrodynamic forces responsible for transporting sediment. Also, the sediment and bedforms interact with the forcing as part of an interconnected dynamical system with feedback, leading to unexpected behaviour in the movement of bedforms. For example, at the time of the grounding of the HMS *Orpheus*, detailed navigational charts of the crossing were used, but the sandbars had moved northwards and grown considerably during the two years since the previous detailed charts were updated. Despite the significant functions provided by ebb-tidal deltas and the impact they have navigation, the processes governing their development, evolution, and interaction with adjacent beaches are still not understood fully (*Fagherazzi and Overeem*, 2007).

Ebb-tidal deltas exist in many different shapes and sizes, and their overall morphology is known to be determined by the interaction of tidal currents, waves and sediment supply (e.g. *Hayes*, 1980). The long-term (order of decades) equilibrium size and shape of ebb-tidal deltas is determined by tidal prism, wave energy, available sediment, and accommodation space (e.g. proximity to rocky headland) (e.g. *Walton and Adams*, 1976; *Hicks and Hume*, 1996). While deltas are relatively stable at long timescales, they are considered highly-dynamic in the short timescale (*van der Vegt et al.*, 2006). Short-term morphodynamic responses occur from sediment transport by temporary wave and wind events, typically as the formation, migration, and dissipation of sandbars (*Sha*, 1989). Qualitatively, patterns of morphological change have been observed to occur in cycles based on the "maturity" of a delta as determined based on the occurrence of accretion or erosion (*Oertel,* 1977). Youthful deltas are characterized by the deposition of fresh sediment loads at the inlet, which is reworked with tides and waves around the delta into bars and channels in maturity. The erosion of old deltas continues until a dynamic transition occurs and the cycle is reset. These cycles are a means of transporting sediment across inlets and occur in response to a fluctuating littoral budget and changing hydrodynamic conditions. More detailed observations of short-term responses have captured meso-scale sandbar migration at speeds up to $3.5\ \mathrm{m\ day^{-1}}$ (*Pianca et al.*, 2014) and the movement of an entire ebb-shoal over 50 m in two weeks (*Balouin et al.*, 2004).

Early attempts to understand the hydrodynamics that drive development and evolution of ebb-tidal deltas made significant progress using analytical models of an ebbing tidal jet (or 'ebb-jet') (e.g. *French*, 1960; *Abramovich*, 1963; *Özsoy*, 1977; *Joshi and Taylor*, 1983; *Ortega-Sanchez et al.*, 2008). *Özsoy and Ünlüata* (1986) used an analytical jet model to predict spatial patterns of sediment transport capabilities. However, the mathematical formulations became difficult to solve by hand if many processes were included over general terrain. As such, none included the presence of waves or the evolution of bathymetric morphology. These analytical ebb-jet model attempts were supported by scaled physical models in the

laboratory of ebb-jets with and without non-breaking waves (e.g. *Ismail and Wiegel*, 1983) and their impact on sedimentation patterns (e.g. *Rowland et al*., 2007).

Detailed process-based numerical models have become very sophisticated and are able to simulate the complicated hydrodynamics occurring at ebb-tidal deltas (e.g. *Nardin and Fagherazzi*, 2012; *Nardin et al*., 2013; *Olabarrieta et al.*, 2014). Numerical models are able to generate realistic current patterns that largely agree with field measurements (e.g. *Chen et al.*, 2015), but the inclusion of many interacting processes complicates the deconstruction of fundamental cause and effect relationships. Also, computational costs of numerical models are far greater than analytical models, and limit the type, extent, and duration of simulations possible.

Numerical models make it relatively easy to include morphological evolution in response to currents and waves (e.g. *Lesser et al*., 2004; *Roelvink*, 2006), and to the effects of tidal range (*Leonardi et al.*, 2013). The application of numerical morphological evolution models to ebb-tidal deltas has been very successful for determining qualitative trends in morphological development (e.g. *Kraus*, 2000; *van Leeuwen et al*., 2003; *van der Vegt et al.*, 2006; *Ashton and Giosan,* 2011) and a generic review is given in *de Swart and Zimmerman* (2009). However, when quantitatively compared with actual observations and over shorter than developmental timescales, predictions of ebb-tidal delta morphological evolution diverged substantially from measurements (e.g. Gelfenbaum et al., 2003; *Lesser*, 2009)

In general, to achieve better predictive ability of numerical morphological evolution models, improved model physics and parameterizations of the physical processes governing morphological evolution are needed (*Nearshore Processes Community*, 2015). Sediment transport modelling is already ‘difficult, highly-empirical and inaccurate’ for current-only situations, but is much worse at places like ebb-tidal deltas where waves are included (*Roelvink and Reniers*, 2011). When feedback with morphological

evolution is included, a true nonlinear dynamical system emerges, vulnerable to nonlinear phenomena and behaviour that is sensitive to intrinsic model parameters, making it difficult to determine whether predictions are realistic or merely properties of the model.

To ground predictions in reality and improve the predictive capacity of numerical morphological evolution models, detailed observations are needed (*Nearshore Processes Community*, 2015). Detailed geomorphic measurements at ebb-tidal deltas are difficult to capture in-situ due to the high-energy conditions and shallow, mobile bed features. Hydrographic surveys are possible, but require calm conditions and typically occur at intervals greater than is practical to capture migrating ebb-shoals and sandbars. Furthermore, geomorphic timescales require observations to continue at durations greater than years, which is also impractical for typical in-situ instrument deployments. Nevertheless, if there are to be advances in the predictive ability of morphological models, detailed observations are needed to guide their progress.

Understanding the connections between forcing conditions, hydrodynamic, and morphodynamic processes is an ongoing research theme. In practice, progress has become waylaid by detail and lacks fundamental understanding and support.

1.2 **Key Thesis Questions**

I hypothesise that ebb-tidal delta morphology forms as a result of dynamic balance between the dominant forces responsible for sediment transport, namely the ebbing tidal jet currents and opposing waves. Further, variations in ebb-tidal delta morphology are likely due to changes in the dynamic balance between those forces around the existing morphology.

I propose that our understanding of ebb-tidal delta morphodynamics will improve with enhanced ability to observe ebb-tidal delta geomorphology, and by using exploratory tools to investigate the balance of forces and response which is expressed as morphodynamic change.

Key thesis questions include:

- Is the movement of ebb-tidal delta features dependent more on waves or on tidal currents?
- Under what conditions is an ebb-jet wave or tide dominated?
- Is it enough to predict ebb-jet tidal currents by only considering a few significant factors (e.g. inertia, friction, turbulence, and waves), rather than requiring full detailed representation of many processes?
- How does an ebb-jet behave differently with opposing waves?
- How is the position of ebb-shoal development sensitive to tidal currents, waves and sediment?
- What are the processes that control the position of channel margin linear bars (or 'levees') and how does this affect the terminal lobe dynamics?
- Is observed ebb-tidal delta morphology seasonal?
- Is there evidence to support the claim that ebb-tidal deltas are nonlinear dynamical systems?
- Does the response of ebb-shoal position to forcing depend on the initial position of the ebb-shoal?

To answer these questions and build understanding of morphodynamics at ebb-tidal deltas, in this thesis I gather and analyse a 5-year geomorphic observational record of the ebb-tidal delta at Raglan using video-based techniques, develop a semi-analytical ebb-jet model to describe the extent and strength of ebbing tidal currents in the presence of waves, and use the ebb-jet model to drive an exploratory morphodynamic model for ebb-tidal shoal and channel development and evolution to explore the sensitivities of delta morphology to changes in fundamental forcing.

1.3 **Thesis Overview**

The main body of this thesis is composed of three research chapters, in which I use a variety of methods to learn more about the short-term forcing and response of ebb-tidal deltas. Each of the three chapters was intended

as a stand-alone document for submission to an international, peer-reviewed journal.

I begin in Chapter 2 by using video-based remote sensing techniques to observe geomorphic features at an ebb-tidal delta at Raglan, New Zealand. The position of major features and transient sandbars were detectable and their movements were traced over 5 years. Patterns of geomorphic change were related to seasonal and interannual environmental conditions. To date, this work presents the most frequently sampled and longest duration observational record of meso-scale geomorphic evolution at an ebb-tidal delta. The paper based on the work in Chapter 2 is being prepared for submission to *Journal of Geophysical Research – Earth Surfaces*.

The objective of Chapter 3 was to examine the fundamental hydrodynamic processes occurring at ebb-tidal deltas by developing a semi-analytical model for an unstratified jet in the presence of waves. The 'jet model' extends previous work by including the first-order effects of waves (and wave dissipation) on ebb-jet current speed, extent, and width. The model is fast, computationally cheap, and predicts realistic currents within the main channel and ebb-shoal of an ebb-tidal delta. The paper based on the work in Chapter 3 will be submitted to *Journal of Waterway, Port, Coastal, and Ocean Engineering*.

Chapter 4 couples the semi-analytical ebb-jet model (from Chapter 3) with sediment transport formulae to develop an exploratory morphodynamic evolution tool able to describe the development of ebb-shoal and channel morphology. In addition to development, the model is also used to describe short-term cross-shore response to changes in forcing conditions of sandbars on established ebb-shoals with conditions representative of those observed at Raglan in Chapter 2. A portion of the Chapter was submitted as a paper to a special issue of *Computers & Geosciences* focussed on "Uncertainty and Sensitivity in Surface Dynamics Modelling".

The three research chapters are followed by a concluding discussion in Chapter 5, which summarizes the main findings of this thesis and ends with overall conclusions and suggestions for further research.

Chapter 2

Observations of the Geomorphology of an Ebb-Tidal Delta

Photo captured 9th April 2012, courtesy Raphael Lumgrüber.

Harrison, S.R., Bryan, K.R. and Mullarney, J.C. (in preparation). Observations of the geomorphology of an ebb-tidal delta. *Journal of Geophysical Research: Earth Surfaces*.

Contribution of Authors

Chapter 2 presents the article entitled “Observations of the geomorphology of an ebb-tidal delta”, which is being prepared for submission to *Journal of Geophysical Research: Earth Surfaces*. This study provides a significant contribution to the scientific field by showing detailed measurements of geomorphic features at a mixed-energy ebb-tidal delta and showing seasonal and interannual morphodynamic behaviour.

The Raglan Cam-Era video system was installed by Waikato Regional Council prior to the start of my PhD and kindly provided for my use in this thesis. I processed and analysed all the video, wave and tidal data. I wrote all of the numerical code to process and analyse the data, prepared all of the figures and wrote the initial and subsequent drafts of the article. My co-authors, K. R. Bryan and J.C. Mullarney edited drafts and provided helpful direction. With the guidance of K.R. Bryan, my image processing abilities were enhanced and refined.

Abstract

Video observations of depth-limited wave-breaking patterns at an ebb-tidal delta on the energetic west coast of New Zealand at Raglan were used to identify geomorphic features over a 5-year period. The terminal lobe, mouth bar, channel margin linear bars, and swash bars were identified and tracked over the duration. Morphodynamic response was related to environmental conditions by correlating observed movements with concurrent wave and tidal conditions. Movements occurred largely in response to transition between seasonal forcing trends, with winter deltas generally broader and further seaward than the summer deltas which were more cuspate. The formation of a double-barred ebb-shoal was observed, with the outer bar dependent more strongly on wave conditions and the inner bar on ebb-jet strength. Also, swash bars were observed to constrict the seaward extent of the main channel during large wave events, which was subsequently cleared by tidal currents. These observations suggest that ebb-shoal features are dependent upon competition between ebb-jet strength and opposing waves. Interannual morphological changes did not appear strongly related to any environmental forcing, indicating that the ebb-tidal delta is a morphological system which to some degree is self-organized.

2.1 Introduction

Ebb-tidal deltas are large sedimentary accumulations on the seaward side of tidal inlets that play a significant role in moving sediment around coastal littoral cells (e.g. Figure 2.1). Deltas shelter inlets by dissipating and redirecting wave energy offshore and onto adjacent beaches, respectively (e.g. *Fitzgerald*, 1984) and they provide a mechanism for sediment to bypass an inlet (*Syvitski and Saito*, 2007). Deltas also function as temporary and long-term sand storage, exchanging sediment between the adjacent beaches, nearshore and inlet mouth (e.g. *Fitzgerald et al*., 1984; *Gelfenbaum*, 1999). Despite the importance of ebb-tidal deltas, the processes governing their development, evolution, and interaction with

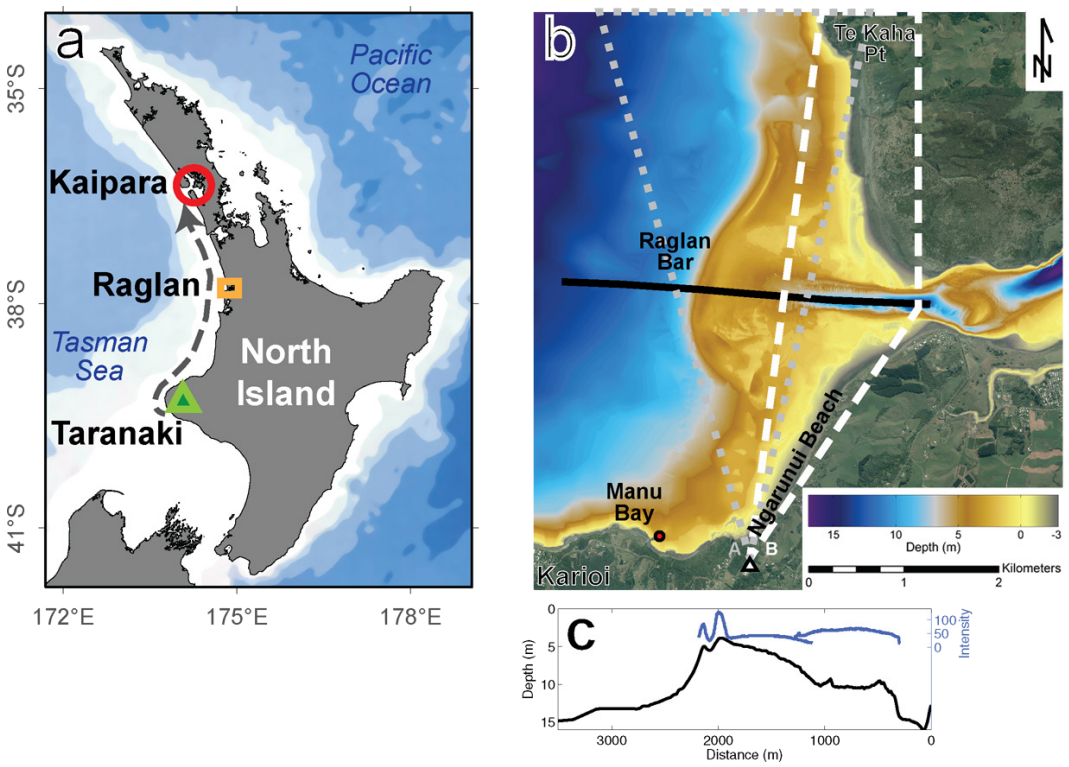

Figure 2.1. (a) Whaingaroa (Raglan) Harbour on the west coast of central North Island, New Zealand. (b) Multibeam echo-sounder bathymetry data of the Raglan Bar (provided by Waikato Regional Council), with Cam-Era location (white triangle), Raglan A field of view (grey dotted line), Raglan B field of view (white dashed line), and Manu Bay water elevation gauge (red dot). (c) Distribution of depth (black line) and relative pixel intensity (blue line) of rectified image pair shown in Figure 2.3a along the main thalweg (marked by black line on panel b).

adjacent beaches are not fully understood (*Fagherazzi and Overeem*, 2007).

Ebb-tidal deltas form in response to tidal forcing through an inlet (*Van der Vegt et al.*, 2006), with their equilibrium size and shape determined by the tidal prism (*Walton and Adams*, 1976), wave energy, and available sediment (e.g. *Hicks and Hume*, 1996). *Galloway* (1975) classifies delta geomorphology based solely on the relative influences of fluvial, wave or tidal processes. However, when short-term conditions (i.e. flow, waves, and sediment supply) deviate from long-term averages, a local morphodynamic response occurs, typically in the form of mobile bedforms or sandbars migrating along the delta toward the nearshore or adjacent beaches (*Sha*, 1989; *Hicks et al.*, 1999; *Sherwood et al.*, 2001; *Ruggiero et al.*, 2003; *Ruggiero et al.*, 2009). For instance, following severe runoff through the Santa Clara River mouth in California, an abnormally large delta formed, which subsequently diminished in volume when the normal

forcing conditions returned, with excess sediment transported to the downdrift beaches as a morphological ‘wave’ (*Barnard and Warrick*, 2010).

The physical processes occurring at an ebb-tidal delta are interconnected and vary depending on location. During ebb, a jet of water (‘ebb-jet’) flows from an inlet across the ebb shoal into the sea. The ebb-jet spreads laterally in response to the morphology (*Kilcher and Nash*, 2010), the density structure (*Wright*, 1977), and the interactions with incident surface gravity waves (*Ismail*, 1980). The incident surface waves are influenced by the morphology, as well as by their interaction with tidal currents (*Van Rijn*, 1990). As waves propagate shoreward, their energy focuses on the shallowest part of an ebb-tidal delta. For conditions with sufficiently large wave energy, depth-limited wave breaking will occur, maximizing the effect of waves on the ebb currents and driving shoreward flow over the ebb shoal and into the inlet (e.g. *Olabarrieta et al*., 2011). In the case of river flows, the effects of buoyancy are decreased as the vertical stratification is destroyed by mixing during wave-breaking (*Wright*, 1977).

Recent numerical model investigations on the role of ebb-tidal delta morphology and wave-current interaction at inlets (*Olabarrieta et al*., 2014) show how Stokes drift and wave breaking-induced accelerations produce shoreward water mass transport creating a wave setup that decreases with alongshore distance from the inlet. The wave setup causes an alongshore pressure gradient that forces alongshore current along both sides of the ebb shoal toward the adjacent beaches (*Shi et al*., 2011). The gradient in alongshore current drives sediment convergence and coastal change in the form of deposition along the adjacent beaches. Changes in morphology feed back to the system by affecting the hydrodynamic and wave patterns which are responsible for further sediment transport and coastal change.

The need for improved model physics and parameterizations of the physical processes governing morphological evolution was identified as a major research direction for the immediate future of nearshore processes research (*Nearshore Processes Community*, 2015). The need arises

because the dynamic behaviour of interacting coastal processes may be nonlinear (*De Vriend*, 1991a*; De Vriend*, 1991b). To achieve any predictive capacity, numerical models must have significant fundamental processes well represented or robustly parameterized. Sediment transport modelling is already 'difficult, highly empirical and inaccurate' for current-only situations, but is much worse at places like ebb-tidal deltas where waves are included (*Roelvink and Reniers*, 2011). Waves interact with current to modify the bed shear stress (*Grant and Madsen*, 1979; *Soulsby and Clarke*, 2005), bed ripples (*Traykovski*, 2007), and sediment mobility (*Li et al*.,1996). Most of these interactions occur at much smaller spatial and temporal scales than are convenient to use when modelling the evolution of morphology, so parameterizations of the physical processes are necessary to include in numerical models (e.g. *Fredsøe*, 1984; *Van Rijn*, 2007). Coastal evolution is the result of time-integrated physical processes acting in the short term (*Cowell and Thom*, 1994). Yet, modelling detailed coastal change over morphological timescales is often impractical in linear time, and so the occurrence of events is typically parameterized with input reduction techniques to a few representative wave conditions (e.g. *De Vriend et al*., 1993; *Daly et al.*, 2014). The problem with this is that the morphodynamic response of some coastal features (e.g. barred beaches and ebb-tidal deltas) depends on the order of forcing events (e.g. *Plant et al.*, 1999).

Detailed observations are needed to verify models and guide further development, in such cases where there are many uncertainties associated with modelling evolving morphology subject to wave-current interaction (*Nearshore Processes Community*, 2015). However, few observations of ebb-tidal delta geomorphic features exist, and those that do exist tend to be infrequently sampled. The same conditions that drive morphodynamic change at an ebb-tidal delta also inhibit the collection of adequate field measurements. Hydrographic surveys by boat are difficult due to the shallow sandbars and require calm surface water for safety and quality assurance. In-situ measurements are also difficult to collect, because instrument deployment and retrieval requires calm conditions,

there is a high risk for instruments to be moved, lost, or buried by sand waves, and point measurements lack the spatial coverage to capture the diverse conditions occurring at ebb-tidal deltas. Also, frequent observations are needed in order to track quickly-moving sandbars likely at ebb-tidal deltas. For these reasons, remote sensing is a potential solution.

The use of video-based remote sensing in various coastal monitoring applications is attractive because video observation provides continuous and automated data collection (e.g. *Holman and Stanley*, 2007; *Aarninkhof et al.*, 2003; *Gallop et al*., 2009). Pixel intensity associated with the dissipation of wave energy during depth-limited breaking is white in colour and is used to infer the position of shallow sandbars in time-averaged imagery. The method has been validated and widely used at beaches (e.g. *Plant et al.*, 2007). Video data have only recently been used to observe ebb-tidal delta morphology (e.g. *Balouin et al.*, 2004; *Pianca et al*., 2014).

Pianca et al. (2014) observed meso-scale sandbars move along the southern flank of the New River Inlet (North Carolina) ebb-tidal delta during a 23 day experiment. Their video observations were supported by a very detailed field campaign (e.g. *Wargula et al*. 2014; *Clark et al.*, 2014) and included in-situ current and wave measurements and multiple hydrographic surveys using a specialist Army amphibious vehicle (LARC-5) to validate the techniques for inferring sandbar migration from video. Meso-scale sandbars were observed to move at an average rate of $1.5\ \mathrm{m\ day^{-1}}$ and up to $3.5\ \mathrm{m\ day^{-1}}$ depending on wave conditions.

In this paper, we aim to use video-based techniques to provide detailed observations on the annual and interannual changes to the terminal lobe position and shape and the propagation speed and direction of swash bars on an ebb-tidal delta. Further, we relate these seasonal trends in morphodynamic response to forcing patterns. A 5-year long data base of averaged video imagery is used for analysis.

2.2 **Regional Setting**

The Raglan Bar (known locally as 'The Bar') is an ebb-tidal delta located seaward of the entrance to Whaingaroa (Raglan) Harbour on the west coast of the central North Island of New Zealand (Figure 2.1). The harbour entrance and ebb-tidal delta are located on a relatively straight stretch of coast, but in the lee of a large (elevation 756 m) volcanic headland ('Karioi') which partially shelters the delta from the dominant wind and wave direction which is from the southwest (*Sherwood and Nelson*, 1979; *Gorman et al.*, 2003). The Bar has been described as a mixed-energy, free-form, nearly symmetric delta composed of approximately $7.10 \times 10^6\ \mathrm{m}^3$ of fine-grained ($d_{50} = 0.20\ \mathrm{mm}$) titanomagnetite sand (*Hicks and Hume*, 1996; *Sherwood and Nelson*, 1979). The ebb-tidal delta is considered stable according to the empirical relationship between delta volume and spring tidal prism (*Walton and Adams*, 1976; *Marino and Mehta*, 1987; *Hicks and Hume*, 1996).

Recent multibeam echo-sounder hydrographic survey data (surveyed on the 18th -20th November, 2013 and provided by Waikato Regional Council, see Appendix A for details) at Raglan reveals many characteristic features of a mixed-energy, meso-tide ebb-tidal delta (Figure 2.1b). A single ebb-dominated channel, approximately $300\ \mathrm{m}$ - $450\ \mathrm{m}$ wide at the inlet between low to mid-tide and oriented approximately $5°$ north of west, cuts through the main body of the ebb-tidal delta. Near the inlet, the channel is deepest at the inlet gorge (approximately $15\ \mathrm{m}$), and bounded on the north and south by channel margin linear bars (or 'levees') that are partially exposed during low-tide (Figure 2.1b). Bedforms of various scales can be seen in the channel and along its margins, with crests oriented perpendicular to the channel orientation. Moving seaward from the inlet, the channel broadens in width and becomes shallower until it meets the crest of the mouth bar (approximately $4\ \mathrm{m}$ below mean sea level ('msl')) and before opening to the Tasman Sea (Figure 2.1c). The main body of the delta is a broad, cuspate, shallow swash platform extending nearly $2\ \mathrm{km}$ seaward of the inlet at its centre and nearly $3\ \mathrm{km}$ wide. The seaward edge of the swash platform is a terminal lobe extending shoreward at its

northern and southern extremities over several hundred metres. The terminal lobe was nearly symmetric when surveyed, with the northern arm slightly longer and straighter than the southern arm, which was more sharply directed towards the southern beach. The inlet is bordered by black sandy beaches to the north and south, with a small rocky headland ('Te Kaha Point') nearly $2\ \mathrm{km}$ to the north of the inlet and the large basalt headland (Karioi) nearly $2\ \mathrm{km}$ to the south. Te Kaha Point extends just over $300\ \mathrm{m}$ seaward from the adjacent shoreline, and Karioi protrudes nearly 6 km seaward of the inlet position.

Whaingaroa Harbour is a ria formed by post-glacial flooding of the lower reaches of a river valley over the last $10{,}000$ years, and now covers nearly $33\ \mathrm{km}^2$ of which $24\ \mathrm{km}^2$ is intertidal (*Sherwood and Nelson*, 1979). The harbour is meso-tidal, with mean spring and neap tidal ranges of $2.8\ \mathrm{m}$ and $1.8\ \mathrm{m}$ respectively (*Heath*, 1976), and maximum astronomical tides approaching $4\ \mathrm{m}$. The mean spring and neap tidal prisms are $46 \times 10^6\ \mathrm{m}^3$ and $29 \times 10^6\ \mathrm{m}^3$ respectively (*Heath*, 1975) and are funnelled through the inlet gorge, measured to have a cross-sectional area between $2900\ \mathrm{m}^2$ to $2750\ \mathrm{m}^2$ (see Appendix A) during mid to low tide [slightly smaller than estimates from the 1970s of $3600\ \mathrm{m}^2$ to $2900\ \mathrm{m}^2$ (*Heath*, 1975)]. Measurements from a cross-channel boat-mounted ADCP survey on 14th April 2014 (see Appendix C) show that the peak flow through the inlet gorge during mean spring ebb is roughly $6000\ \mathrm{m}^3\mathrm{s}^{-1}$, with depth-averaged peak mean spring ebb velocity of $2.3\ \mathrm{m\ s}^{-1}$ (*Sherwood and Nelson*, 1979).

The region is exposed to frequent and high energy wave events, primarily from the southwest. NOAA WaveWatchIII ('NWW3') (http://polar.ncep.noaa.gov/waves/wavewatch/) hindcast wave data from the nearest deep-water node ($38\ °\mathrm{S}, 174.5°\mathrm{E}$) over the 5 years from 2010 to 2015 have a mean significant wave height of $2.1\ \mathrm{m}$ (Figure 2.2a) and a mean wave period of $12\ \mathrm{s}$.

The ebb-tidal delta and adjacent beaches are primarily composed of marine sediments, dominated by fine-grained ($0.18\ \mathrm{mm}$) titanomagnetite sand ($3535\ \mathrm{kg\ m}^{-3}$) (see Appendix B) derived from erosion of the

Quaternary Taranaki andesites originating over $200\ \mathrm{km}$ to the south of Raglan (*Bryan et al*., 2007). Annual alongshore littoral drift was estimated at $175{,}000\ \mathrm{m}^3$ which moves northward along the west coast from Taranaki to the Kaipara Harbour (see Figure 2.1a) (*Hicks and Hume*, 1996). Large-scale sand 'slugs', or semi-localized mounds of sediment, were observed to migrate around the southern headland at Raglan in $10\text{-}15\ \mathrm{m}$ depths during a series of large storms, eventually moving north and eastward diffusing shoreward at roughly $400\ \mathrm{m}$ over 6 months (*Phillips et al*., 2009). It is thought that these deposits are temporarily incorporated into the ebb-tidal delta and adjacent beaches until wave and tidal conditions re-equilibrate the delta and beach morphology. Mud and silt dominate the terrestrial sediments (*Sherwood and Nelson*, 1979) which either remain in the estuary (*McKergow et al*., 2010) or are transported beyond the ebb-tidal delta. The latter assumption is based on the fact that the inlet, adjacent beaches and ebb-tidal delta are composed mainly of fine titanomagnetite sand and lack fine silt and mud (*Sherwood and Nelson*, 1979).

The catchment (or watershed) has a total area of $525\ \mathrm{km}^2$ (*Environment Waikato,* 2002; *McKergow et al*., 2010). There are seven major sub-catchments and many smaller streams that drain to the harbour. The mean annual runoff into the harbour is $0.034\ \mathrm{m}^3\ \mathrm{s}^{-1}\ \mathrm{km}^{-2}$, but experiences dramatic spikes up to $1.0\ \mathrm{m}^3\ \mathrm{s}^{-1}\ \mathrm{km}^{-2}$ during winter and spring flooding events. The maximum daily rainfall recorded at the weather station on Karioi during 2010-2015 was $92\ \mathrm{mm}$ (Figure 2.4d) (*NIWA*, 2015a).

2.3 **Methods**

Five years of video observations (2010-2015) are used to describe the movement of sandbar features at the ebb-tidal delta at Raglan, New Zealand.

2.3.1 Description of the Raglan Cam-Era Dataset

The 'Cam-Era' video observation system was installed by Waikato Regional Council and NIWA, and consists of two video cameras ('Raglan

A' and 'Raglan B') mounted atop a building on the hill top approximately $94\ \mathrm{m}$ above mean sea level at the southern end of Ngarunui Beach, south of the inlet to Whaingaroa Harbour (Figure 2.1b, white triangle). Both cameras point northward with slightly overlapping views. The oblique view of Raglan A covers the terminal lobe and nearshore (Figure 2.1b, grey dotted line), while the oblique Raglan B is oriented slightly east of north capturing the beaches and inlet (Figure 2.1b, white dashed line).

Raglan A and B are both Lumenera LE 375 video cameras, each with a 7.7×6.1 mm color CMOS sensor, 2048×1536 pixel array (i.e. 3.1MP), and a 25.5 -mm fixed-focal-length lens. The cameras are operated synchronously by a locally-housed desktop computer, capturing imagery during daylight hours. The standard collection procedure captures $2{,}400$ image pairs over 20-minutes at 2Hz during every half-hour of daylight. From those images captured, a 20-minute average image is composed for each camera. The images are transferred using ftp each night to computers at NIWA and University of Waikato.

During the 5 years considered in this study, $35{,}363$ 20-minute average image pairs were collected between 1 January, 2010 and 1 January, 2015 over a full range of tidal levels and environmental conditions.

2.3.2 Environmental Data

Tidal predictions are used to approximate the water level at the time that each video image was collected. Water level is needed for image rectification and tidal ranges for each ebb-event are used as a proxy for ebb-jet current strength during the observation period. Two water level gauges were installed at Raglan by the Waikato Regional Council, one located coastally at Manu Bay just south of Ngarunui Beach (Figure 2.1, red dot) and the other at the Wharf, nearly 4.2 km from the inlet within the harbour (not shown in Figure 2.1). Both water level gauges experienced intermittent lapses in measurement during the observation period and so tidal harmonic analysis on the observations was used to create a continuous tidal record for the whole period. The harmonic analysis was based on two years of water level data from the coastal gauge at Manu

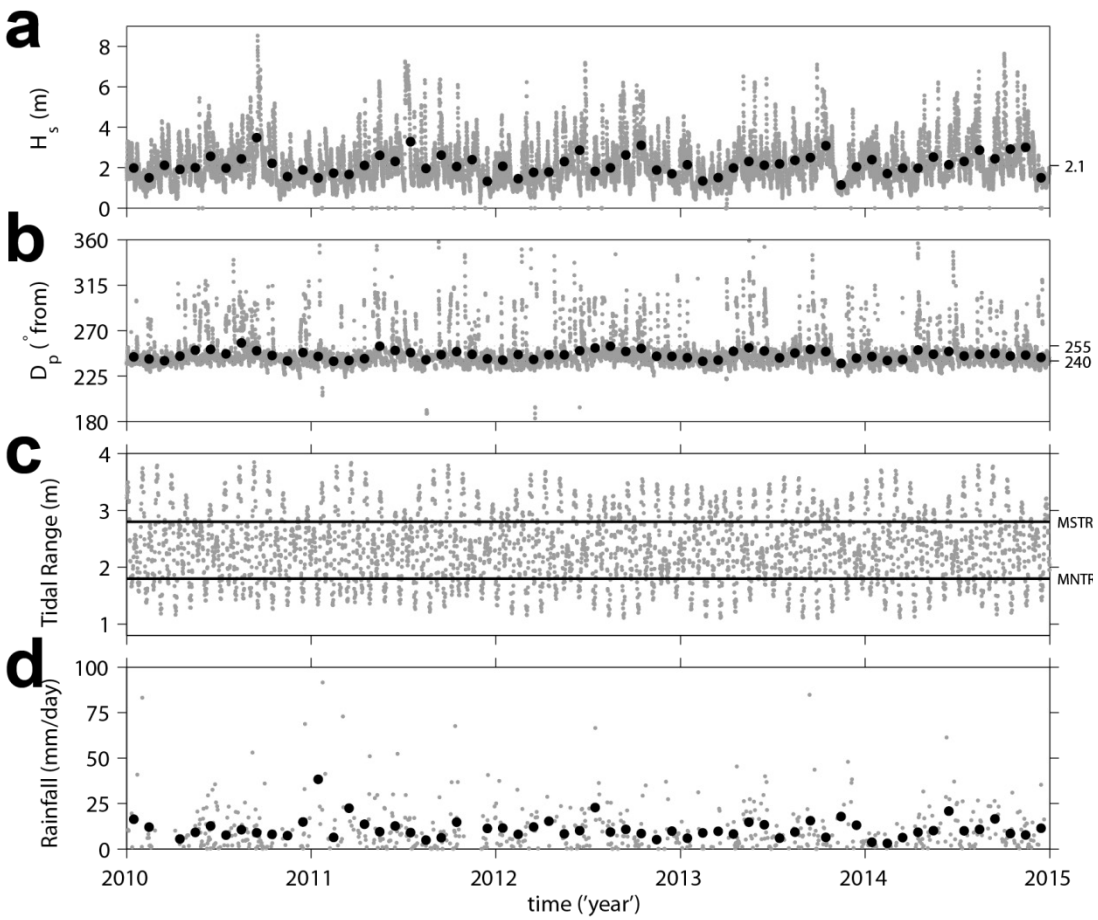

Figure 2.2. Time series of (a) significant wave height H_s, (b) peak wave direction D_p, (c) tidal range, and (d) daily rainfall at Raglan during the period of the study. In (a), (b) and (d), the monthly mean values are also shown with black circles.

Bay [corrected for atmospheric pressure using MSLP data from the Taharoa weather station 40 km toward the south (*NIWA*, 2015b)] and harmonic analysis was undertaken using `t_tide` (*Pawlowicz et al.*, 2002). The difference between the high-tide and low-tide for each ebb-event (or 'tidal range') is shown in Figure 2.2c.

Tidal prediction levels do not capture the wind and wave setup or water level variation due to atmospheric conditions, so there is error associated with using predicted tides rather than water level observations. However, a comparison showed that the predicted tidal levels and observed tides were comparable ($R^2 = 0.98$ and $p < 0.001$). The maximum differences between the observed water levels and the predicted tidal levels during the two years were ± 0.5 m, with 95% of the observed water level values less than 20 cm different from the corresponding predicted tidal level. A metre error in the water level altered the alongshore position in the

rectified video imagery by 8 m to 45 m at the southerly and northerly extents of the ebb-tidal delta, respectively. Spatial differences in water surface elevation in the cameras' fields of view (e.g. from wave set-up and set-down, or from choking of the tidal wave through the entrance) were not accounted for and also introduce error to the spatial position of rectified pixels.

NWW3 global hindcast model solutions for the nearest node to Raglan ($38\ °\mathrm{S}, 174.5°\mathrm{E}$) were extracted and used as a measure of the wave climate during the period of observation (Figure 2.2a and 2.2b). The hindcast data consist of three hourly significant wave height (H_S), peak period (T_p) and peak direction (D_p) data for the period of 1 January 2010 to 1 January 2015. The node is $35\ \mathrm{km}$ WSW from ebb-tidal delta. Wave energy flux (or 'wave power'), $Ec_g = \rho g\ H_s^2 c_g/16$, determined from the NWW3 node data are similar ($slope = 1, R^2 = 0.74, p < 0.001$) to measurements from a non-directional Datawell Waverider buoy located 45 km south of Raglan at the Taharoa ironsand mine (data provided by *Bluescope Steel*). Taharoa is fully exposed to the dominant wave direction, but Raglan is partially sheltered to events from the south to southwest. Local wave refraction and sheltering effects of Karioi are not accounted for in the NWW3 hindcast data.

2.3.3 Image Analysis

To reduce the number of images processed and to minimize variations caused by tidal variations (*Lippmann and Holman*, 1989), we consider at most one single pair of images per day occurring at a common tidal height. By considering a single pair of images per day occurring at or near the low tide value $\eta = -0.5$ m (allowing tolerance when needed, i.e. $\eta \in [-0.4, -0.8]$ m), the number of image pairs considered was reduced to $1{,}643$ from $35{,}363$. This tidal value was chosen because it is slightly higher than the highest low tide and so offers the greatest number of observations likely to capture the depth-limited wave breaking needed to show the morphological patterning around the delta.

Images were selected for further processing from the $1{,}643$ pairs based on visibility and suitable wave conditions. Each image pair was reviewed and assessed manually. Images with dense fog, strong light reflection, absence of breaking waves, or a fully-saturated surf zone were discarded. Of the 1,643 image pairs considered, 81% were discarded leaving 307 pairs used in this study. Due to the increased rate of sun reflection and shorter length of day, there are fewer usable image pairs during winter than in each of the other seasons (e.g. 20% in winter and 29% in spring). June had the least monthly observational representation with only 3.6% of the selected image pairs, whereas January had the most monthly representation with 13.7% of the observations.

Although the cameras are mounted securely on the roof of the Bethel House at Children's Bible Ministry Camp, movement of various scales was detected in the image record. At the scale of seconds, there is pixel-scale movement in the field of view from local vibration in the building structure during wind events or from human movement inside the building. These movements are considered insignificant within each 2400 image burst-sequence used to generate the 20-minute average images, and therefore not treated. During hot summer days, there was an observed movement of up to 10 vertical pixels over 5 km in the field of view attributed to thermal expansion and contraction over the length of the day. Also, occasionally during the 5-year record, the cameras moved substantially due to extreme wind or manual camera cleaning. To account for the larger perturbations in the 20-minute average images, each image of the 307 pairs (i.e. 614 images) was corrected for movement by recalculating the cameras' positions using the geographic coordinates of virtual ground control points observed in each image and the corresponding pixel coordinates in a known reference image for each camera. The cameras' rectifications were previously established using ground control points on land along both beaches and on the water around the centre of the ebb-tidal delta. Figure 2.3 shows a comparison between the wave breaking patterns in a rectified image pair (Figure 2.3a) with the position of shallow bed features in the multibeam bathymetry (Figure 2.3b). Also, the pixel intensity along the

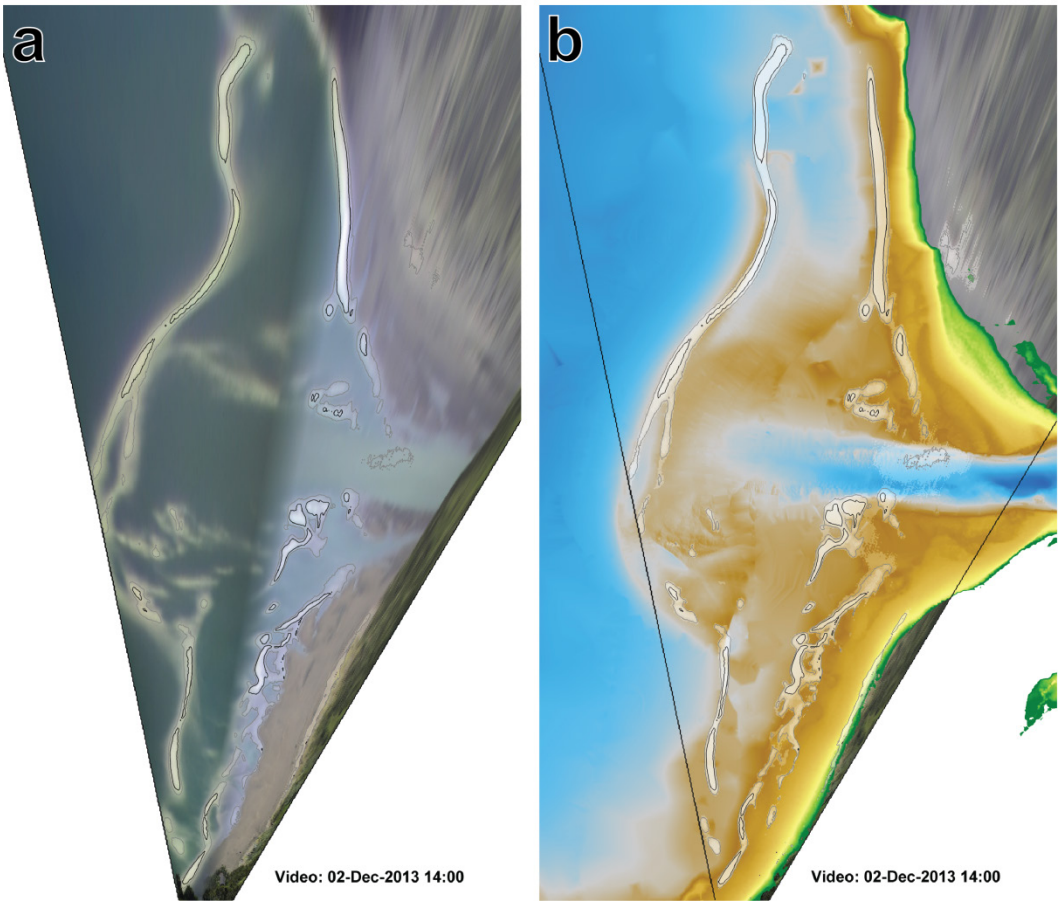

Figure 2.3. Comparison of the geographic position of wave-breaking patterns in the (a) rectified Cam-Era composite (captured 2nd December 2013 14:00) with the (b) position of shallow bathymetric features in the multibeam hydrographic survey (surveyed 18th-20th November 2013). Pixels in the rectified image are contoured and overlain on the multibeam data.

channel thalweg is shown in Figure 2.1c to be highest directly over the shallowest points of the two sandbar crests, suggesting pixel intensity as a suitable indicator of depth-limited breaking atop shallow bed features. The reference image pair used in the comparison was captured during the first occurrence of visible wave-breaking, 10 days after the hydrographic survey.

After rectification, the images were converted from RGB colour space to grayscale and contrast enhanced to improve the ability to distinguish wave breaking by mapping the intensity values of an image to a new range.

Many geomorphic features are easily discernible on the geo-rectified time exposure images of the Raglan Bar. For example, Figure 2.4 is a composite of a geo-rectified image pair which clearly shows sandbars and channels. The positions of three main features were digitized in each

enhanced georectifed image pair: the terminal lobe, mouth bar, and channel margin linear bars.

The terminal lobe is the long bar feature that borders the seaward side of

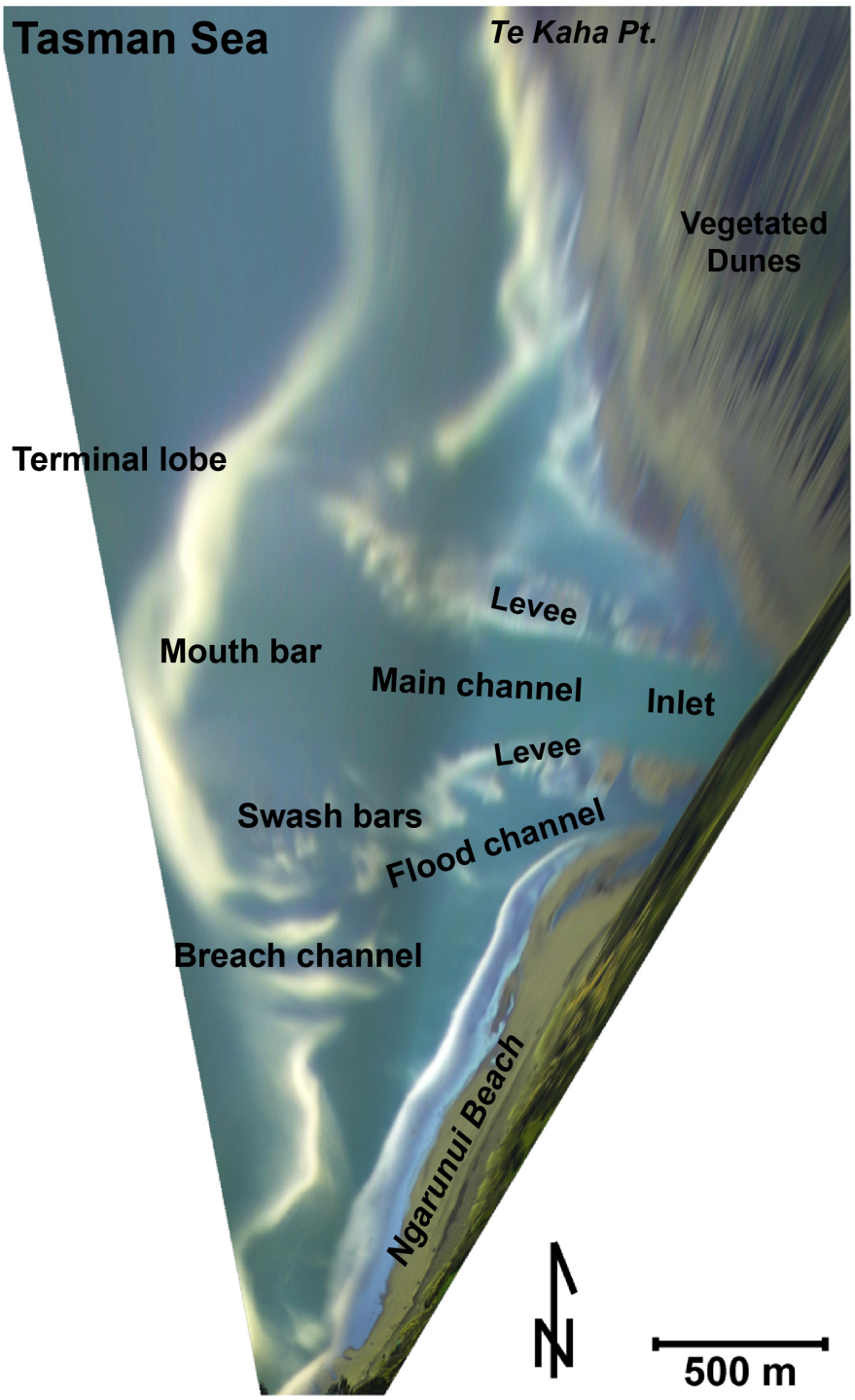

Figure 2.4. Example of geo-rectified time-averaged composite showing detectable geomorphic features of the ebb-tidal delta at Raglan. The terminal lobe, mouth bar, levees, swash bars, main channel, flood channels, and a breach channel in the terminal lobe are recognizable and labelled.

the entire ebb-tidal delta complex, and was identified in the rectified imagery by extracting the coordinates of the furthest seaward maximum of light intensity corresponding to initial depth-limited wave breaking for each alongshore position. Generally at Raglan, the terminal lobe runs alongshore with a cuspate protrusion extending further seaward offshore from the main channel and inlet. The terminal lobe feature was only visible in the Raglan A camera view.

Between the terminal lobe and main channel and within the alongshore bounds of the main channel was a sandbar similar to a river mouth bar – similar in that it formed at the seaward end of the main seaward-directed current jet exiting the inlet – and therefore in this study we call this feature the 'mouth bar'. Here we refer collectively to the central terminal lobe and the mouth bar as the 'ebb-shoal', as they are in line with the ebb tidal stream and waves also shoal and break on them. Typically, the mouth bar is the shallowest feature along the jet axis seaward of the inlet (see depth profile in Figure 2.1c). At typical ebb-shoals, mouth bars are not necessarily distinct from the crest of a terminal lobe, but in this video record they were most commonly observed as two distinct features, and so are included here as separate features.

Channel margin linear bars (or levees) extend seaward from the inlet while bounding the main channel on the north and south. The levee positions were detected in the images as the first occurrence of light pixels both north and south of the main channel thalweg at each cross-shore position from the inlet on the landward side to the mouth bar on the seaward side. The levees were visible in both Raglan A and B camera views and were digitized in each image pair.

The terminal lobe, mouth bar, and channel margin linear bars were present in all of the image pairs. Their geographic positions were rotated into cross-shore (x) and alongshore (y) distance from the inlet and jet-axis [assuming a straight line heading $277°$ from the point $(406{,}505\ \text{mE}, 697{,}730\ \text{mN NZGD2000 Mount Eden Circuit projection})$].

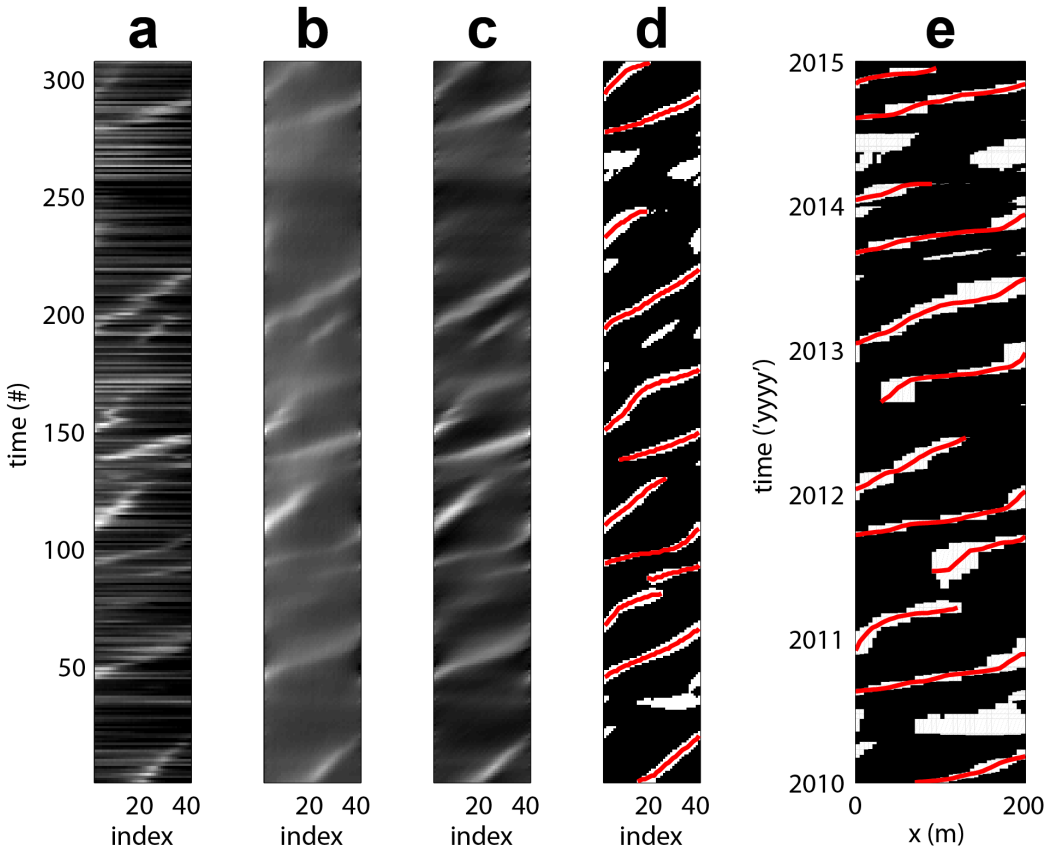

Figure 2.5. An example of the timestacks of pixel intensity along $200\ \mathrm{m}$-long transects centred at one of the nodes, where nodes are distributed around the ebb-tidal delta platform. (a) the raw pixel intensity along the transect at each observation as a timestack in dimensions of observation number and pixel index, (b) de-noised timestack after the first pass of directional filter ($\pi/4$), (c) de-noised timestack after the second pass of directional filter ($\pi/2$), (d) binary timestack after thresholding by pixel intensity, with "ridgelines" of (bar propagation) along white regions identified by red lines, and (e) the translated bar propagation paths in time and space dimensions.

Measurements of the more transient swash bar movements were captured by establishing a grid of nodes over the shallow delta platform and measuring the rate of propagation of high-intensity maxima across transects in both the x- and y-directional components. Time-space plots (or 'timestacks') of pixel intensity along $200\ \mathrm{m}$-long transects centred at each node were generated (shown in Figure 2.5a), de-noised (Figure 2.5b and 2.5c), and used to identify bar propagation rates (Figure 2.5d and 2.5e). The noise was removed using orientation-selective filters which were applied to each of the timestacks in order to highlight structures with dominant orientations within the timestack from the noisy fluctuations of background pixel intensity (*Kovesi*, 2012), which are commonly only in a horizontal orientation (Figure 2.5a). The orientation filters were chosen

manually for each timestack, but typically were values of $\pi/4$ and $\pi/2$ or $3\pi/4$ and π (radians) for bars propagating in the positive or negative directions, respectively. Initially, the timestacks were observed in pixel coordinates (space) and observation number (time) to take advantage of image processing techniques needing evenly spaced data. The ridges of propagating bars were automatically detected in the timestacks by thresholding the de-noised pixel values into a binary array – 1 for pixel intensity above the threshold and 0 below the threshold (Figure 2.5d, white regions are bar propagation paths in image data record space). The threshold value is dynamically determined for each transect as the sum of the mean and standard deviation of the surrounding nine observations (4 observations each side of the one being considered). Connected white pixels were used to determine regional grouping associated with bar propagation paths within each binary timestack using Matlab® function `bwconncomp.m`, and also `regionprops.m` to identify their regional properties. By taking the mean value of the observation number at each pixel location along the length of a connected regional group, a 'ridgeline' of the propagation path was determined (Figure 2.5d, red lines). This was repeated for each of the connected regional groups in each binary timestack at every node in the observational grid domain. The ridgelines and binary timestack arrays were then mapped into real space and time coordinates (Figure 2.5e) by simply converting the indices of pixel location to easting and observation number to time (linearly interpolating between observations when needed). The rate of change between each point along the identified bar crest were used to determine the bar propagation speeds at each node throughout the entire time of observation.

2.4 **Results**

2.4.1 Wave Climate

In the NWW3 hindcast data, the vast majority of wave events came from the WSW direction, with 70% of all events from $240°$ ($\pm 7.5°$) and 16% from $255°$ ($\pm 7.5°$). Only 11% of all wave events originated from west to north or south to southeast. The wave energy flux (or wave power) ranged

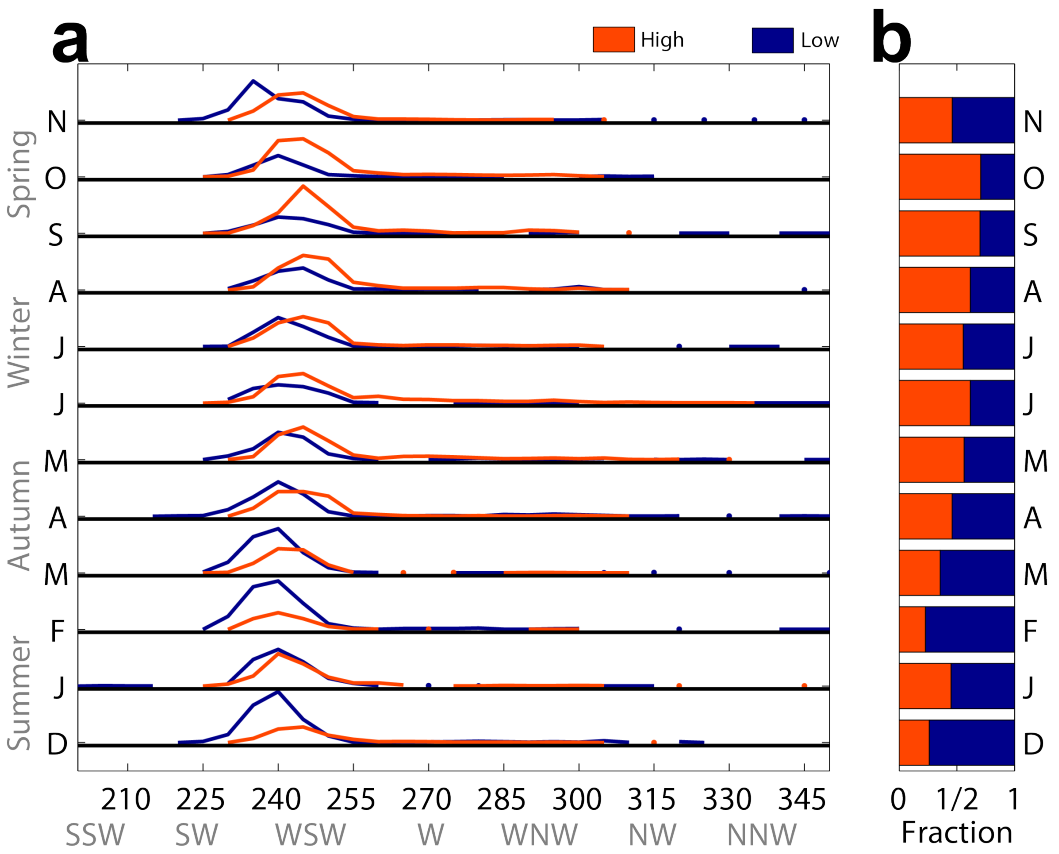

Figure 2.6. NWW3 deepwater wave events (3-hourly) grouped by month with wave events of higher- and lower-energy than the 5-year median in orange and blue, respectively. The relative occurrence is shown by direction (from) in (a) and as a fraction of the total number of wave events each month in (b).

from calm 0 to over $450\,\mathrm{kW\,m^{-1}}$. As the power of the wave events increased, the dominant direction shifted from $240°$ to $255°$ ($\pm 7.5°$). The largest 2% of wave events had power above $168\,\mathrm{kW\,m^{-1}}$ and 67% came from $255°$. A spring equinoctial signal was observed in the significant wave height (Figure 2.2a). Seasonal differences included a greater occurrence of relatively low-energy wave events during November through April (summer and early autumn) and a greater occurrence of relatively high-energy wave events during May through October (winter and early spring) (see Figure 2.6). Figure 2.6 shows a slight shift in wave direction with waves coming mainly from $240°$ during November through March but with an increased frequency from $255°$ during April through October. There were also more occurrences of high-energy events from the west and northwest directions during winter and spring, although few in comparison to the west-southwest.

2.4.2 Terminal Lobe

Over the 5 year observational record, the mean position of the terminal lobe (Figure 2.7a, black solid line) was a nearly symmetric cuspate sandbar covering approximately $2.5\,\mathrm{km}$ in the alongshore direction, located between $1.0\text{-}1.6\,\mathrm{km}$ offshore of the inlet with a seaward bulge directly offshore from the inlet extending $630\,\mathrm{m}$ beyond the lateral flanks. Cross-shore variations between 230 to $750\,\mathrm{m}$ of the mean terminal lobe position occurred during the observational period, which were associated with a change in curvature of the lobe. The largest cross-shore movements were observed at the southern end of the terminal lobe feature approximately $1000\,\mathrm{m}$ south of the jet axis which varied over a range of $750\,\mathrm{m}$, with the northern lobe and central terminal lobe moving 60% and 30-40%, respectively as much as the south.

The 5-year monthly mean cross-shore terminal lobe position was further offshore during winter and spring months than in summer or autumn months (see Figure 2.7b and 2.7c). The monthly mean cross-shore position of the central terminal lobe was the furthest offshore during July, at 2% seaward of the annual mean. The southern arm of the terminal lobe

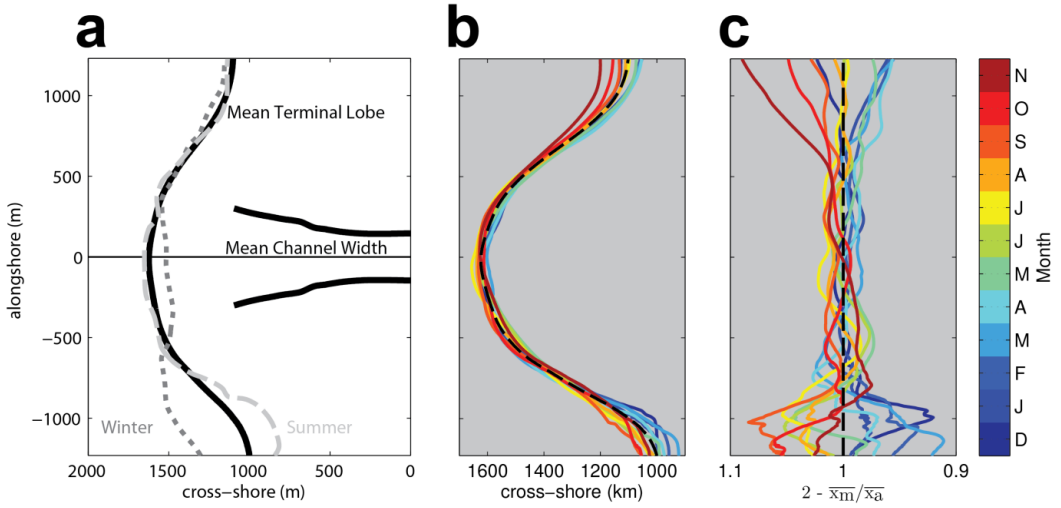

Figure 2.7. (a) The alongshore and cross-shore position of the terminal lobe and distance between levees: 5-year mean in black and examples of summer (5th February 2013, light-grey dashed line) and winter (22nd October 2010, dark-grey dotted line) terminal lobe states. (b) Monthly averaged terminal lobe position, and (c) the difference between monthly averaged cross-shore terminal lobe position and the 5-year mean, with month indicated by colour.

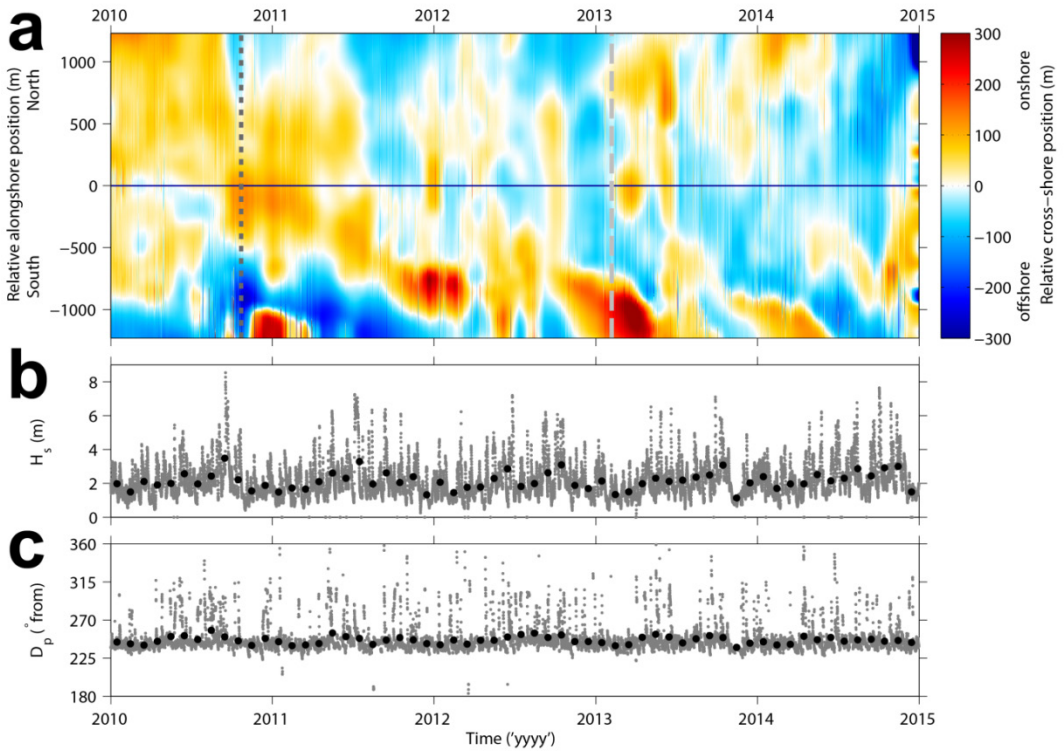

Figure 2.8. (a) Timestack image of the cross-shore position relative to the 5-year mean (as colour) for the alongshore length of the terminal lobe (y-axis) over the observation period (x-axis). The summer and winter example terminal lobe observations from Figure 2.7a are indicated with light-grey dashed- and dark-grey dotted lines, respectively. For reference, concurrent significant wave height (b) and peak direction (c) data is shown.

was over 8% seaward of the annual mean during September, and the northern arm was 9% further offshore than the annual mean during November.

Figure 2.8a shows a timestack image of the cross-shore position relative to the 5-year mean (represented by the colour scale) for the alongshore length of the terminal lobe (y-axis) over the observation period (x-axis). To fill in the gaps between observations, cross-shore positions between observations were linearly interpolated at each alongshore position at half-day observational resolution. The resultant array (image) was then convolved with a low-pass filter with an element sized $25\ \text{days} \times 100\ \text{m}$ to remove excess noise (the smooth background colour data in Figure 2.8a). As verification of the process, the actual observation data were overlaid at each of the 307 observations (the streaks in Figure 2.8a) showing very close agreement.

As seen in Figure 2.8a, there appeared to be a nearly cyclical pattern in the cross-shore terminal lobe movements over time. The pattern appeared as a laterally traveling wave moving away from the jet axis along both arms of the terminal lobe. For an impulse of shoreward movement at the centre of the terminal lobe, the shoreward propagating signal travelled $1\ \mathrm{km}$ south of the jet axis along the southern arm of the terminal lobe over a period of 1.5 years. The signal was less obvious along the northern arm, but moved more quickly taking only half a year to travel 1 km north of the jet axis (Figure 2.8a). The movement of these waves are a signature of the adjustment timescale of the curvature of the lobe, and north-south differences an indication of season changes in symmetry of the lobe. The movements appear to be 'chunky' rather than smooth adjustments, likely instigated by discrete events of suitable combinations of forcing conditions.

The cross-shore position of the terminal lobe was observed to move offshore with increasing wave power. This was largely driven by the cross-shore position of the northern arm of the terminal lobe, which was strongly positively related to the magnitude of wave power, with 75% ($p < 0.01$) of the variation in cross-shore distance attributed to variation in the magnitude of wave power. Variation in the cross-shore position of the southern arm was not significantly related to wave power, but did show sensitivity to the wave direction angle and the alongshore contribution of wave power. The relationship between cross-shore distance from shore at the southern arm and wave power was positive but weak ($R^2 = 0.15,\ p < 0.001$). The integral of cross-shore distance from shore of the terminal lobe over the alongshore extent of the terminal lobe (a potential proxy for delta volume) was largest during winter (July through November), and smallest during summer (January through April).

2.4.3 Mouth Bar and Central Terminal Lobe

The mouth bar and central terminal lobe both moved seaward and shoreward roughly perpendicularly to the jet axis over the 5-year observational record. The cross-shore position of the mouth bar ranged from $1{,}306$ to $1{,}550\ \mathrm{m}$, with a mean of $1{,}445 \pm 45\ \mathrm{m}$, seaward of the inlet. The cross-shore position of the central terminal lobe ranged from $1{,}420$ to $1{,}733\ \mathrm{m}$, with a mean of $1{,}615 \pm 52\ \mathrm{m}$, seaward of the inlet. Both the central terminal lobe and mouth bar trended seaward in time after an event in late 2010 when both features suddenly moved over one hundred metres shoreward, which appeared to occur again in early 2013 although to a lesser extent. The separation between the mouth bar and the terminal lobe was as large as $285\ \mathrm{m}$, with largest differences occurring during

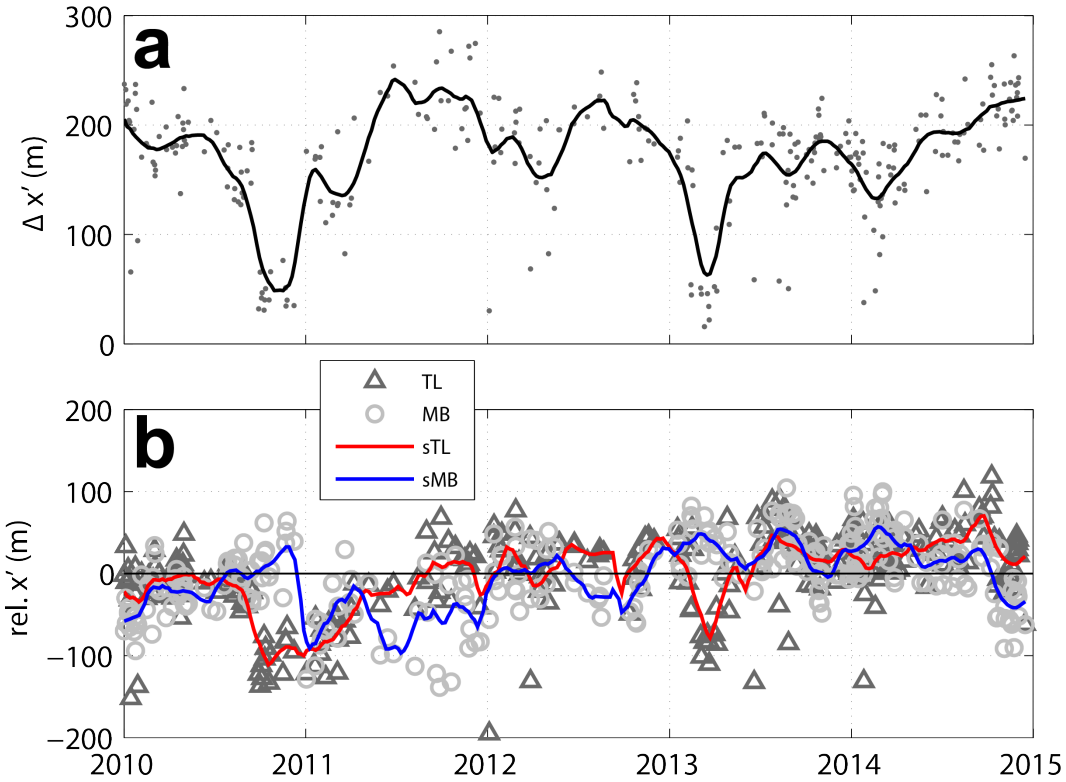

Figure 2.9. (a) The difference between cross-shore distance from the inlet of the central terminal lobe and the mouth bar measured in each observation (grey dots) and 30-day running mean (black line). (b) The relative mean cross-shore position ($x - \bar{x}$) of the central terminal lobe (dark-grey triangles) and the mouth bar (light-grey circles) during each observation, and with a 30-day running mean of the central terminal lobe (red line) and mouth bar (blue line)

winter and the most merging events (cross-shore separation of less than $50\ \mathrm{m}$) occurring during spring, summer, and autumn (Figure 2.9a). The joining of terminal lobe and mouth bar was a combination of the central terminal lobe moving shoreward and the mouth bar moving offshore (Figure 2.9b). The terminal lobe and mouth bar were not observed to join during winter.

Correlation of the cross-shore mouth bar and central terminal lobe positions with wave and tidal forcing conditions was weak. The cross-shore position of the mouth bar was positively related to daily maximum tidal range with an $R^2 = 0.10$ and $p < 0.001$, but not significantly related to wave power. The central terminal lobe was positively correlated to both daily maximum tidal range and 2-day mean wave power but weakly: $R^2 = 0.05$ and $p < 0.001$ for each.

2.4.4 Swash Platform

Sandbars were observed propagating along the swash platform at all of the 54 nodes examined. The rate and direction of bar movements was discernible at each node between each observation using the method described in 2.3.3 (Figure 2.10).

Table 2.1 describes the bar migration rates for the full delta (54 nodes). The 5-year mean bar migration rate over all nodes was $1.8\ \mathrm{m\ day^{-1}}$ with rates up to $7.7\ \mathrm{m\ day^{-1}}$ (98$^{\mathrm{th}}$ percentile). 39% of the estimated rates were greater than $1.0\ \mathrm{m\ day^{-1}}$ and 18% were greater than $2.0\ \mathrm{m\ day^{-1}}$. The migration rates at Raglan are slightly faster than observations of meso-

Table 2.1. Bar migration rates averaged for all nodes over the swash platform.

All Nodes	Mean (m/day)	25$^{\mathrm{th}}$ % (m/day)	50$^{\mathrm{th}}$ % (m/day)	75$^{\mathrm{th}}$ % (m/day)	98$^{\mathrm{th}}$ % (m/day)	>1.0 m/day (%)	>2.0 m/day (%)	>3.0 m/day (%)
5-years	1.8	0.7	1.2	2.2	7.7	39	18	10
Summer	2.0	0.7	1.3	2.5	8.4	40	20	12
Autumn	1.7	0.7	1.3	2.1	6.3	37	16	8
Winter	1.5	0.5	0.9	1.8	7.0	27	12	7
Spring	2.1	0.9	1.4	2.6	8.4	50	25	15

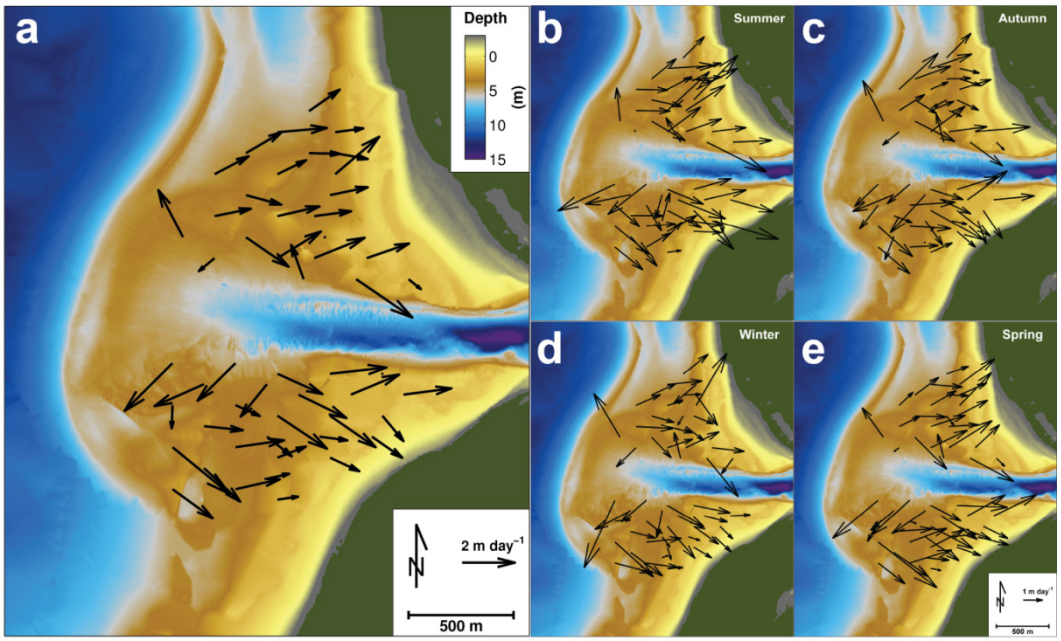

Figure 2.10. Migration patterns of swash bars along the swash platform; (a) 5-year mean, (b) summer, (c) autumn, (d) winter, (e) spring. Note the change in quiver scale between (a) and (b)-(e).

scale sandbars at New River Inlet, North Carolina (recall, mean = $1.5\ \mathrm{m\ day^{-1}}$ and max = $3.5\ \mathrm{m\ day^{-1}}$) (*Pianca et al.*, 2014).

The 5-year mean vector-averaged bar propagation rates are shown in Figure 2.10a, which shows a general pattern of onshore-directed movement along the delta flanks and nearshore, with offshore movements at the seaward end of the main channel margins. At the seaward end southern margins, the average direction is towards the southwest (i.e. away from the channel and seaward). On the seaward side of the southern flank, the average movements were directed southeast (i.e. alongshore away from channel and shoreward). On the shoreward side of the flank and nearshore, the mean movements were directly onshore. Near the inlet, the bar movements moved slightly north and shoreward towards the inlet. Along the seaward side of the northern channel margin, the mean bar movements were directed northwest, away from the channel and seaward. Mean bar movements along the entire northern flank and nearshore were directed shoreward and slightly to the north. Near the inlet on the northern channel margin, the mean bar movement was directed south and shoreward towards the inlet.

Grouping the nodes into common regions based on their 5-year vector-averaged mean movement, we identify 6 regions: seaward channel margins, inlet channel margins, southern flank, southern nearshore, northern flank and northern nearshore.

Comparing the bar propagation rates over the 5 years by wave condition, the fastest and slowest bar propagation rates occurred during relatively low-energy wave events ($Ec_g \leq 15\ \mathrm{kW\ m^{-1}}$). The variability of migration rate decreased with increasing wave energy while the mean speed slightly increased with increased wave power (but were less than the 75th percentile of migration speeds at low wave energy. At the north and south flanks and nearshore areas, the orientation of migration became more directly onshore with increased wave energy. At the seaward end of the channel margins, the migrations became oriented at $\pm 40°$ from directly offshore on the north and south of the channel respectively. Movements at the seaward channel margin increased in speed and were more strongly directed directly offshore with increased tidal range. Movements at the

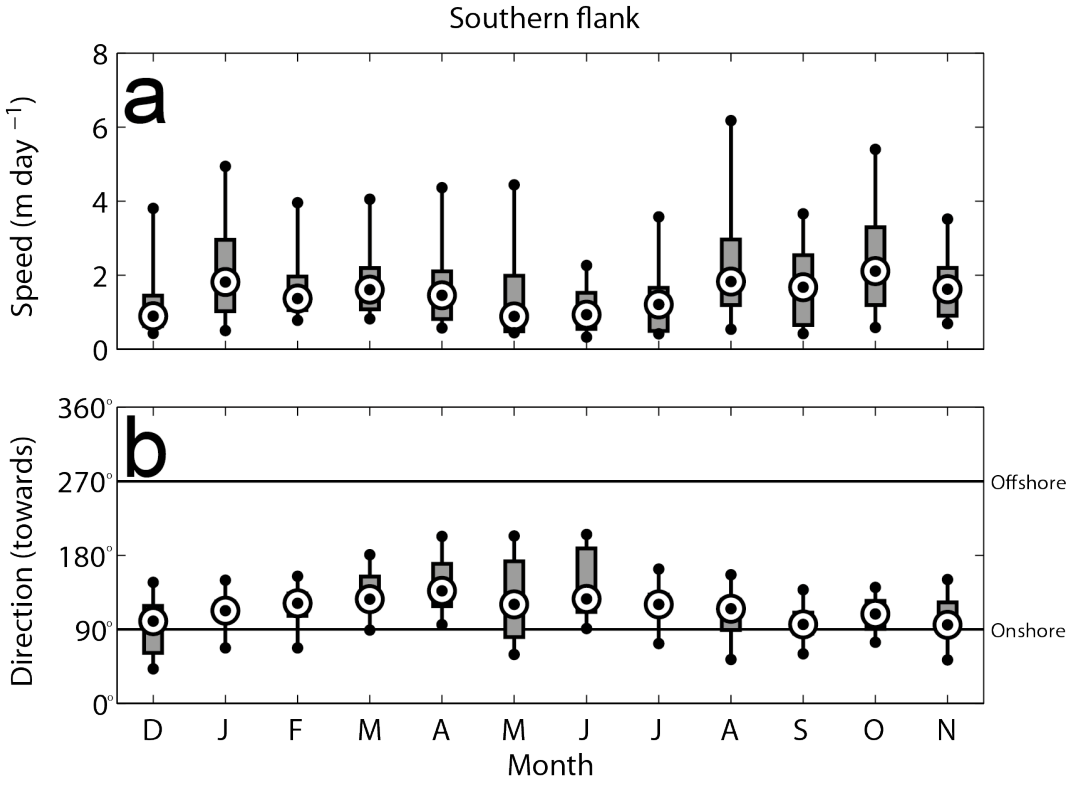

Figure 2.11. Seasonal variations in bar migration rates (a) and direction (b) averaged over the southern flank nodes.

southern flank also increased in speed with increased tidal range, and were directed more directly shoreward. The other regions did not show clear signs of dependence on tidal range.

Seasonal trends (by month) for each region were also evident. The transitional periods from winter to spring (i.e. August through October) and from summer to autumn (i.e. January through March) had the fastest bar propagation rates at all regions except for the southern nearshore (e.g. Figure 2.11a). Bar movements in the southern nearshore were fastest during spring and summer when they were directed directly shoreward and slowest during the transition from autumn to winter (i.e. April through July) and directed alongshore north toward the inlet. The inlet channel margins experienced fastest movements during the summer and slowest during winter, with the orientation changing from strongly inward toward the channel and inlet throughout winter to more directly onshore during spring. The northern nearshore region had fastest bar movements during summer (shoreward) and during winter to spring transition (alongshore northward). Movements at the northern nearshore often moved south toward the inlet during the spring to summer transition. The northern flank experienced fastest movements during August, and was directed shoreward year-round. The direction of movements at the southern flank was directed shoreward during summer but more northeast during autumn and winter (Figure 2.11b). Movements at the seaward channel margin region were usually directed seaward and outward from the channel, but almost 50% of the bar movements during spring and summer were directed shoreward.

2.4.5 Channel Margin Linear Bars

The main channel extends seaward from the inlet, and is bounded laterally by channel margin linear bars (or levees). Channel width measurements over the 5-year record are shown in Figure 2.12. In general, the width of the channel increased with distance from the inlet. Over the 5-year observational record, the inlet width was between $240\ \mathrm{m}$ and $350\ \mathrm{m}$ wide with a mean and standard deviation of $290 \pm 30\ \mathrm{m}$.

The width of the inlet in the video observations was narrower than the distance measured on the multibeam hydrographic data, which were between $380\ \mathrm{m}$ and $430\ \mathrm{m}$ for tidal levels of $\eta = -0.4\ \mathrm{m}$ and $-0.8\ \mathrm{m}$ (the water level range for images). *Lippmann and Holman* (1989) indicate that tidal variations can affect the position of features in the images, however there was not a significant relationship between the inlet width and the predicted tidal level during our observations, although the predicted tidal level varied within the range $\eta \in [-.8 - .4]$. Therefore the variations in inlet

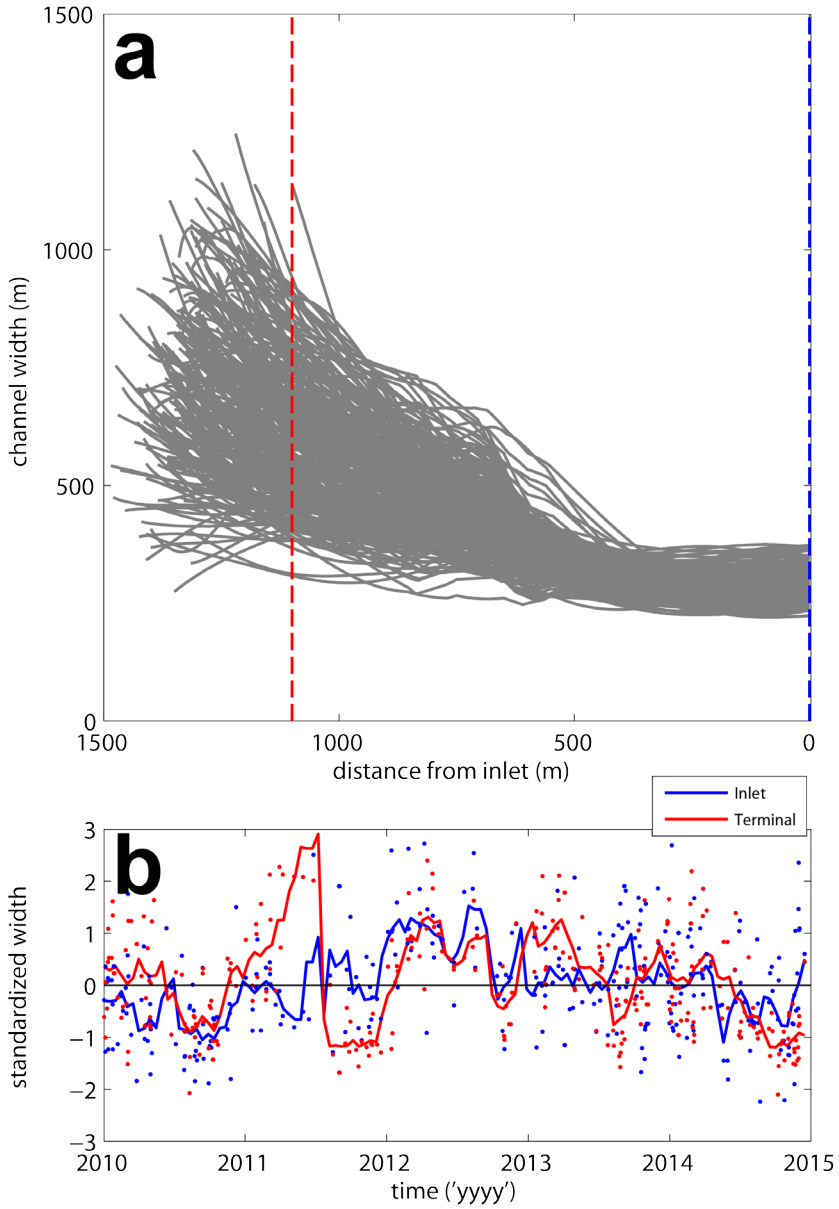

Figure 2.12. (a) Channel width (distance between levee bar features) measurements over the 5-year observational period, over the length of the channel, and (b) standardized width at the inlet (blue) and $1100\ \mathrm{m}$ seaward of the inlet (red).

width must be attributed to actual changes in the width of the inlet, error associated with the inlet width detection procedure, error in the approximation of water level height using tides, or error introduced to during the image rectification process. The last two error sources would be the same for the seaward and landward end of the channel, and do not account for the difference in variability seen between the two ends (Figure 2.12b). The most likely source of the variability is due to the procedure of digitizing the levee position, as the region around the inlet rarely had waves breaking on it and the contrast between black sand and water was difficult to distinguish in low-light images (see Figure 2.4 for an example).

Relative to the rest of the channel, the channel width along the first $500\ \mathrm{m}$ of the channel seaward of the inlet was very consistent in time. At $500\ \mathrm{m}$ seaward of the inlet, the mean channel width was $330 \pm 30\ \mathrm{m}$.

The seaward half of the channel, however, varied more substantially. The mean width of the seaward (or terminal) end of the channel, $1100\ \mathrm{m}$ from the inlet, was $600 \pm 140\ \mathrm{m}$ with widths ranging between $410\ \mathrm{m}$ to $860\ \mathrm{m}$.

2.5 Discussion

2.5.1 Evidence of Dynamic System

The geomorphic features of the ebb-tidal delta at Raglan were observed to move in response to forcing patterns. There was significant dependence on the magnitude and direction of wave energy flux, and the strength of the ebb-tidal jet. No single type of forcing was able to directly account for all of the observed variation in feature positions, which implies that the geomorphic features are controlled by multiple types of forcing and interconnected with each other as part of a larger morphodynamic system.

Despite temporary displacement, the primary delta features (terminal lobe, mouth bar, and channel margin linear bars) maintained a similar general arrangement over the 5 years of observation. The average positions of these features can be considered as morphological steady states, characterized by the average forcing regime and sediment supply present at Raglan over various time-scales (e.g. monthly vs annual wave climate).

During highly energetic events (e.g. extreme wave event), the positions of the terminal lobe, mouth bar and channel marginal linear bars were all reset into a new arrangement. Over time, the features migrated back toward their long-term average position, suggesting some kind of attractor for the morphodynamic system.

Movement of the delta features was intermittent, marked by periods of active movement between periods of inactive stillness. This behaviour is seen in Figure 2.8a: the 'chunky' movements of the terminal lobe are evidence that movements occur during particular forcing events as transitions between less active periods when the terminal lobe remains still. This notion is further supported by the observation of swash bar migration rates on the delta flanks and channels being fastest during the transitional period of winter to spring and summer to autumn when the wave climate changes.

2.5.2 Seasonal Trends

Delta-scale changes were observed to coincide with seasonal wave intensity variations. From late spring to mid-autumn (November through April), the wave climate had lower-than-average energy. From December through March, the terminal lobe was more cuspate with the lateral arms oriented further shoreward than average (Figure 2.7b and 2.7c). Also, sandbar propagation rates were faster throughout most of the delta during summer to autumn. The smaller summer waves appear to encourage restorative onshore sediment flux throughout the delta. This idea is supported by the observed summer progradation of Ngarunui Beach south of the inlet (*Wood,* 2010).

Swash bar propagation also related to seasonal changes in forcing conditions. For example, the direction of sandbar migration coincided with slight changes in dominant swell direction. For instance, at the southern nearshore region there was a transition in the orientation of swash bar movement from directly shoreward during spring and summer to alongshore during autumn and winter. This transitional period coincided with a change in the dominant wave direction, where summer was

characterized by mainly low-energy waves from 230-245° and autumn and winter by high-energy waves from 250-255° with increased occurrence of northwesterly events. The position and orientation of the southern headland (Karioi) is such that it shelters Ngarunui Beach from most of the south to southwest swell. The typical summer wave conditions travel nearly parallel to the headland toward the southern flank of the ebb-tidal delta, and therefore have an angle of incidence that contributes very little to the alongshore sediment transport (e.g. *Komar*, 1971) compared to the wave events of autumn and winter to which the delta is more exposed. Also, the region around the southern arm of the delta is constrained by the beach and headland, which might lead to the formation of circulation cells directed by return flow of excess surface flow associated with wave setup (S*hi et al.,* 2011; *Olabarrieta et al.*, 2014). Presumably the orientation of such a circulation cell would be sensitive to the direction of advancing waves. Unfortunately there are no measurements or model output to confirm this hypothesis.

The cross-shore position of the northern flank and central terminal lobe were observed to be significantly related to the magnitude of wave energy flux. The southern arm of the terminal lobe however was not, but sensitive to the direction of wave events. The sheltering effects of Karioi likely contributed to these observations. The central and northern reaches of the terminal lobe are more exposed to the wave conditions from 240° (consisting of 70% of wave events) than the southern end of the terminal lobe and beach. The alongshore momentum and sediment flux would be oriented northward along the terminal lobe in exposed areas, but the effect would not be symmetrical in regions in the lee of the headland (e.g. *Hart and Bryan*, 2008), which is less exposed. Because of this mechanism occurred so frequently, the northern arm was regularly maintained by currents with conditions suitable to transport available sediment along its extent toward the north.

The changing alongshore position of the levees varied more quickly than anticipated based solely on growth due to sediment transfer from the ebb-

jet to channel margins (*Rowland et al.*, 2010). The sudden changes in distance between levees were likely to be caused by the cross-shore sediment flux observed as transient swash bar features migrating into the channel margins during high-energy wave events, which was visible when reviewing the video data as an animation. This is supported by the observation of swash bar migration along the southern flank changing direction from onshore to a more channel-directed northeast heading during autumn and winter when the wave energy was higher. The seaward channel margins also experienced increased seaward bar migration rates during autumn and winter, which was likely associated with the outward flux of sediment delivered into the channel margins from the southern flanks (see Figure 2.10).

2.5.3 Non-Seasonal Patterns

The cross-shore distance (Figure 2.9b) from the inlet and the central terminal lobe and mouth bar, and also the distance between the central terminal lobe and mouth bar (Figure 2.9a) varied over the 5 years, but those patterns did not correspond with seasonal changes. For example, the mean distance of the combined ebb-shoal (the central terminal lobe and mouth bars together) moved seaward during 2010 until spring when it quickly moved shoreward by $100\text{-}200\ \mathrm{m}$ and the mouth bar and central terminal lobe joined. Then, the ebb-shoal moved back seaward gradually over two full years until the central terminal made another quick but temporary movement, lasting only 4 months, shoreward by $150\ \mathrm{m}$ before continuing seaward until the end of 2014. It is not clear from the data what actually caused this behaviour, but we speculate that the separated and joined arrangements are similar to the high- and low-energy states observed on beaches (*Wright and Short*, 1984; *van de Lageweg et al.*, 2013). The long-term slow seaward migration of the ebb-shoal with quick but interannual shoreward transitions is likely evidence that the delta is growing beyond its ability to maintain itself or moving past ‘maturity’ into ‘old age’ stage of a geomorphic cycle (*Oertel*, 1977). In other words, the delta grows large during an extended period of high-energy events (e.g. stormy that average winter in ENSO cycle), then as the wave climate

decreases in spring and summer (or another year in the cycle), the delta size is no longer supported by the wave climate and is eroded at the seaward extent in the form of swash bars migrating shoreward to renourish the beaches and nearshore. This could be related to variation in sediment supply delivered to the region (e.g. *Phillips*, 2004), interannual climatic oscillations (e.g. ENSO or PDO), or maybe even a natural tipping point (e.g. *Sheffer*, 2010).

The distance between levees also appeared to have a non-seasonal pattern. Figure 2.12b shows the standardized width $(w - \overline{w})/\sigma(w)$ between levees at the inlet (blue) and $1100\ \mathrm{m}$ seaward of the inlet (red). The two standardized widths appear to have tracked each other for much of the time, but differ frequently as well. A long term widening in the inlet beginning after winter 2010 peaked mid-2012 and returned to the more narrow position in winter 2014. The terminal end of the channel showed very similar behaviour, but had a few very large and sudden width changes, e.g. widening to nearly $1200\ \mathrm{m}$ during autumn to winter 2011, with a sudden narrowing to nearly $450\ \mathrm{m}$. The sudden narrowing of the terminal end of the channel is observed in the video as the introduction of new swash bars along the channel margins.

We speculate that the widening and narrowing of the channel (and distance between levees) is due to interaction between the ebb-tidal jet and the ebb-shoal. When the ebb-shoal is further onshore and strong opposing waves are present, the momentum of the ebb-jet is essentially blocked at the terminal lobe and must spread laterally, causing the channel to widen. When waves are not present, the ebb-jet can freely debauch seaward and levees form more closely to the jet core axis (*Rowland et al.*, 2010). This is reflected in the observations because the seaward end of the channel often narrows by the sudden formation of swash bars in the channel margins following very high energy storms. The data do not confirm this idea, but is likely due to the introduction of transient features into the channel margins during very high-energy storms.

It is very likely that much of the discrepancy limiting strong correlation between forcing conditions and observed responses is due to the existence of 'equilibrium' morphology associated with particular forcing conditions. If equilibrium morphology existed, then despite how the morphology was arranged before a particular forcing event, the morphology would trend toward the equilibrium position associated with the forcing condition causing the change. The existence of such 'attractor' positions is common in nonlinear dynamical systems (e.g. *Kuznetsov*, 1998).

2.5.4 Potential Sources of Error

The method of identifying the position of channel margin linear bars (or levees) was a source of potential error as it required waves to break along the shallow margins. However, there were many times when wave energy dissipation at the terminal lobe does not leave enough wave energy to induce depth-limited breaking on the channel margins. Also, the method potentially identified swash bars *near* the channel rather than the actual boundary of the channel.

The position of channel margin linear bars should not be used to indicate the width of the ebbing tidal jet. In general an ebb-jet is bounded laterally by levees but does not necessarily need to be as wide as the existing channel. For example, a jet flowing into an open basin is not bounded by levees, but still has a finite width determined by the rate of lateral momentum transfer (e.g. *Özsoy and Ünlüata,* 1982; *Ismail and Wiegel*, 1983). Opposing waves and bed-shear stress increase the likelihood of the jet being bounded by existing levees by enhancing the spreading of an ebb-jet (*Ismail and Wiegel*, 1983; *Nardin et al.*, 2013). However, in video-based observations of depth-limited breaking patterns along the channel margins that are relatively far apart (e.g. $4 \times$ inlet width), we should not necessarily assume that the ebb-jet filled the entire distance over the full length of the channel. Unfortunately, the spatial jet structure and current were not easily discernible in the video observations at Raglan. Pairing video observations with an HF radar array could potentially provide

additional relevant data such as surface current speed, local wave attenuation, and spatially variable water levels to better discern ebb-jet structure, local wave attenuation and pressure gradients, and water levels.

When choosing images to process from the full record, a tolerance for tidal level during the images was $\eta \in [-0.4, -0.8]$, which introduces variation to the observed channel width measurements based on the different height of the water surface relative to the sloped intertidal bathymetry. The channel width in the multibeam data at the inlet for these water levels was between $430\ \mathrm{m}$ and $380\ \mathrm{m}$, respectively which could account for some of the variation in inlet width. On the other hand, sandbars are clearly seen entering the inlet along the channel margins when reviewing the video animation, implying that there was plenty of sediment available for the potential contraction of channel width at the inlet. However, the current is so fast in the inlet gorge that the bars are not likely to remain at the inlet for long.

The irregular sampling rate of usable observations presented in this study is a potential source of error. There were more observations during spring and autumn than winter or summer, with June and December having the least clear observations of wave breaking. Over the 5 years, there were only 11 events observed during June and 16 during December. The low number of observations in June is attributed to the short length of day, light reflection from low sun elevation, and inclement weather (e.g. fog, rain, clouds). On the other hand, long daylight hours and clear weather typify Decembers, but a calmer than average wave climate provided few events to observe depth-limited breaking. The relatively low sampling count during these months precludes statistically robust inference, but is still more frequent than traditional sampling methods could occur.

Observation of winter sandbar movements was hampered by the lack of clearly visible conditions. Winter storms were typically highly-energetic and coupled with stormy weather which, due to saturated surfzone conditions and/or an obstructed view, inhibited the ability to observe depth-limited breaking. Perhaps the frequency of clear observations during winter was

too slow to capture the fast bar migration during the high-energy wave events.

Although the fit between NWW3 data and nearshore observations at Taharoa are close, the wave data does not include any wave refraction effects likely to occur at Raglan from waves wrapping around the headland. Local conditions will have an alongshore gradient in wave height and a change in nearshore wave direction due to the shadowing effect of Karioi.

Wind at Raglan is frequent and often severe. The wind effect in the current, local waves, and sediment transport are considerable. However, we consider their contributions to be of higher order than wave and ebb-tidal current forcing and neglect them in this study.

2.6 **Conclusions**

Video observations of depth-limited wave-breaking patterns at the ebb-tidal delta at Raglan, New Zealand were used to identify geomorphic features over a 5-year period. Movements of the terminal lobe, mouth bar, channel margin linear bars, and swash bars were described and related to wave and tidal forcing. The video-based technique was able to provide frequent observations over the 5-year period during conditions that would not be possible for boat access, and with little physical effort.

The terminal lobe, mouth bar, and channel levee positions showed short-term variation about a long-term average, largely explained by the seasonal and interannual wave and tidal trends. Movements throughout the delta were intermittent between less active periods. For example the terminal lobe was observed to move intermittently, transitioning between more stable arrangements during transition events. Further, the rate of swash bar migration was fastest during the transition between seasons, namely winter to spring and summer to autumn.

The cross-shore terminal lobe position was sensitive to the magnitude and direction of wave events, with the northern arm being most sensitive to magnitude and the southern arm sensitive to direction. There was

seasonality in the cross-shore position throughout the terminal lobe corresponding to seasonal wave trends, namely the higher occurrence of low-energy waves from south of WSW during summer and autumn and high-wave energy waves from WSW with increased occurrence of events from the W and NW during winter and spring. The central terminal lobe was furthest offshore during July, whereas the northern and southern arms were furthest offshore during spring. Swash bars on the delta flanks propagated shoreward fastest during spring through autumn, swash bars near the beaches moved fastest during winter and spring, and bars near the channel moved fastest during winter.

Non-seasonal patterns were observed, particularly in the cross-shore position of the ebb-shoal, distance between the central terminal lobe and mouth bar, and alongshore distance between levees.

The lack of direct relationships between observed morphological change and forcing conditions indicates that the ebb-tidal delta is a morphological system which to some degree is self-organized.

Chapter 3

A Semi-Analytical Model for an Unstratified Jet in the Presence of Waves

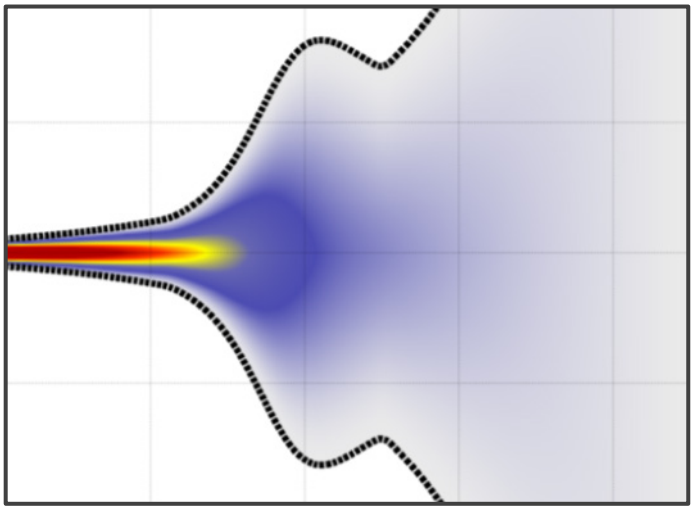

Harrison, S.R., Bryan, K.R., Mullarney, J.C., Winter, C., Elgar, S., Raubenheimer, B. (in preparation). A semi-analytical model for an unstratified jet in the presence of waves. *Journal of Waterway, Port, Coastal, and Ocean Engineering*.

Contribution of Authors

Chapter 3 presents the article entitled “A semi-analytical model for an unstratified jet in the presence of waves”, which is in revision for submission to *Journal of Waterway, Port, Coastal, and Ocean Engineering*. This study examines the fundamental hydrodynamic processes occurring at ebb-tidal deltas by developing a semi-analytical model for an unstratified jet in the presence of waves. It provides a significant contribution to the scientific field by extending previous work on analytical jet models by including the first-order effects of waves (and wave dissipation) on ebb-jet current speed, extent, and width. Also, the model is verified against laboratory measurements and numerical simulations on flat bathymetry with unbroken waves, and verified against detailed field measurements from New River Inlet, North Carolina.

The flow and wave measurements at New River Inlet were gathered as part of a large multi-agency experiment in 2012 and were kindly provided by Britt Raubenheimer and Steve Elgar (both at Woods Hole Oceanographic Institute, Applied Ocean Physics & Engineering). The raw instrument data was processed and checked for quality by Britt and Steve prior to delivery. I further processed and analysed all the data for the purpose of this study. The semi-analytical model formulation and software was developed and written by myself, with helpful feedback from Karin R. Bryan and Julia C. Mullarney. I wrote all of the numerical code to process, analyse, visualize, and compare model output and observations, prepared all of the figures, and wrote the initial and subsequent drafts of the article. My co-authors, Karin R. Bryan, Julia C. Mullarney, Christian Winter (Universität Bremen), Britt Raubenheimer and Steve Elgar edited drafts, provided helpful direction, and editorial help with response to reviewers’ comments.

Abstract

A semi-analytical model is developed to predict the current strength and extent of a tidal inlet jet over an ebb-tidal delta in the presence of opposing waves. The model uses the 2-D momentum and continuity equations, which balance inertia, bed friction, turbulent mixing, and simplified wave-current interaction. The model is evaluated by comparing predictions with laboratory observations, published numerical simulations using a fully 2-D model of currents at a river mouth, and field observations of ebb-tidal currents at New River Inlet, North Carolina. The model qualitatively reproduces the behaviour of ebb-jets with and without the presence of waves, including the exponential decay of the centreline current and the exponential growth of the jet width with distance along the flow, enhanced jet-spreading with opposing waves, and a decreased ebb-jet extent with increased wave energy. Modelled turbulent jet currents closely match those from flume experiments without waves on flat-bottom bathymetry. Predicted currents also closely match numerical simulations of river jets with non-breaking, directly opposing waves on flat-bottom bathymetry. If a channelization parameterization is incorporated into the model, the predictions compare well with field observations of the along-jet current structure (Adjusted Relative Mean Absolute Error, ARMAE < 0.1). The model is mainly limited by underrepresentation of higher-order processes, of which effects are assimilated into the bed-shear stress term. Also, self-similarity arguments enable the reduction of model complexity, but also limit the application and ability to resolve currents outside of symmetric ebb-jets. The model over predicted the impact of waves on the current over the ebb-shoal for larger waves.

3.1 Introduction

Tidal currents and waves create complex systems of bars and channels on ebb-tidal deltas, which occur on the seaward side of tidal inlets (*Van der Vegt et al*., 2006). These deltas shelter inlets by dissipating and redirecting wave energy (*Fitzgerald*, 1984; *Oertel*, 1988; *Sha*, 1989; *Hicks and Hume*, 1996), provide a mechanism for sediment bypassing the inlet

(*Syvitski and Saito*, 2007), and affect maritime navigation. Despite the importance of ebb-tidal deltas, the hydrodynamic processes governing their development and evolution are not understood fully (*Fagherazzi and Overeem*, 2007).

During ebb, a jet of water ('ebb-jet') flows from an inlet across the ebb shoal into the sea. The current jet spreads laterally in response to the morphology (*Kilcher and Nash*, 2010), the density structure (*Wright*, 1977), and the interactions with incident surface gravity waves (*Ismail*, 1980). The incident surface waves are influenced by the morphology, as well as by their interaction with tidal currents (V*an Rijn*, 1990). As waves propagate shoreward their energy focuses on the shallowest part of an ebb-tidal delta. For conditions with sufficiently large wave energy, depth-limited wave breaking will occur, maximizing the effect of waves on the ebb-tide currents and driving shoreward flow over the ebb shoal and into the inlet (*Malhadas et al.,* 2009, *Bertin et al*., 2009, *Olabarrieta et al.*, 2011, *Dodet et al.*, 2013, *Wargula et al.*, 2014, *Orescanin et al*., 2014).

Ebb-jets are difficult to observe in the field owing to the spatial and temporal inhomogeneity of the flow. Observations suggest that bottom friction plays a critical role in controlling the shape of an ebbing tidal jet (*Borichansky and Mikhailov*, 1966). With friction, the mean centreline velocity of an ebb-jet decays exponentially, while the jet width grows exponentially with distance from the inlet. Flow measurements at the mouth of the Altamaha River Estuary, Georgia showed enhanced bottom friction owing to interactions of opposing waves with ebb flow (*Kang and Di Iorio*, 2005). However, the effect of a seaward sloping bottom on the outer edge of the ebb shoal can counteract the rapid jet expansion owing to friction because the jet width must adjust to maintain depth-averaged jet volume continuity as depth increases (*Özsoy*, 1977; *Kilcher and Nash*, 2010; *Kilcher et al.,* 2012). In contrast, stratification on the outer ebb shoal can reduce the effective jet depth and enhance spreading and dispersion (*Spydell et al.,* submitted 2014). Field observations in New Zealand suggest that much of the momentum of the ebb flow is contained within a vortex pair that forms along the sides of the ebb jet, transporting

momentum alongshore and offshore from the inlet, and dissipating energy slowly as it spins down (*Old and Vennell*, 2001; *Spiers et al.,* 2009).

Here, a simple model for an unstratified ebb-tide jet flowing into a directly opposing wave field (Figure 3.1) is used to investigate the interactions of waves with a current jet. This effort is motivated by the need for a simple 'exploratory-type' model (e.g *Murray and Theiler*, 2004) of the fundamental processes controlling ebb-jet strength and extent. The simplified approach complements more computationally expensive detailed numerical studies. There have been multiple efforts to model ebbing tidal flows using such simplified approaches (*French*, 1960; *Abramovich*, 1963; *Özsoy*, 1977; *Joshi and Taylor*, 1983; *Ismail and Wiegel*, 1983; *Ortega-Sanchez et al.*, 2008). By assuming a non-dimensionalized vertically- and laterally-averaged axis-symmetric jet an analytical solution to the quasi two-dimensional ('2D') turbulent jet equations can be derived from the standard shallow water equations with friction (*Özsoy and Ünlüata*, 1982). The symmetry allows the use of a self-similarity profile to model the

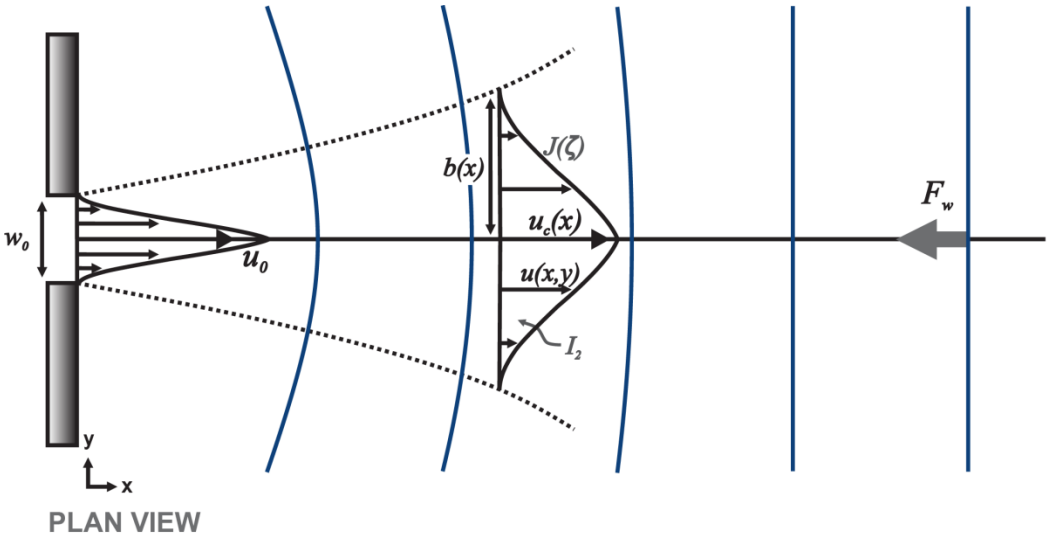

Figure 3.1. Schematic diagram of the idealized ebb-jet hydrodynamics represented by the simple model. For an inlet of width w_0 and velocity u_0, the ebb-jet is described by the half width $b(x)$ and centerline velocity $u_c(x)$. Jet velocity away from the centerline, $u(x,y)$ is assumed to decay with distance from the centerline with the similarity profile $J(\zeta)$ [Eq. (4)]. Blue curves are wave crests, with momentum flux given by the Fw [Eq. (2)]. See text for details.

centreline stream-wise velocity and jet width with distance from the inlet. The model (*Özsoy and Ünlüata*, 1982) did not include waves, but allowed for flat, constant sloping, or arbitrary depth profiles, and could be used to drive sediment transport. Simplified depth-averaged mass and momentum equations derived from the equations of motion were used to obtain a theoretical expression that compares well with laboratory observations of the change in the spreading rate of a jet in the presence of opposing waves (*Ismail and Wiegel*, 1983). The modelled and observed wave-induced spreading of a turbulent jet increased linearly as the ratio of the wave momentum to the initial jet momentum (i.e., the rate of spreading increased with wave height and decreasing wave period). The results suggested that wave momentum flux is the dominant force increasing the jet spreading rate. However, the investigation was limited to jets with turbulent fluctuations that were small relative to the wave velocity fluctuations on flat bathymetry with negligible friction. The model presented here builds upon this earlier work (*Özsoy and Ünlüata,* 1982; *Ismail and Wiegel,* 1983) by balancing wave momentum flux, modelled using radiation stresses caused by waves shoaling and breaking, with wave-induced bed shear-stress and turbulence. The contributions by a pressure gradient in balancing radiation stress are not included in the model. The model is verified with field observations collected using an array of wave and current sensors at New River Inlet, North Carolina (*Wargula et al.*, 2014; *Chen et al.*, 2015).

The simple model simulates some of the behaviours found in detailed numerical studies, such as the increase in lateral jet spreading through conversion of wave momentum flux and enhanced bottom friction (*Nardin et al.*, 2013), as well as the dependence of wave-current interactions on jet outflow rate, offshore wave energy, and inlet morphology, with morphology being the dominant controlling variable (*Olabarrieta et al*., 2014). However, the model does not simulate wave refraction and the detailed processes of breaking caused by ebb currents (as in *Olabarrieta et al*., 2014) nor does it simulate the morphological influence on jet extent and spreading through

the development of a pressure gradient (as in *Edmonds and Slingerland*, 2007).

3.2 **Methods**

The idealized, semi-analytical model solves the momentum balance along the ebb-jet centreline between an ebbing tidal jet at an inlet and an opposing wave field (Figure 3.1). The model domain consists of a tidal inlet and an alongshore-uniform receiving body of water of arbitrary depth. The inlet width is initialized at the landward boundary and used as part of a normalizing length scale.

3.2.1 Hydrodynamics

The slowly evolving hydrodynamic flow is based on the depth-averaged shallow water momentum and mass continuity equations averaged over turbulent and wave timescales. Coriolis force can cause veering in jet flows depending on the Rossby radius of deformation (e.g. *Pedlosky*, 1987); however on the length and velocity scales used here the effect is negligible and therefore neglected. Also considered higher-order, horizontal pressure and water level variations are neglected. Using these assumptions, the shallow water momentum and mass continuity equations are (*Saint-Venant*, 1871)

$$\begin{aligned}
&\frac{\partial(hu)}{\partial t}+\frac{\partial(hu^2)}{\partial x}+\frac{\partial(huv)}{\partial y}=\frac{1}{\rho}\left(-\bar{\tau}_{b,x}+\bar{F}_{t,x}+\bar{F}_{w,x}\right),\\
&\frac{\partial(hv)}{\partial t}+\frac{\partial(huv)}{\partial x}+\frac{\partial(hv^2)}{\partial y}=\frac{1}{\rho}\left(-\bar{\tau}_{b,y}+\bar{F}_{t,y}+\bar{F}_{w,y}\right),\\
&\frac{\partial(hu)}{\partial x}+\frac{\partial(hv)}{\partial y}=0,
\end{aligned} \tag{3.1}$$

where h is the height of the water column, u and v are the x- (cross-shore, positive offshore) and y- (alongshore) components of vertically averaged velocity, g is gravitational acceleration, and ρ is water density. The overbar ($\bar{\cdot}$) indicates vertical-averaging. The bed shear-stresses in the x and y directions are $\bar{\tau}_{b,x}=\rho c_f\sqrt{u^2+v^2}u$ and $\bar{\tau}_{b,y}=\rho c_f\sqrt{u^2+v^2}v$, the momentum losses due to turbulence mixing are $\bar{F}_{t,x}=\rho c_t\sqrt{u^2+v^2}u$ and $\bar{F}_{t,y}=\rho c_t\sqrt{u^2+v^2}v$, and the forces (in units of shear stress) induced by wave breaking are

$$\bar{F}_{w,x} = -\frac{\partial S_{xx}}{\partial x} - \frac{\partial S_{yx}}{\partial y},$$
$$\bar{F}_{w,y} = -\frac{\partial S_{xy}}{\partial x} - \frac{\partial S_{yy}}{\partial y}, \quad (3.2)$$

where the wave radiation stresses are approximated by (*Longuet-Higgins and Stewart*, 1964)

$$S_{xx} = E\left(\frac{c_g}{c}\cos^2\theta + \frac{c_g}{c} - \frac{1}{2}\right),$$
$$S_{xy} = S_{yx} = E\left(\frac{c_g}{c}\sin\theta\cos\theta\right), \quad (3.3)$$
$$S_{yy} = E\left(\frac{c_g}{c}\sin^2\theta + \frac{c_g}{c} - \frac{1}{2}\right),$$

in which θ is the angle of wave propagation with respect to current flow, and c_g and c are the wave group velocity and celerity, respectively, estimated from the peak wave period T_p and the water depth h. For waves opposing the current, as assumed here, $\theta = 180°$ and $S_{xy} = S_{yx} = 0$, and for alongshore homogeneous bathymetry $\frac{\partial S_{yy}}{\partial y} = 0$.

Cross-shore velocity profiles are assumed self-similar and symmetric across the jet, allowing the vertically-averaged equations (3.1) to be laterally-averaged using a self-similarity function (*Abramovich*, 1963; *Schlichting*, 1968; *Özsoy*, 1977). The jet is assumed to have a similarity profile shape (Figure 3.1) given by (*Stolzenbach and Harleman*, 1971; *Özsoy* and *Ünlüata,* 1982; *Nardin et al.,* 2013)

$$J(\zeta) = \begin{cases} 0 & ; \quad 1 < \zeta \\ (1-\zeta^{1.5})^2 & ; \ 0 < \zeta < 1, \\ 1 & ; \quad \zeta < 0 \end{cases} \quad (3.4)$$

where b is the jet half-width, and ζ is distance in the cross-jet dimension normalized by the jet half-width (i.e., $\zeta = \frac{|y|}{b}$).

Traditionally, the analytical solution of jets is separated into different zones based on the amount of influence of lateral advection on the initial jet core (e.g. *Özsoy* and *Ünlüata*, 1982; *Joshi*, 1982). The Zone of Flow Establishment ('ZOFE') includes a jet core (or region with cross-jet constant initial velocity) and covers the region where the jet begins at the

inlet, seaward to the point where the width of the jet core decays to zero. The centreline velocity is unaffected by lateral advection throughout the ZOFE. The Zone of Established Flow ('ZOEF') occurs seaward of the ZOFE and lacks a jet core. The cross-jet velocity profile in the ZOEF is defined with the self-similarity function (equation 3.4) beginning at the inlet. Some argue that there is even a transitional zone between the ZOFE and ZOEF as the transition should require a certain length to adjust between solutions depending on friction (*Ortega-Sanchez et al.*, 2008).

Here, we consider the ebb-jet to already satisfy the requirements of the ZOEF directly at the inlet. This assumption simplifies the model formulation and is supported by depth-averaged cross-jet current profiles measured at Raglan, New Zealand (see Appendix C, Figure C.5d) that show gradual decay at the channel margins of the inlet.

Applying the similarity assumption, the momentum and continuity equations take a 2D [offshore distance x, and jet-width $b(x)$] form (equation 3.5) following modifications of the classic jet equations (*Özsoy* and *Ünlüata*, 1982). The vertically- and laterally-averaged jet x-momentum and jet mass continuity equations inside the jet are therefore

$$\begin{aligned} &I_1 h\frac{\partial(bu_c)}{\partial t} + I_2\frac{\partial(hbu_c^2)}{\partial x} = \frac{I_2 b}{\rho}\,\tau_{b,x} + \frac{I_2 b}{\rho}\,F_{\mathrm{t},\,x} + \frac{b}{\rho}\,F_{\mathrm{w},\,x}, \\ &h\frac{\partial b}{\partial t} + I_1\frac{\partial(hbu_c)}{\partial x} - ahu_c\frac{\partial b}{\partial x} = 0. \end{aligned} \tag{3.5}$$

where I_1 and I_2 originate from lateral-averaging the self-similarity profiles within the ZOEF, and are given by

$$\begin{aligned} I_1 &= \int_0^1 (1-\zeta^{1.5})^2 d\zeta \;\approx 0.450, \\ I_2 &= \int_0^1 [(1-\zeta^{1.5})^2]^2 d\zeta \;\approx 0.316. \end{aligned} \tag{3.6}$$

The analogous laterally-averaged bed shear-stress term is $I_2 b\tau_{b,x}$, where $\tau_{b,x}$ and turbulent mixing terms ($F_{\mathrm{t},\,x} = -\rho c_t u_c|u_c|$) use simple drag-like coefficients dependent upon the centreline velocity to dissipate momentum. The c_t and c_f parameters are specified during model calibration. For simplicity, wave group and phase velocity, and wave height and

propagation direction are assumed to be uniform across the jet, i.e., no wave refraction. This assumption leads to the laterally averaged wave forces $bF_{\mathrm{w},\,x} = -b\partial\left(E\left(2c_g/c - 1/2\right)\right)/\partial x$ when waves are directly opposing the current ($\theta = 180°$). The velocity of inflow across the jet boundary is represented by the coefficient of entrainment, $a = 0.03$ (*French*, 1960). Wave energy, $E = \frac{1}{8}\rho g H_{rms}^2$ where H_{rms} is the root-mean squared wave height. The near-bed wave orbital velocity is calculated as $u_{orb} = \omega H_{rms}(2\sinh(kh))^{-1}$ (*Soulsby*, 1987).

The friction factor c_f is a scalar value applied uniformly throughout the domain. The weak flow approximation (*Liu and Dalrymple,* 1978) is used when waves are present, but without waves, $u_{orb} \to 0$ so the following approximation is used,

$$\tau_{b,x} = \begin{cases} -\rho c_f u_c u_{\mathrm{orb}} & \text{with waves,} \\ -\rho c_f u_c |u_c| & \text{without waves.} \end{cases} \tag{3.7}$$

Seaward of the terminal end of the ebb-jet [defined here as the first (offshore from the inlet) zero-crossing (from offshore to onshore flow) in current velocity], the flow is composed purely of a vertically averaged wave-generated current along the x-axis. As such, the jet equations (3.5) are no longer valid and a depth-averaged 1D x-momentum equation is used, which combined with the 1-D mass continuity condition describes the flow in the region beyond the seaward extent of the ebb-jet as

$$h\frac{\partial u_c}{\partial t} + hu_c\frac{\partial u_c}{\partial x} = -c_f u_c|u_{\mathrm{orb}}| - c_t u_c|u_c| - \frac{1}{\rho}\frac{\partial}{\partial x}\left[E\left(\frac{2c_g}{c} - \frac{1}{2}\right)\right]. \tag{3.8}$$

3.2.2 Waves

Waves and currents interact in the ebb-jet (*Olabarrieta et al*., 2011, 2014; Dodet et al., 2013) and wave orbital velocities increase bed shear-stress (*Nardin et al.*, 2013; *Soulsby and Clarke*, 2005). The intrinsic frequency of the wave oscillations varies with current and depth as described by the dispersion relation. The excess momentum flux that modifies the current as waves shoal and break is determined by the gradient of the radiation stress (*Longuet-Higgins and Stewart*, 1964).

In the model, the wave field is determined by locally applying the linear dispersion relation with a (Doppler) shift for an opposing current, $\sigma^2 = (\omega - k \cdot u_c)^2 = gk \tanh kh$ (*Phillips*, 1977), where $\omega = 2\pi f$ is the observed (absolute) angular frequency and k is the wave number. The wavenumber and intrinsic angular frequency σ are locally applied along the profile. The dispersion relation is used to calculate the wave group and phase.

Wave breaking is more strongly influenced by morphology than by an ebb-jet at a shallow (relative to wave height) ebb-tidal delta, as observed at Willapa Bay, Washington (*Olabarrieta et al.*, 2011), at New River Inlet (*Chen et al.,* 2015) and in numerical model results of idealized ebb-tidal deltas (e.g. *Olabarrieta et al.*, 2014). In all three cases, wave-height modulation was mainly caused by changes in depth rather than wave-current interaction. This suggests that wave energy dissipation at an ebb-tidal delta might not be too different than at a beach. Therefore, we adopt a wave height transformation formulation for wave-energy dissipation initially derived for depth-limited breaking at a beach (*Thornton and Guza*, 1983) to model the spatial change in energy flux (e.g., wave energy dissipation) over an ebb-shoal with opposing current. The original formulation is extended to include the effect of an opposing current on the wave frequency, given by

$$\frac{\partial E c_g}{\partial x} = \varepsilon_b = \frac{3\sqrt{\pi}}{16} \rho g B^3 \sigma \frac{H_{rms}^5}{\gamma^2 h^3} \left\{ 1 - \left[1 + \left(\frac{H_{rms}}{\gamma h} \right)^2 \right]^{-\frac{5}{2}} \right\}, \qquad (3.9)$$

where E is energy, B is a breaker coefficient that represents the fraction of foam region on the face of a breaking wave, and the breaker index $\gamma = H_b/h_b$ is an adjustable coefficient relating the height of waves at breaking, H_b to the water depth at breaking, h_b. Wave height along the profile is given by the solution to equation (3.9).

3.2.3 Numerical Solution

The model domain is defined by a depth profile and the inlet width. Boundary conditions include the current speed at the inlet u_0, and the offshore wave height H_{rms} and period T_p. Initial conditions include initial

velocity $u_0(x)$ and jet width $b_0(x)$ profiles. Although gradients in radiation stress from waves breaking on the ebb shoal have been predicted and observed to force water into inlets (*Malhadas et al.,* 2009; *Bertin et al.*, 2009; *Wargula et al.*, 2014; *Orescanin et al.*, 2014), potentially raising water levels inside the bay (*Olabarrieta et al.*, 2011; *Dodet et al.,* 2013), these effects are not included in the model. To minimize instabilities, the initial velocity profile should smoothly connect the inlet velocity condition and the offshore velocity condition [typically $u_0(x_{end}) = 0$]. The initial jet width profile can come from field measurements or can be set to any non-zero value.

Ebb-tide deltas often have well-pronounced main channels that restrict the spreading of ebb jets. Initial model runs did not reproduce the increase in velocity observed where shoals constricted the jet to flow within a relatively narrow channel. To account for this channelization without violating the axial-symmetric self-similarity assumptions that allow for the lateral-averaging of the depth-averaged equations (3.1), a channelization parameter $ch \in [0,1]$ is used. This parameter limits the jet spreading in the presence of a channel by suppressing $\partial b/\partial t$ (equation 3.5) such that the jet half-width at the next iteration becomes

$$b_{new} = b_{old} + (1 - ch)\frac{\partial b}{\partial t}, \tag{3.10}$$

where the channelization parameter ch is specified during initialization of the model as the ratio of the depth of the channel boundary to the depth of the thalweg at each x. The channelization parameter introduces sensitivity in the model solutions to the level of channelization. In general, increasing the channelization decreases the lateral spreading of momentum and increases the seaward extent of the jet.

In all cases, the momentum and continuity equations (3.5 and 3.8) are solved simultaneously using explicit methods. The momentum equation is solved using a forward difference in time and a second-order forward difference in space. The mass continuity equation is solved forward in time, but with a second-order central difference in space. Time and space

discretizations must be small enough to satisfy standard Courant-Friedrichs-Lewy ('CFL') convergence conditions for the flow and wave propagation within the domain. Stable results were found using $dt = 0.01\ \mathrm{s/iteration}$ and $dx = 5$ m.

For any given depth profile, a velocity boundary condition is applied at the inlet, and wave conditions are prescribed at the seaward boundary. Speed of convergence in the model solution is improved by providing the equilibrium solution for the given depth profile for a jet without waves, but with friction and turbulence as the initial approximation for the jet velocity and width along the jet-axis.

Wave conditions, including the dispersion relation and energy dissipation, found using equation (3.9), are calculated using a shoreward-differencing scheme at each time step. To include wave-current interaction effects, the wave field is calculated for a given flow field and depth profile (with intrinsic frequency dependent on the flow speed) followed by a recalculation of the flow field (from 3.5 and 3.8) using the updated wave conditions at each time step. This coupling is performed once per time step.

3.3 **Results**

For a given depth profile, the model describes the depth-averaged mean-current resulting from the interaction of an ebb-jet with an opposing wave field. Here, the model is compared with other numerical and theoretical models, with laboratory experiments, and with field observations.

3.3.1 Qualitative Jet Behaviour

An ebb-jet has an initial seaward directed flux of momentum extending from the inlet. In the absence of waves, the current associated with that momentum decays exponentially along the centreline with distance from the inlet due to friction, turbulence, and lateral loss of mass from spreading (Figure 3.2a). The lateral loss of mass is counteracted somewhat by entrainment, which is governed by the term a in equation (3.5). Typically, the jet width increases with distance from the inlet. However, when the

entrainment is insufficient to compensate for the increase in jet cross-sectional area owing to an increase in depth, the jet contracts to maintain depth-averaged continuity [e.g., the jet width contracts seaward of the shoal ($x = 1\,\mathrm{km}$) in Figure 3.2a1].

An opposing wave field increases the decay of the jet velocity and the lateral spreading of the ebb-jet, and shortens the seaward extent of the jet momentum (Figure 3.2b and c). Opposing unbroken waves increase the expansion of an ebb-jet by enhancing bed friction (*Nardin and Fagherazzi* 2012; *Nardin et al.*, 2013). Also, excess momentum caused by the shoaling and breaking of waves alters the momentum of the ebb-jet (*Longuet-Higgins and Stewart*, 1964). As waves shoal, the momentum flux acts in the seaward direction, whereas as waves break, the momentum flux acts in the shoreward direction, counteracting the jet. Thus, the jet spreads laterally where the currents converge. As the wave height increases the seaward extent of the jet (indicated by the first positive-to-negative u_c zero-crossing) decreases (e.g., *x* = 0.80 km in Figure 3.2b2 and *x* = 0.74 km in Figure 3.2c2), and the jet widens. Similar to numerical model results (*Olabarrietta et al.*, 2014), a convergence point in the

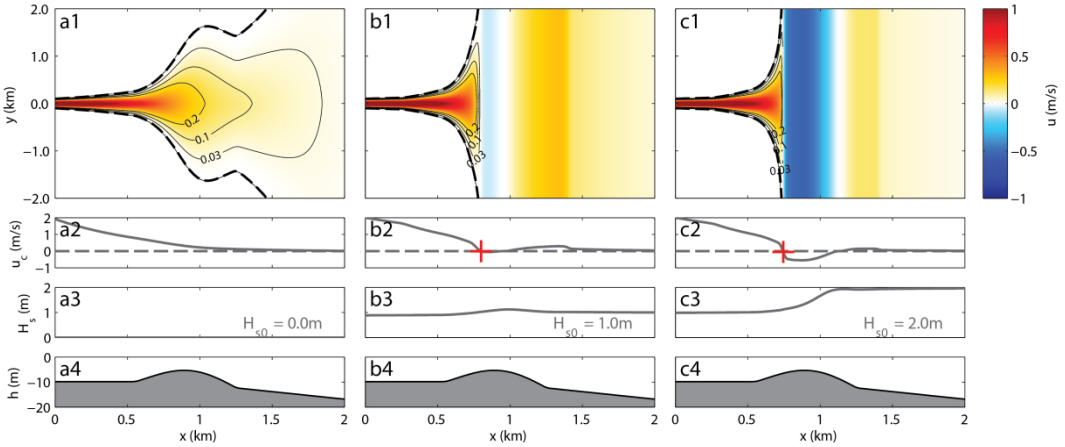

Figure 3.2. Model output showing simple jet flow a) without waves, b) with an opposing wave field with significant wave height of 1 m, and c) with an opposing wave field with significant wave height of 2 m. From top to bottom are (a1, b1, c1) contours of velocity (scale on the right) as a function of alongshore (*y*) and cross-shore (*x*) position, and (a2, b2, c2) velocity, (a3, b3, c3) wave height, and depth (a4, b4, c4) versus cross-shore position along the centre of the channel (*y* = 0). The point of flow convergence is shown (red + symbol in b2 and c2). Note that seaward of the jet, the solution along the centreline (*y* = 0) is extended uniformly alongshore to the edges of the domain (*y* = +/- 2 km).

centreline velocity occurs where the wave-driven shoreward current meets the seaward current of the ebb-jet (Figure 3.2b and c).

3.3.2 Comparison with Laboratory Experiments and Numerical Models

Laboratory measurements in the absence of waves (*Ismail and Wiegel*, 1983) are used to test the simple model on a flat bathymetry ($h = 0.114$ m). Model details are listed in Table 3.1. The modelled current profiles are similar to the laboratory observations in the ZOEF (Figure 3.3, compare solid blue curves with symbols) using $c_f = 0.00039$ and $c_t = 0.00001$. The flume in *Ismail and Wiegel's* had a smooth concrete floor, which had a Manning's $n \approx 0.012$ with water depth $h = 0.11$ m, corresponding to $c_f = 0.004$, which is one order of magnitude larger than the value used in the model (Table 3.1).

The analytical solution (*Özsoy and Ünlüata*, 1982) was modified (*Nardin et al*., 2013) to include frictional effects of non-breaking waves and was compared with the numerical model Delft3d FLOW-WAVE to simulate a constant barotropic (river) jet flowing into an opposing (non-breaking) wave field on flat bathymetry. The same boundary conditions (*Nardin et al*., 2013) are used as input for simulations with the simple model on flat bathymetry. Model boundary conditions and parameter settings are listed in Table 3.1. Model current profiles match closely those from Delft3d

Table 3.1. Model scenarios and settings used for comparison with results from *Ismail and Wiegel* (1983), *Nardin et al.*, (2013), and New River Inlet (NRI) (*Wargula et al.,* 2014). For the NRI data the mean values (over 9 events) are listed, with standard deviations in parentheses.

Conditions:	Depth (m)	w_0 (m)	u_0 (ms^{-1})	H_s (m)	T_p (s)	c_f	c_t	B	γ
I&W83 01	0.114 (flat)	0.038	0.10	0	n/a	3.9E-4	1E-5	n/a	n/a
I&W83 02	0.114 (flat)	0.038	0.14	0	n/a	3.9E-4	1E-5	n/a	n/a
I&W83 03	0.114 (flat)	0.038	0.16	0	n/a	3.9E-4	1E-5	n/a	n/a
Nardin 01	3 (flat)	65	1.4	0	n/a	0.0248	0.001	1	0.2
Nardin 02	3 (flat)	65	1.4	0.3	10	0.0248	0.001	1	0.2
Nardin 03	3 (flat)	65	1.4	0.5	10	0.0248	0.001	1	0.2
NRI	Thalweg Profile	135	Sensor 04	Sensor 09	Sensor 09	0.0124 (0.0099)	0.0035 (0.0011)	1	Event-specific

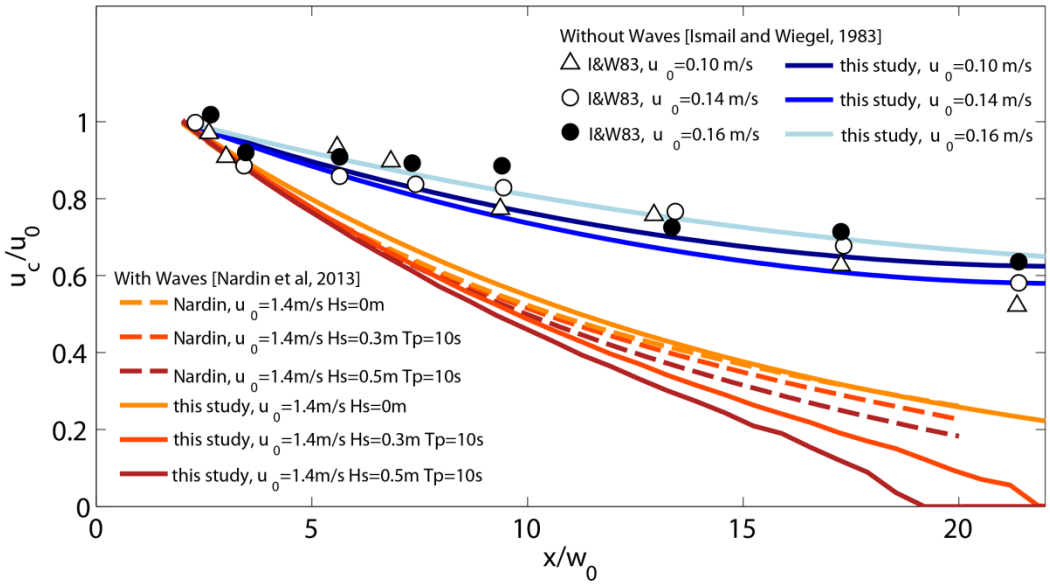

Figure 3.3. Centreline velocity (normalized by the exit velocity at the inlet mouth) versus distance from the inlet mouth (normalized by the inlet width). Symbols (see legend in upper right) are laboratory results (redrafted from *Ismail and Wiegel*, 1983) for turbulent jets (no opposing wave field), dashed orange-red curves (see legend in lower left) are numerical simulations (redrafted from *Nardin*, 2013), and solid orange red and blue curves (both legends) are model results (equation 3.5).

(*Nardin et al.*, 2013) in the ZOEF with non-breaking waves (Figure 3.3, compare solid with dashed orange-red curves). The results show that including wave-breaking-induced shoreward momentum flux (this study) causes the jet current to stop and a convergence point to develop (Figure 3.3, solid red-orange curves for $H_s > 0$, where H_s is the significant wave height, 4 times the standard deviation of sea-surface elevation fluctuations), whereas when the waves are included only through the bed friction term (*Nardin et al.*, 2013), the current slows, but is not blocked completely (Figure 3.3, dashed red-orange curves for $H_s > 0$). *Nardin et al.* (2013) used Chezy's $C = 65\ \mathrm{m}^{1/2}\ \mathrm{s}^{-1}$, corresponding to a friction factor of $c_f = 0.0023$ which was one order of magnitude larger than the value used in the jet model ($c_f = 0.0248$, Table 3.1).

3.3.3 Comparison with Field Observations of Tidal Jet

Model simulations were compared with field observations collected at New River Inlet, NC ('NRI') (*Wargula et al.*, 2014). Four acoustic Doppler current profilers (ADCPs) were deployed with pressure sensors mounted near the seafloor in the main channel of an ebb-tidal delta, and one sensor

pair was deployed in about $9\ \mathrm{m}$ depth offshore of the delta (Figure 3.4). Two additional pressure sensors without ADCPs (sensors 07 and 68 in Figure 3.4) also were mounted near the seafloor in the main channel near the ebb shoal. The ADCPs reported 1-min mean currents, and the pressure gauges were sampled at $2\ \mathrm{Hz}$. The current profiler data were depth averaged. To remove turbulent fluctuations in the 1-minute ADCP measurements, 15-minute averages were used. Sixty-one thirty-minute-long ebb-flow events, occurring at low tide, were selected for analysis. For these sixty-one ebb events, in $9\ \mathrm{m}$ depth (sensor 09, Figure 3.4) the significant wave height (in the frequency range from 0.05 to $0.30\ \mathrm{Hz}$) ranged from 0.4 to $1.4\ \mathrm{m}$, wave periods ranged from 3 to 10 seconds, wave angles (relative to the ebb jet near sensor 08) ranged from $-86°$ (from the south) to $26°$ (from the north), and the tidal ranges (difference between high and low tide) in the inlet (black + symbol near sensor 04, Figure 3.4) were from 0.57 to $1.41\ \mathrm{m}$. Water levels at low tide during the events, corrected for atmospheric pressure fluctuations, ranged from -0.62 to $-0.25\ \mathrm{m}$ below mean sea level (msl) during the ebb events. The ebb-jet flow ranged from 0.65 to $1.20\ \mathrm{m\ s^{-1}}$ at sensor 04.

The ebb-jet width was not measured, and therefore is not considered here. Knowledge of the jet width would allow for better determination of the level of entrainment and channelization. However, wave energy flux (proportional to wave height squared) during ebb events decreased onshore across the ebb shoal (Figure 3.5a), consistent with dissipation of wave energy from depth-limited breaking. The along-channel flow velocity initially decayed with distance offshore from the inlet mouth (sensor 04, Figure 3.4), but increased at the constriction in the main channel near sensor 06 (Figure 3.4) before decaying further (Figure 3.5b). During many events, the current slowed sharply over the ebb shoal at sensor 08 (Figure 3.5b) and occasionally reversed flow direction (shoreward). Offshore wave energy flux is negatively correlated with ebb-flow velocity at the inlet mouth (sensor 04) (the vertical order of red to blue curves in Figure 3.5a is reversed relative to the order in Figure 3.5b), indicating the penetration of wave-current interaction effects throughout the ebb-jet, consistent with

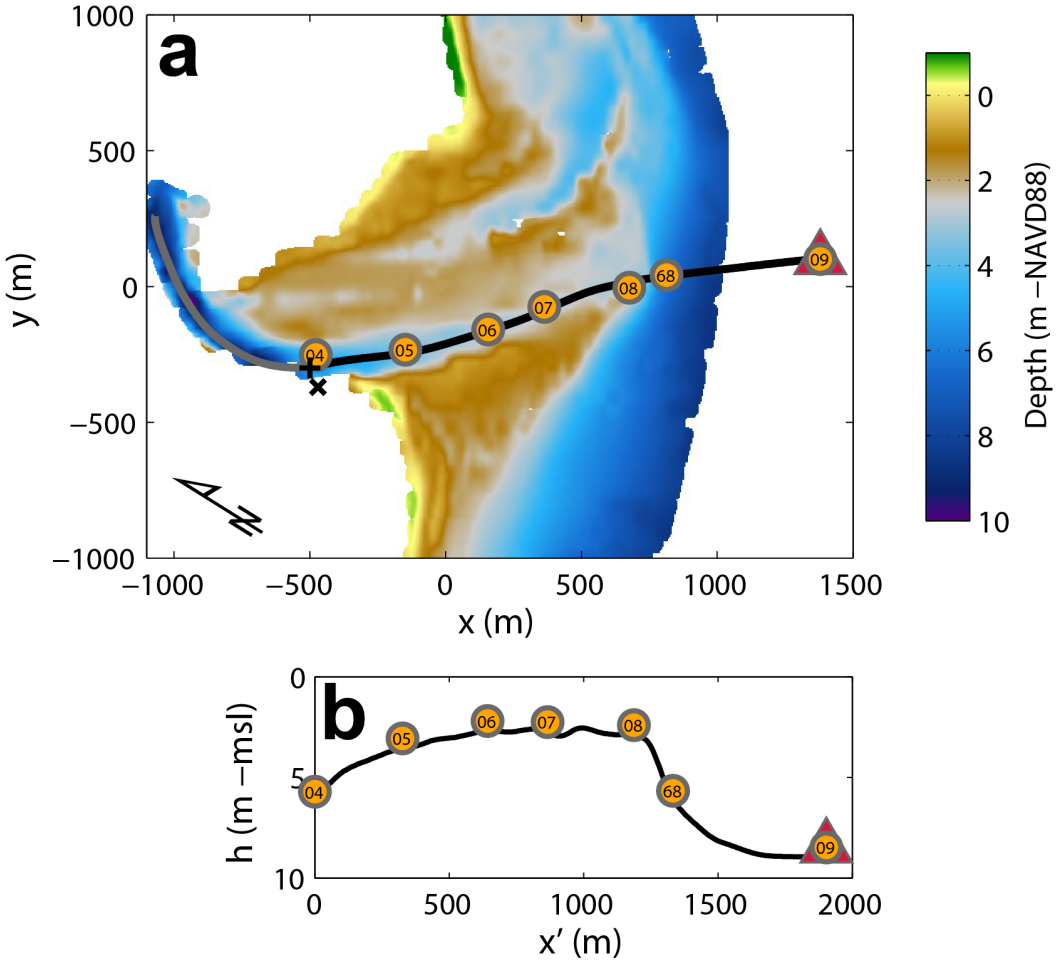

Figure 3.4. (a) Site map of New River Inlet, NC including bathymetry (color contours, scale on the right), thalweg position of main ebb channel (gray curve), current and pressure sensor locations (numbered), tide gauge (black + symbol), met station (black x symbol), and wave gauge (red triangle). The black curve indicates the extent of the region used to define the model domain with the 'inlet' beginning at sensor 04. The grid is oriented 58˚ from North. (b) The straightened thalweg depth profile with distance (x') from sensor 04 used as the model domain, and sensor locations (numbered).

previous results (*Wargula et al.,* 2014). During small wave events, the ebb-flow velocity was stronger along the entire jet profile and decayed less over the ebb shoal (blue curves, Figure 3.5b) than during large wave events (red curves, Figure 3.5b). For small wave events, shoaling occurred within the main channel at sensors 06 or 07 (blue curves, Figure 3.5a), possibly owing to the stronger flows. Flows at sensors 04, 05, 06, and 08 were aligned with the main channel thalweg. However, at sensor 09 cross- and alongshore currents often were similar (but small).

Differences between cross-shore velocity profiles from each ebb event and the mean profile (grey curve, Figure 3.5b), each normalized by the

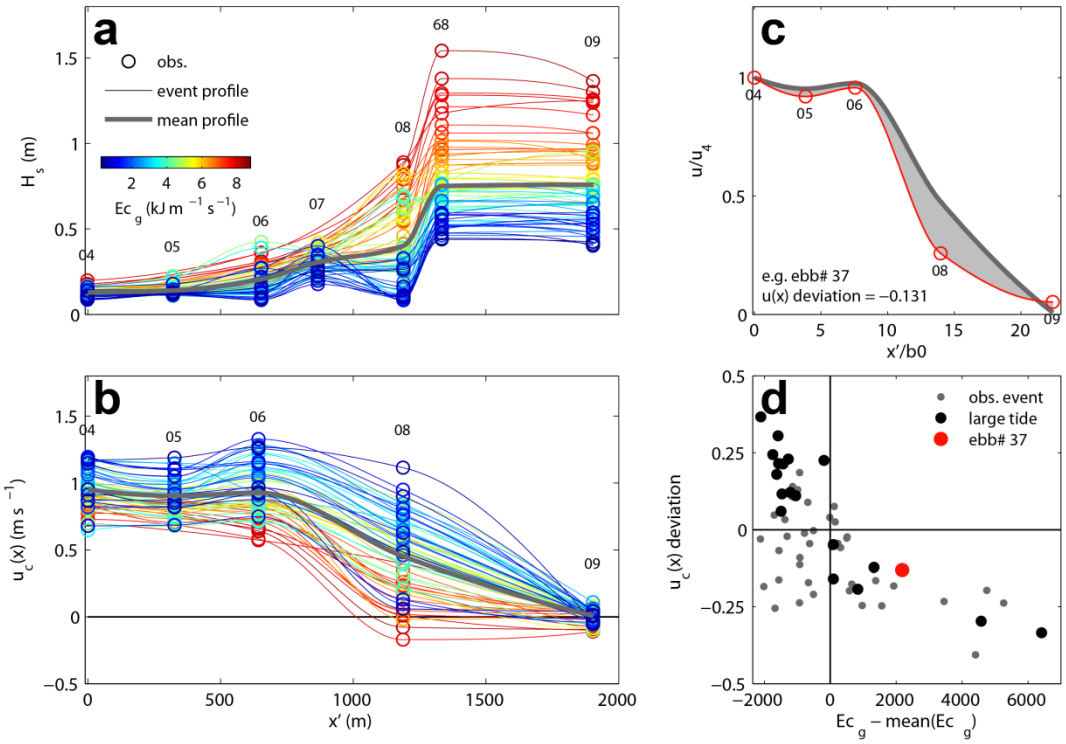

Figure 3.5. Characteristics of the sixty-one observed ebb-jets. (a) Significant wave height (coloured curves) versus distance from the inlet. The thick grey curve is the mean profile. Observations are marked by coloured rings (sensor numbers are listed above each cloud of rings). Colours correspond to offshore wave energy flux observed at sensor 09. (b) Ebb-jet velocity (coloured curves) versus distance from the inlet. The thick grey curve is the mean profile. Observations are marked by coloured rings (sensor numbers are listed above each cloud of rings). Colours correspond to wave energy flux at sensor 09. (c) Normalized ebb-jet velocity versus normalized distance from the inlet for an example showing how the deviation of a particular ebb event (ebb# 37) current profile (red curve) from the mean profile (grey curve) is calculated (see text for detail); and (d) average deviation of current profiles [the grey area in panel (c)] versus change in offshore wave energy during each event relative to the mean offshore wave energy over all events (ebb events following the largest change in water level between high and low tide (≥ 1.00 m) are shown in black, and the example event from panel (c) ebb# 37 is shown in red).

velocity at sensor 04, were calculated by integrating the areas between the curves (Figure 3.5c). These deviations were negatively correlated with offshore (9 m depth) wave energy flux Ec_g (Figure 3.5d), suggesting that waves slowed ebb currents within the main channel and over the ebb shoal. The correlation was highest for events during the largest tidal ranges (≥ 1 m), which were likely to have stronger ebb-jets (Figure 3.5d).

3.3.4 Calibration

Prior to calibrating the jet model, the best-fit γ value was determined for each of the sixty-one events to minimize potential errors from

misrepresentation of waves within the model domain. For each event, wave and current observations along the depth profile (adjusted for the tide) were used as input into the wave dissipation formulation (Equation 3.9). The coefficients B and γ are interrelated (*Roelvink,* 1993), and wave breaking intensity was held constant ($B \equiv 1$) and only γ was varied (*Cacina*, 1989; *Apotsos et al.,* 2008). The best-fit event-specific wave γ values were determined by minimizing the difference between observed and predicted wave heights at the 3 sensors (sensors 07, 08, and 68) shoreward of the offshore wave observations.

The best-fit γ values during opposing flows ranged from 0.14 to 0.53, with a mean value of 0.32, slightly smaller than typical γ values for similar wave conditions at other beaches (*Guza and Thornton*, 1980; *Thornton and Kim*, 1993; *Raubenheimer et al.*, 1996; *Lippmann et al.*, 1996; *Apotsos et al.*,

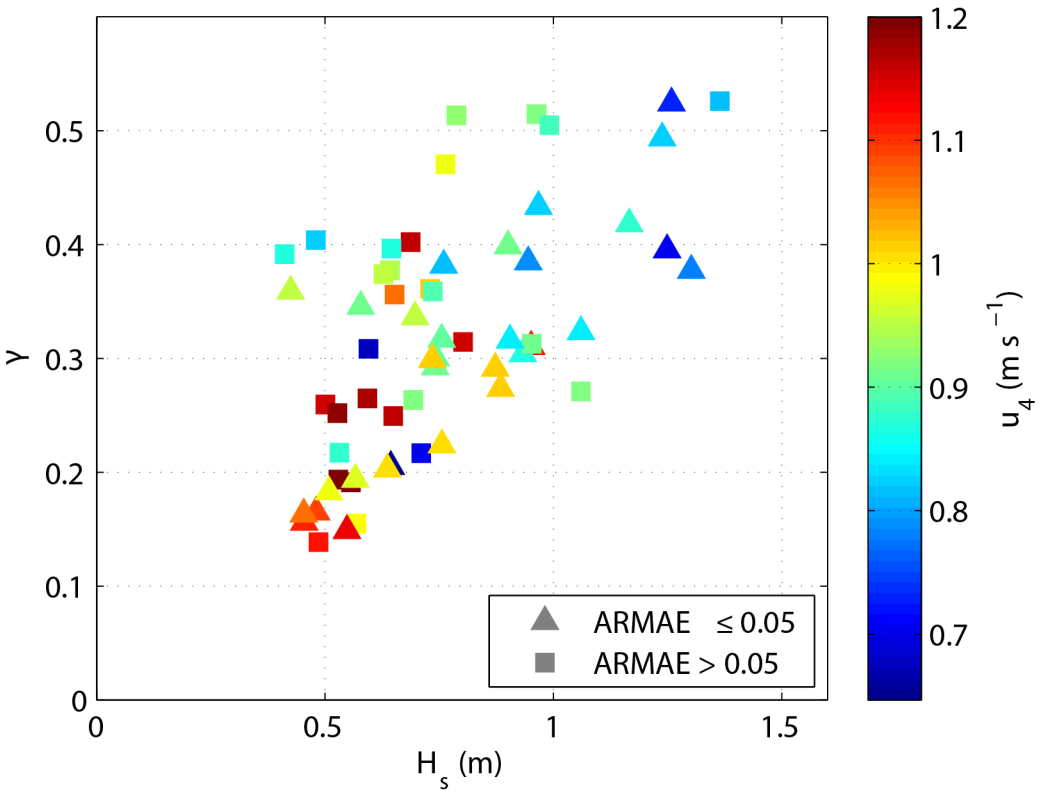

Figure 3.6. The best-fit γ versus significant wave height observed in 9 m water depth (sensor 09) for the wave height profile determined by equation 9 (*Thornton and Guza*, 1983) during each ebb event. Colour (scale on the right) indicates ebb current speed at sensor 04 during each event. Triangles indicate "excellent" (Table 3.2) fits and squares indicate less-than-excellent fits of the wave height profile over the full model domain. The breaking intensity was set to $B = 1$.

2008). The breaking indices γ are negatively correlated with inlet ebb-velocity at sensor 04 and positively correlated with offshore $(9\ \mathrm{m})$ wave height at sensor 09 (Figure 3.6).

To evaluate the goodness of fit between predictions and observations the Adjusted Relative Mean Absolute Error (ARMAE) was calculated for each run as (*Van Rijn et al.*, 2003; *Winter*, 2007)

$$\mathrm{ARMAE} = \frac{\frac{1}{N}\sum_{i=1}^{N}(|\mathrm{Pred}_i - \mathrm{Meas}_i| - \Delta\mathrm{Meas})}{\frac{1}{N}\sum_{i=1}^{N}|\mathrm{Meas}|}\ ,$$
$$\Delta\mathrm{Meas} = \begin{cases} 0.05\ \mathrm{m\ s^{-1}} & \text{for } u_c \\ 0.1\ \mathrm{m} & \text{for } H_s \end{cases}\ , \tag{3.11}$$

where Pred_i and Meas_i are predicted and measured values (either significant wave height or current velocities) at the i sensors. The term $(|\mathrm{Pred}_i - \mathrm{Meas}_i| - \Delta\mathrm{Meas})$ is set to zero if the absolute error is smaller than the accuracy of the measurements, $\Delta\mathrm{Meas}$, to ensure that the predicted values are within the error band of the measured values. Prediction qualifications based on ARMAE can range from "bad" to "excellent" (Table 3.2) (*Van Rijn et al.*, 2003).

The fit of modelled to observed wave heights was excellent ($H_s\ \mathrm{ARMAE} < 0.05$; Table 3.2) for events with offshore wave height $H_s \geq 0.7\ \mathrm{m}$, while the fit for events with offshore wave height $H_s < 0.7\ \mathrm{m}$ was good ($H_s\ 0.05 < \mathrm{ARMAE} < 0.10$; Table 3.2).

The ebb events were simulated with the jet model by adding the water level η (observed at the tide gauge (Figure 3.4a, black '+') uniformly to the depth profile (Figure 3.4b), and by applying the ebb velocity at sensor 04

Table 3.2. Qualification for error ranges in velocity, (*Van Rijn et al.*, 2003).

Qualification	Velocity ARMAE	Wave Height ARMAE
Excellent	< 0.1	< 0.05
Good	0.1-0.3	0.05-0.1
Fair	0.3-0.5	0.1-0.2
Poor	0.5-0.7	0.2-0.3
Bad	> 0.7	> 0.3

at the model inlet boundary and the offshore wave conditions at the offshore model boundary (at sensor 09) for each ebb event. The initial jet width was set to the measured channel width at sensor 04, $w_0 = 135\ \mathrm{m}$. All conditions were held constant for 30 minutes to allow the boundary conditions to propagate through the model domain.

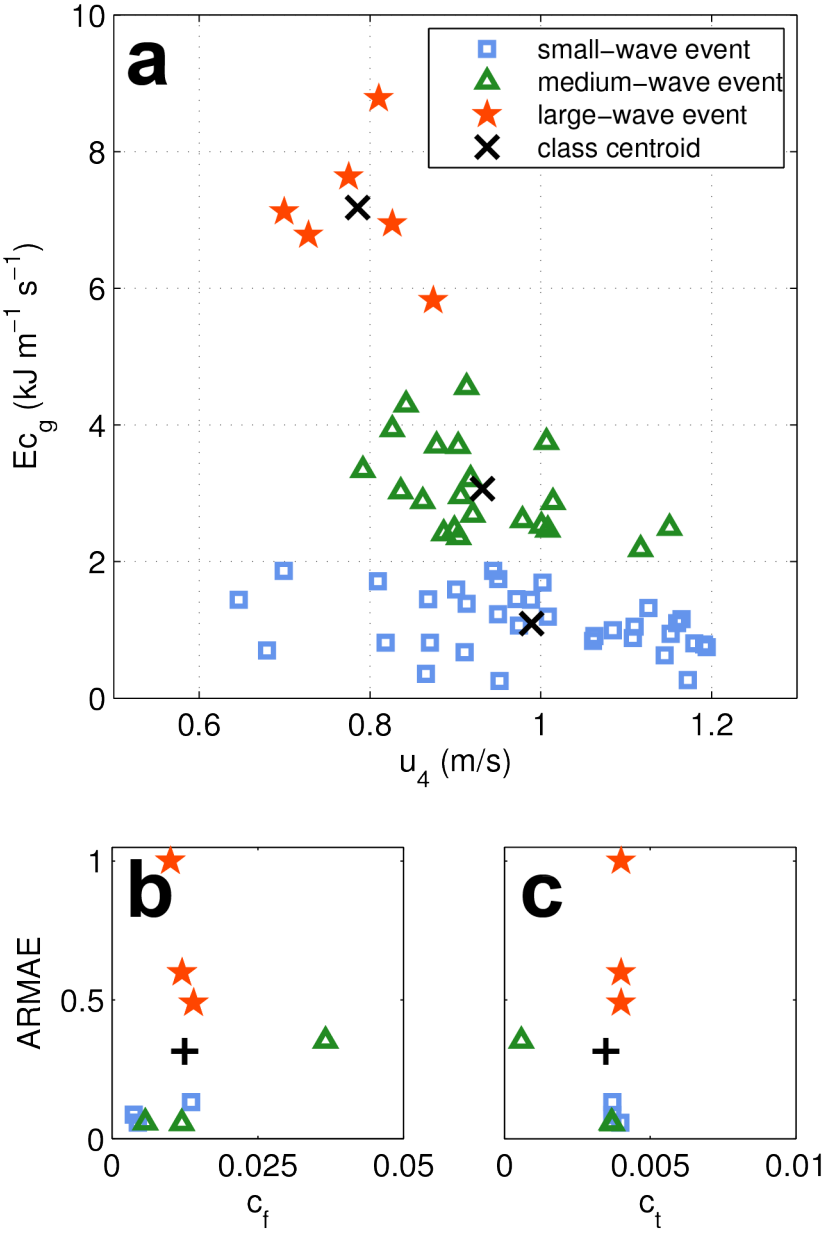

Figure 3.7. (a) Energy flux versus initial ebb velocity. The 61 ebb events were clustered into small (blue squares), medium (green triangles) and large (orange stars) offshore energy flux classes. Black x symbols indicate the centroid of each class. ARMAE of current throughout the domain versus mean values of (b) c_f and (c) c_t from the nine calibration runs (symbols). Black + symbols indicate the mean global parameters (with standard deviations) of $c_f = 0.0124$ (0.0099) and $c_t = 0.0035$ (0.0011).

The jet model was calibrated against nine ebb events [3 from each of 3 classes based on offshore energy flux (Figure 3.7a) spanning the range of conditions observed]. With the wave parameters previously determined ($B = 1$ and event-specific γ), only two free parameters remain within the jet model, the coefficient of friction c_f, and the turbulent mixing coefficient c_t. For each of the nine events, these parameters were optimized to reduce the mean absolute difference between observations and model predictions of current speed at the 4 ADCPs (sensors 05, 06, 08, and 09) seaward of the inlet. The values for the nine events (Figure 3.7b,c) had means (standard deviations) of $c_f = 0.0124$ (0.0099) and $c_t = 0.0035$ (0.0011). The friction factor $c_f = 0.0124$ is an order of magnitude higher than previous results from NRI (*Wargula et al.,* 2014) and is analogous to $C = 28.1\ \mathrm{m^{1/2}s^{-1}}$, where C is the Chézy coefficient. Unresolved processes are likely absorbed into the friction term, which explains the high friction factor values. This may restrict predictive capabilities of the model in cases where friction factors are based on bed roughness alone.

3.3.5 Validation

All sixty-one ebb events were simulated with the model using the best-fit mean values of the parameters c_f and c_t, along with $B = 1$ and each ebb-specific γ and tidal level. In all cases, the predicted ebb current profiles were qualitatively similar, with velocity decaying with distance offshore from the inlet. In most cases, the model reproduced the ebb-jet speed observed at sensors 05, 06, and 09 (Figure 3.8, Figure 3.9a,b,d). Predicted currents at sensor 08 often were smaller than observed (Figure 3.8, Figure 3.9c).

The skill of model flow predictions was assessed using $u_c\ \mathrm{ARMAE}$ values based on error ranges for velocity profiles (Table 3.2). Model predictions of the ebb-jet velocity were excellent at sensors 05 and 06 and bad farther offshore (sensors 08 and 09) (Figure 3.9). Although current predictions were within $0.25\ \mathrm{m\ s^{-1}}$ of observations at sensor 09, the $u_c\ \mathrm{ARMAE}$ qualification is based on relative error of observed velocities of $O(0.1\ \mathrm{m\ s^{-1}})$, and hence the apparently bad qualification.

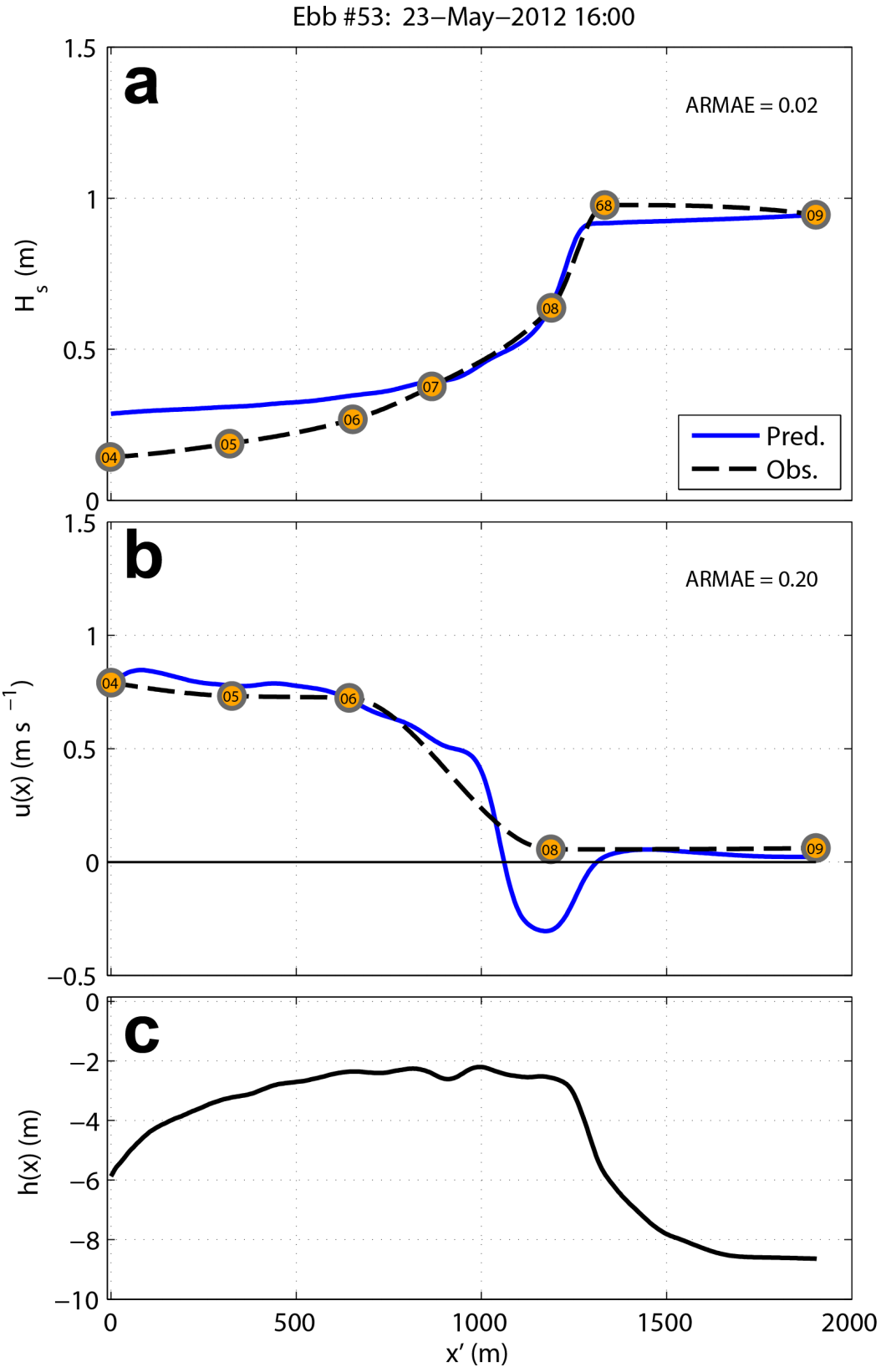

Figure 3.8. Observed (numbered sensors) and modelled (blue curves) (a) significant wave height and (b) jet-centreline velocity and (c) water depth versus distance from the inlet for ebb event 53.

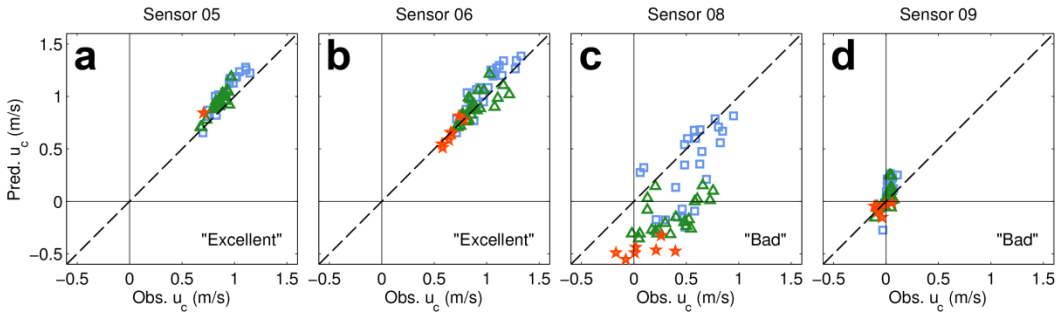

Figure 3.9. Modelled versus observed ebb-jet centreline current for sensors along the channel thalweg (sensor numbers on top of each panel, see Figure 3.4 for locations) for small (blue squares), medium (green triangles), or large (orange stars) offshore energy flux. Model skill (Table 3.2) is listed on each panel.

Modelled and observed ebb-jet currents were affected by opposing waves. At the shallow ebb shoal near sensor 08 wave dissipation slowed the ebb current, similar to previous results at this site (*Wargula et al.,* 2014) (Figure 3.9c, Figure 3.10). Waves above a certain energy threshold triggered a sharp decrease in ebb currents (Figure 3.10). The model often over-predicted the effect of depth-limited wave breaking on mean-flow dissipation at the ebb shoal, resulting in modelled currents smaller than observed (Figure 3.10), reducing model skill at these locations (Figure 3.9c). The model was better at predicting currents at the ebb shoal for small-wave events than for large-wave events (Figures 3.9c and 3.10).

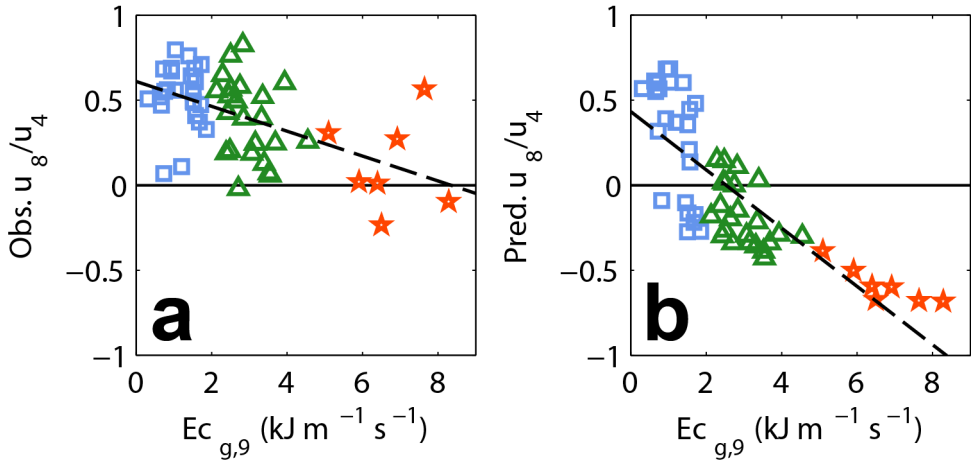

Figure 3.10. (a) Observed and (b) modelled ebb-jet velocity over the ebb shoal at sensor 08 normalized by the inlet velocity at sensor 04 vs offshore (9 m) wave energy flux for small (blue squares), medium (green triangles), and large (red stars) offshore energy flux. Least square linear fits are overlain (dashes) with slope (a) $0.07\ \mathrm{m\ s\ J^{-1}}$ and (b) $0.17\ \mathrm{m\ s\ J^{-1}}$.

3.4 Model Limitations

There was substantial variation in calibrated model parameters between the different ebb events (standard deviations for NRI parameters in Table 3.1). Although friction and turbulence factors were similar across event classes (Figure 3.7b,c), the ratio of wave height to depth at breaking, γ differed between ebb events (Figure 3.6). The breaker index γ increased with offshore energy flux (Figure 3.6) causing depth-limited wave breaking to initiate closer inshore than if the same conditions were used with smaller γ values.

The model has a fixed surface, and therefore lacks a pressure gradient term. When laterally unconstrained by levees, the spreading term acts like a pressure gradient term and many of the effects associated with pressure gradient enhance jet spreading. During calibration, underrepresented processes such as pressure gradients were effectively assimilated into the bed-shear stress and likely the reason for friction coefficient values in unnatural ranges, being an order of magnitude higher than measured. The high friction coefficients likely impacted the balance between ebb-currents and waves by acting preferentially on the mean-flow.

Wave-current interactions were only very roughly approximated in the model. The model calibration would benefit from the addition of certain processes to better represent these interactions. For instance, much of the turbulence associated with depth-limited breaking waves occurs near the surface boundary layer, affecting the vertical profile of dissipation and shear production, and therefore the ability of wave radiation stresses to transfer momentum to mean-flow (e.g. *Feddersen*, 2012). A parameterization of that process in the jet-model would allow for the retardation of the effects of waves on the mean-flow in shallow areas where wave breaking is likely to enhance the separation of surface and bottom boundary layers. Again, the inclusion of a pressure gradient term along with parameterized wave-generated water level set-up and set-down (e.g. *Bowen et al*., 1968) to the jet model would help to reduce lateral spreading of the ebb jet and reduce the reliance on the bed-shear stress to balance momentum.

The formula used in the model to calculate wave dissipation (*Thornton and Guza*, 1983) was derived for waves breaking on a beach, not for waves breaking on an ebb shoal with an opposing current. With appropriate data, an alternative probability density function could be used to fit the wave energy dissipation equation (3.9) to the wave breaking observations (*Thornton and Guza,* 1983). Given that ε_b is proportional to B^3 in equation (3.9), the assumption of optimal B has potential to significantly influence the magnitude of wave dissipation. The physical interpretation of $B = 1$ corresponds to fully developed bores, which is not the case for all waves in the observations, but is within the range of optimal B values (between 0.8 and 1.7) previously fit to beach data (*Thornton and Guza,* 1983). Values of $B > 1$ imply that wave dissipation is underestimated by the simple periodic bore dissipation function initially used to arrive at equation (3.9). Further, the breaker index γ assumes a saturated surf zone, which is not the case here. Recent analysis of drifter data at NRI suggests γ may be improved by including the effects of currents (*Zippel and Thomson*, 2014).

Over the offshore edge of the ebb shoal where depth increases seaward, the modelled current did not dissipate as much as observed (Figure 3.9d); possibly because the modelled bottom shear stress decreases too much with increasing water depth. The lack of frictional dissipation in deeper depths is compounded by the assumption of a linear turbulence term that must be low enough to allow the faster flows to decrease at reasonable rates within the observation array. With this turbulence formulation, offshore turbulent mixing is not sufficient to retard the offshore extent of a jet in deep water. The overall dissipation could be improved by including the effects of wave-induced turbulence on momentum exchange. Moreover, vortex shedding allows flow momentum to disperse away from the jet in deeper waters (*Spiers et al.*, 2009; *Olabarrieta et al.*, 2014). Thus, inclusion of vorticity generation and shedding may improve the model skill for offshore predictions. However, without more field measurements outside the main extent of the jet, it is not known if more advanced formulations are warranted.

Differences between actual (Figure 3.4a) and model (Figure 3.1 and Figure 3.4b) bathymetry may result in discrepancies between observed and modelled currents. The model assumes alongshore uniform bathymetry. As such, the jet spreads only through transfer of momentum to ambient surrounding water. At NRI, the ebb current is mostly confined to the channel. The channelization parameter (equation 3.10) used in the model is crude. In reality, the top layer of the flow should spread outward at a greater rate than the lower layer (which is more channelized), requiring a vertically resolved model. The orientation of the main ebb channel changes along its course (Figure 3.4a), possibly contributing curvature-related processes that are not included in the simplified model. Waves arriving at the ebb-tide delta may be refracted away from the channel by the complex bathymetry, but these effects are not included in the simplified model. Moreover, the bathymetry (Figure 3.4) includes a secondary channel that crosses the ebb shoal to the north of the main channel. The possible effects of the secondary channel are not included in the simplified model.

Offshore waves came from a wide range of directions, with incident angles from -86° to 26° (mean -17°) relative to the channel orientation at sensor 08, with the largest waves occurring at relatively small angles (Figure 3.11a). Within the model, waves are assumed to oppose the ebb-flow (i.e., direction = 180°), allowing neglect of the lateral radiation stress terms (e.g., S_{xy}) in equation (3.3), and resulting in an overestimation of wave forcing in equation (3.5). Although the best fits of wave height profiles are during events with small incident angles, there is no trend of model skill with wave angle (Figure 3.11b). Similarly, velocity model skill is not a strong function of wave angle, despite the model assumption of direction = 180° (Figure 3.11c).

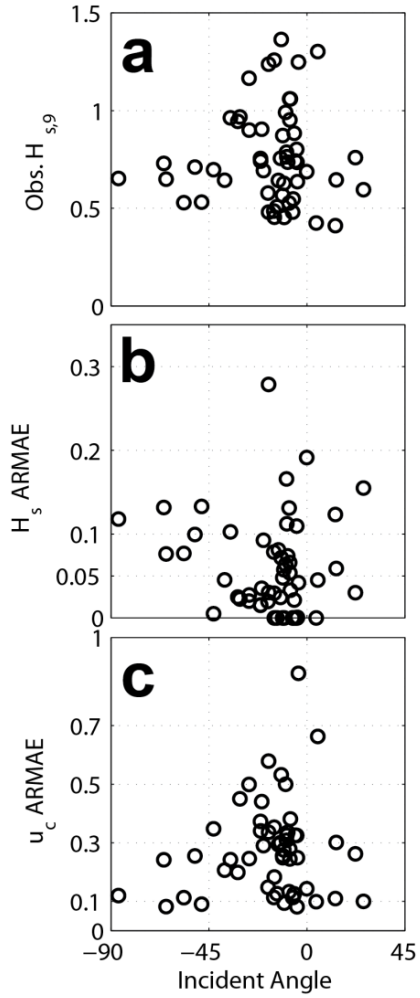

Figure 3.11. (a) Offshore (9 m) significant wave height and ARMAE across the model domain between modelled and observed (b) significant wave height and (c) ebb-jet current versus angle between waves and the jet centreline at the seaward edge of the ebb shoal. Negative values are waves from south of the jet centreline.

3.5 Conclusions

A simple, semi-analytical model based on the momentum and continuity equations, balancing inertia, bed friction, turbulent mixing, and simplified wave-current interaction simulates numerical, laboratory, and field observations of an ebb-jet flowing into an opposing wave field. The model extends previous results by including waves, describing the mean-flow of an ebb-jet, both without waves and with non-breaking or breaking waves. The model simulates the exponential decay of the centreline current and the exponential growth of the jet width, enhanced jet spreading with opposing waves, and a decreased ebb-jet extent with increased wave energy. Overall, the jet model predicted the field-measured currents with

excellent skill. The jet model skill was worst at the shallow region around the ebb-shoal where the model consistently over-predicted the influence of waves on slowing the jet current. Qualitatively, the predicted trend of increased wave-induced slowing and even the emergence of a flow convergence with increased wave energy flux matched measurements, but over predicted the effect.

Chapter 4

A Morphological Model to Simulate Ebb-Tidal Shoal Generation and Short-Term Response to Changes in Forcing Conditions

Turbulent, sediment- laden ebb-tidal flow in the main channel at Raglan, New Zealand. Photo courtesy Raphael Lumgrüber

Harrison, S.R., Bryan, K.R., and Mullarney, J.C. (submitted 2015). Morphodynamic sensitivity of ebb-tidal shoal development using a semi-analytical jet model. *Computers & Geosciences, Special Issue: Uncertainty and Sensitivity in Surface Dynamics.*

Contribution of Authors

Chapter 4 contains the material from an article entitled “Morphodynamic sensitivity of ebb-tidal shoal development using a semi-analytical jet model”, was submitted as a paper to a special issue of *Computers & Geosciences* focussed on “Uncertainty and Sensitivity in Surface Dynamics Modelling”. More work was included in this chapter than was included in the submitted article in order to present a fuller treatment. In chapter 4, the semi-analytical ebb-jet model (from Chapter 3) is coupled with sediment transport formulae to develop an exploratory morphodynamic evolution tool able to describe the development of ebb-shoal and channel morphology. In addition to development, the model is also used to describe short-term cross-shore response to changes in forcing conditions of sandbars on established ebb-shoals.

I implemented the model coupling and development, wrote all software and numerical code to process, analyse, visualize, and compare model output, and wrote the initial and subsequent drafts of the article. My co-authors, Karin R. Bryan and Julia C. Mullarney edited drafts and provided helpful direction.

Abstract

A morphodynamic model is developed and used to explore the sensitivity of ebb-tidal delta channel and ebb-shoal morphology to ebb-jet strength, waves, and sediment characteristics. Thirty-six model runs are used to identify the relative significance of parameters impacting the position of ebb-shoal bar crest, channel width, and the rate of morphological development. Currents above a threshold velocity increase the rate of bar growth —the effect of which is further enhanced by the addition of waves. Waves also lead to wider channels and shorter distances from inlet to ebb tidal shoal crest. Median grain size and grain material density of the seabed sediment played a slight role in controlling the bar crest position. All sediment characteristics influenced the rate of morphological development, from greatest to least being median grain size, grain material density, bed porosity, and grain size distribution. The parameterization of the effect of channelization on the jet outflow in the model enables the reduction of spatial dimensions, but is identified as a major source of uncertainty and raises questions about the natural mechanisms for lateral transfer of sediment between the ebb-shoal bar crest and channel margin linear bars (or levees). By making the assumption that cross-shore sediment fluxes alter the depth profile at a faster timescale than the alongshore changes to the levee positions, a static channel width enabled testing of sensitivities in the short-term response of the ebb-shoal depth profile in response to a variety of forcing conditions. The short-term response was sensitive to the assumed channel width, which alters the influence of wave and jet current conditions. Jet currents of $1.5\ \mathrm{m\ s^{-1}}$ or more were found to have a greater impact on the sandbar evolution than waves. Two types of sandbars were found based on the dominant source of forcing, with certain conditions leading to a double-barred ebb-shoal similar to previous observations at Raglan. The initial position of sandbars was shown to be less important to morphological development than the forcing conditions, with implications for the existence of equilibrium depth profiles based on forcing conditions.

4.1 Introduction

Complex systems of sandbars and channels are a key feature of ebb-tidal deltas, which occur on the seaward side of tidal inlets (*van der Vegt et al*., 2006) where ebb-tidal currents spread and weaken while depositing their sediment loads. Waves interact with the ebbing tidal currents to shape the overall morphology of ebb-tidal deltas (*Hayes*, 1980). Ebb-tidal deltas also shelter inlets by dissipating and redirecting wave energy (*Fitzgerald*, 1984; *Oertel*, 1988; *Sha*, 1989; *Hicks and Hume*, 1996). Ebb-tidal deltas aid in sediment bypassing by providing a mechanism for sediment to cross an inlet (*Syvitski and Saito*, 2007). Shallow sandbars and energetic forces at an ebb-tidal delta present challenges for maritime navigation. Despite the importance of ebb-tidal deltas, the hydrodynamic processes and morphodynamic evolution are not understood fully (*Fagherazzi and Overeem*, 2007).

Various modelling studies investigated the development of ebb-tidal deltas (d*e Swart and Zimmerman,* 2009). Numerical models are commonly used to help increase understanding of their dynamics because it is very difficult to investigate morphodynamic processes at ebb-tidal deltas through direct experiment, especially at morphodynamic timescales (ranging from weeks to years). Models allow for quantitative testing of hypotheses on the relative importance of processes which shape the delta morphology and, with calibration and validation, enable predictive capabilities. For example, a two-line empirical model successfully describes the large-scale dynamic response of deltas along the Dutch and German North Sea coast (*de Vriend et al*., 1994). *Van der Vegt et al*. (2006) focus on the morphology of ebb deposits by using an idealized two-dimensional ('2D') model and found that ebb-tidal deltas form as equilibrium morphology in response to tidal forcing. Detailed process-based models such as Delft3D have also been used to develop river mouth bars and test the sensitivity of development to directly opposing waves (*Nardin et al*., 2013).

So far, existing modelling studies either neglect waves, use very simple empirical relationships, or are detailed, multi-dimensional process-based

models. However, waves significantly impact hydrodynamic conditions at ebb-tidal deltas (e.g. *Olabarrieta et al.*, 2014), and play a major part in the development of ebb-tidal delta morphology when present (e.g. *Oertel*, 1972; *Hayes*, 1979). Empirical relationships can also be used to model ebb-tidal shoal dynamics, and certainly have the advantage of being fast and simple. However, they are not easily applied to multiple locations and require prior knowledge of the equilibrium state and transient evolution of deltas (e.g. *de Vriend et al.*, 1994). Detailed 2D and three-dimensional ('3D') process-based morphodynamic models are able to resolve spatial detail and represent dynamic interactions without previous knowledge of the morphodynamic state of the system. However, sometimes it is difficult to isolate the fundamental causal relationships from the complexity of these models. Moreover, the computational effort is greatest for detailed multi-dimensional process-based models, which makes it difficult to undertake extensive sensitivity testing.

The present Chapter proposes a process-based 'exploratory-type' (e.g. *Murray and Theiler*, 2004) morphodynamic model that parameterizes 3D ebb-tidal delta channel and bar formation from a quasi-2D current jet model and 1D cross-shore sediment transport formulation. Exploratory models are useful for improving fundamental understanding of the effects of forcing, and helpful in identifying knowledge gaps and providing hypothesis to test with more complex models. The approach presented here captures process-based interactions between currents, waves, and sediment but is simple enough to enable identification of critical relationships. Furthermore, the model is fast and able to fully develop delta morphology in less than an hour on a standard computer, allowing a full exploration of parameter sensitivities.

4.2 Methods

The generation of ebb-tidal delta shoals (also commonly called 'ebb-shoal', 'terminal lobe', 'mouth bar', or 'bar') seaward of a tidal inlet is explored using a dynamic coupling of a semi-analytical current jet model and a sediment transport model, and morphology updating. A quasi 2D turbulent jet model (developed in Chapter 3) is used to describe the hydrodynamic flow of an ebbing tidal jet ('ebb-jet') in the presence of directly-opposing waves (Figure 4.1). The flow is used to determine sediment transport using the Soulsby-van Rijn ('SvR') formulation for total load transport in the combined presence of current and waves (*Soulsby*, 1997). Sediment

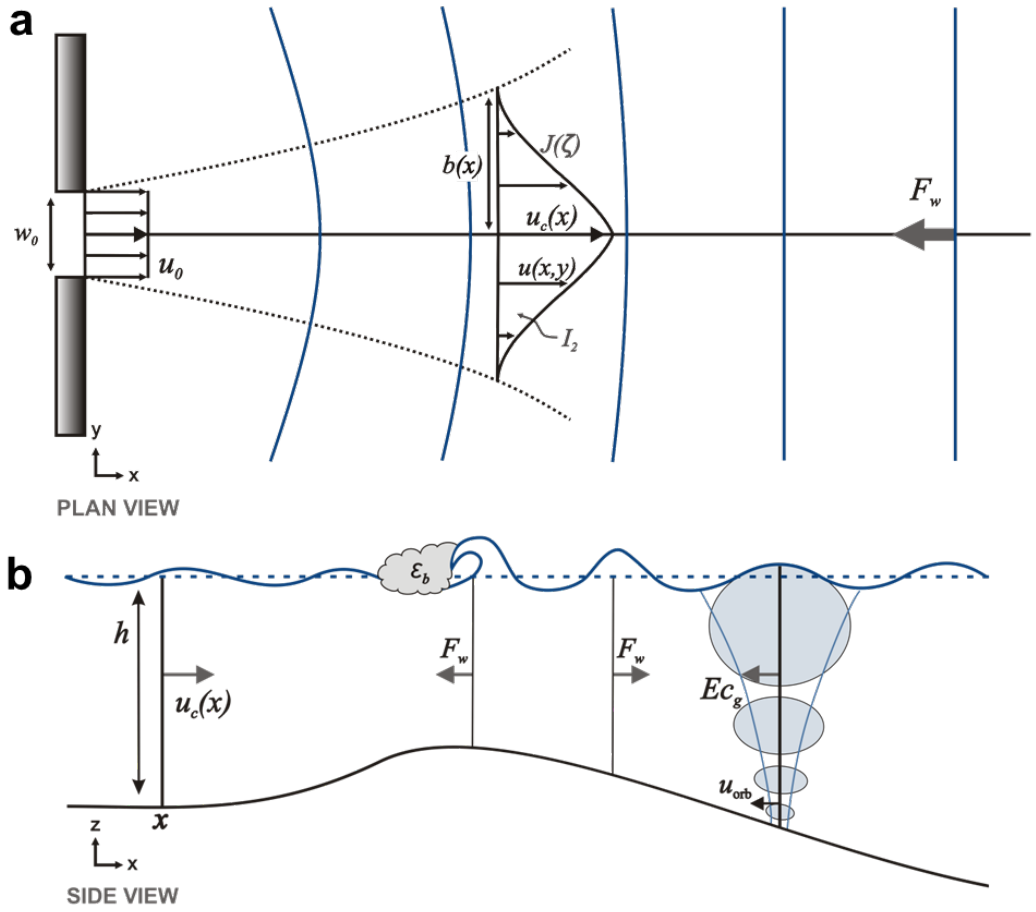

Figure 4.1. Schematic diagram of the idealized ebb-jet hydrodynamics represented by the simple model. (a) Plan view: For an inlet of width w_0 and velocity u_0, the ebb-jet is described by the half width $b(x)$ and centerline velocity $u_c(x)$. Jet velocity away from the centerline, $u(x,y)$ is assumed to decay with distance from the centerline with the similarity profile $J(\zeta)$ [Eq. (1)]. Blue curves are wave crests, with momentum flux F_w. (b) Profile view showing depth-averaged current and wave forcing over alongshore uniform depth profile $h(x)$. See text for details.

fluxes are used to modify the bathymetric depth profile over which the ebb-jet flows. The model coupling cycle is repeated to allow the evolution of morphology resulting from ebb-jet flow and directly opposing waves.

Our model is based on the assumption that the ebb-shoal is: (1) largely driven by the ebbing tide, with the flooding tides approaching the inlet through marginal channels (well away from the ebb-shoal), and (2) that the

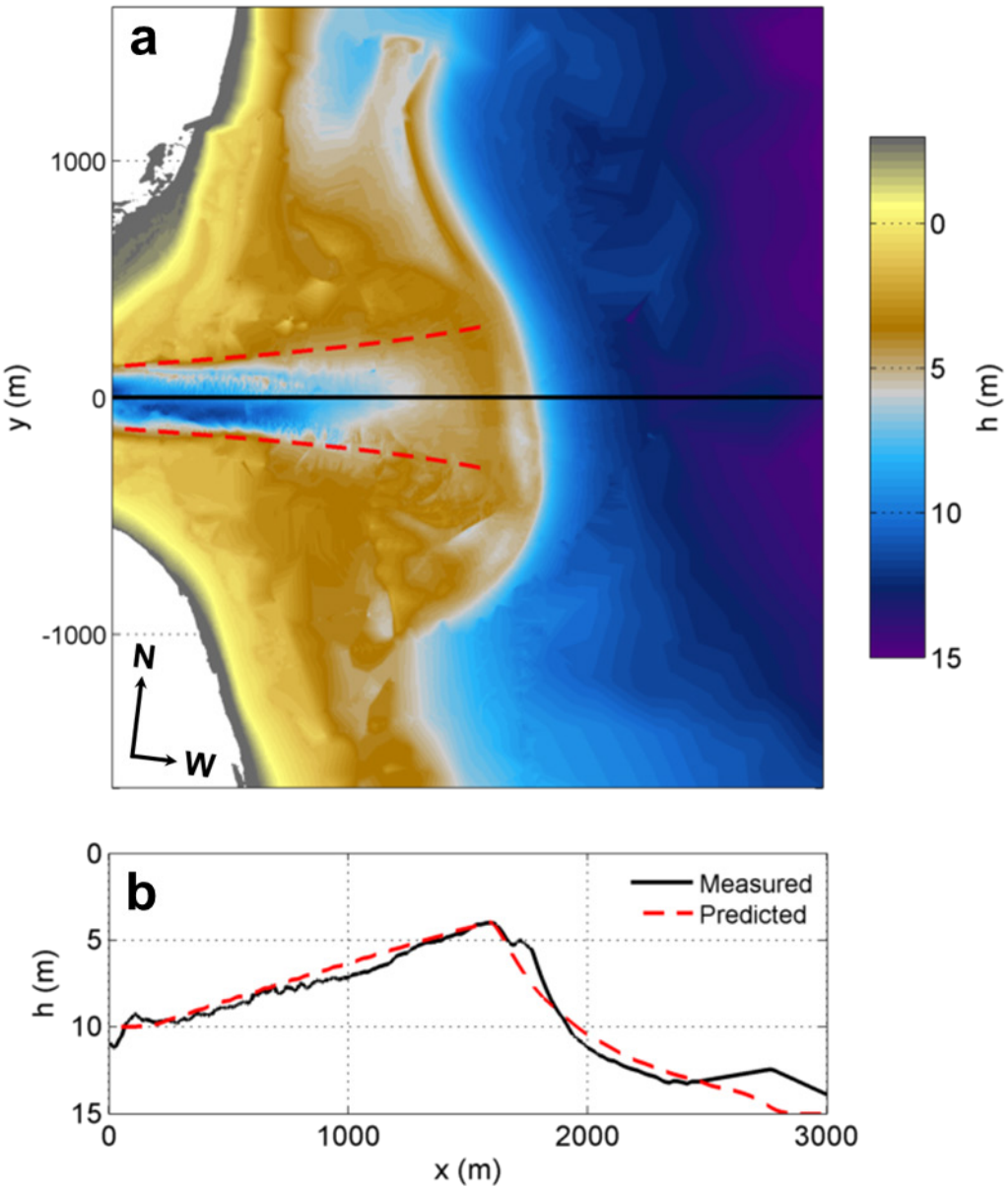

Figure 4.2. (a) Bathymetry data of the ebb-tidal delta at Raglan, New Zealand (rotated 7° and flipped horizontally to match orientation of model) with main channel thalweg (black line) indicated, and (b) the depth profile along the main channel thalweg (black line). Predicted channel width (red dashed line, a) and depth profile (red dashed line, b) for conditions similar to Raglan are shown for comparison.

ebb-shoal is completely symmetric along the centreline of the ebbing jet, and so can be entirely described by the evolution of processes along the centreline, with the lateral shape of both the jet and the shoal described by a simple shape function. Such an approach has been commonly used for modelling of jets (*Özsoy and Ünlüata*, 1982; *Joshi*, 1982; *Ortega-Sánchez et al.*, 2008), and even to drive sediment transport (*Özsoy*, 1986). However, such an approach has yet to be used as the basis for a simple morphology model. Free-form symmetric deltas in mixed-energy environments, like that at Raglan, New Zealand (Figure 4.2a) typically have a nearly symmetric ebb-shoal, a straight main channel, and shallow margin linear bars (or 'levees') (*Hayes*, 1980; *Hicks and* Hume, 1996).

4.2.1 Flow

The hydrodynamic flow is determined using a quasi-2D turbulent jet model. The jet model solves the vertically- and laterally-averaged jet momentum and continuity equations to determine jet streamwise velocity and width. The idealized, semi-analytical model solves the momentum balance along the ebb-jet centreline between an ebbing tidal jet at an inlet and an opposing wave field including by including only the processes of ebb-jet inertia balanced by bed shear-stress, turbulent mixing, and flux of excess momentum from waves shoaling and breaking (Figure 4.1). The cross-jet velocity profile is assumed to have a similarity profile shape (Figure 4.1a) given by (*Stolzenbach and Harleman*, 1971; *Özsoy* and *Ünlüata,* 1982)

$$J(\zeta) = \begin{cases} 0 & ; \quad 1 < \zeta \\ (1-\zeta^{1.5})^2 & ; \ 0 < \zeta < 1, \\ 1 & ; \quad \zeta < 0 \end{cases} \tag{4.1}$$

where ζ is distance in the cross-jet dimension normalized by the jet-half-width b (i.e. $\zeta = |y|/b$, where y is the alongshore distance from the jet axis). The model assumes a rigid-lid, so pressure gradients from wave setup are not considered. However, rather than driving a surface slope, the jet is instead forced to spread laterally.

The slowly-evolving hydrodynamic flow is calculated by solving the depth-averaged shallow water momentum and mass continuity equations

averaged over turbulent and wave timescales. The model considers processes of first-order significance, reducing the complexity of calculations. The vertically- and laterally-averaged jet x-momentum and jet mass continuity equations inside the jet are:

$$\begin{aligned} &I_1 h\frac{\partial(bu_c)}{\partial t} + I_2\frac{\partial(hbu_c^2)}{\partial x} = \frac{I_2 b}{\rho}\,\tau_{b,x} + \frac{I_2 b}{\rho}\,F_{\mathrm{t},\,x} + \frac{b}{\rho}\,F_{\mathrm{w},\,x}\,, \\ &h\frac{\partial b}{\partial t} + I_1\frac{\partial(hbu_c)}{\partial x} - ahu_c\frac{\partial b}{\partial x} = 0\,, \end{aligned} \tag{4.2}$$

where u_c is the streamwise jet centreline velocity, b is jet width, h is depth, ρ is water density, and a = 0.03 is the entrainment coefficient for inflow across the jet boundary (*French*, 1960). I_1 and I_2 originate from lateral-averaging the self-similarity profiles (*Stolzenbach and Harleman*, 1971; *Özsoy* and *Ünlüata,* 1982) given by

$$\begin{aligned} I_1 &= \int_0^1 (1-\zeta^{1.5})^2 d\zeta \;\approx 0.450, \\ I_2 &= \int_0^1 [(1-\zeta^{1.5})^2]^2 d\zeta \;\approx 0.316. \end{aligned} \tag{4.3}$$

The laterally-averaged bed shear-stress term is $I_2 b\tau_{b,x}$, where $\tau_{b,x}$ and turbulent mixing terms ($F_{\mathrm{t},\,x} = -\rho c_t u_c|u_c|$) use simple drag-like coefficients dependent upon the centreline velocity to dissipate momentum.. For simplicity, wave group and phase velocity, and wave height and propagation direction are assumed to be uniform across the jet (i.e., no wave refraction). This assumption leads to the laterally-averaged wave forces, based on the gradient in radiation stress, $bF_{\mathrm{w},\,x} = -b\partial\left(E\left(2c_g/c - 1/2\right)\right)/\partial x$ when waves are directly opposing the current ($\theta = 180°$). Wave energy is $E = \frac{1}{8}\rho g H_{rms}^2$, where H_{rms} is the root-mean squared wave height. The near-bed wave orbital velocity is calculated as $u_{orb} = \omega H_{rms}(2\sinh(kh))^{-1}$ (*Soulsby*, 1987). Alongshore uniform depth is required for the reduction of dimensions by lateral averaging, but the formation of channel morphology is parameterized, as described below (Section 2.4), introducing another dimension to morphological evolution.

The friction factor c_f is a scalar value applied uniformly throughout the domain. The weak flow approximation (*Liu and Dalrymple,* 1978) is used when waves are present, but without waves, $u_{orb} \to 0$ so the following approximation is used,

$$\tau_{b,x} = \begin{cases} -\rho c_f u_c u_{\text{orb}} & \text{with waves,} \\ -\rho c_f u_c |u_c| & \text{without waves.} \end{cases} \tag{4.4}$$

Seaward of the terminal end of the ebb-jet [the first (offshore from the inlet) zero-crossing (from offshore to onshore flow) in current velocity], the flow is composed purely of a vertically averaged wave-generated current along the x-axis. As such, the jet equations (4.2) are no longer valid and a depth-averaged 1D x-momentum equation is used, which combined with the 1-D mass continuity condition describes the flow in the region beyond the seaward extent of the ebb-jet as

$$h\frac{\partial u_c}{\partial t} + hu_c\frac{\partial u_c}{\partial x} = -c_f u_c|u_{\text{orb}}| - c_t u_c|u_c| - \frac{1}{\rho}\frac{\partial}{\partial x}\left[E\left(\frac{2c_g}{c} - \frac{1}{2}\right)\right]. \tag{4.5}$$

In the model, the wave field is determined by locally applying the linear dispersion relation with a (Doppler) shift for an opposing current, $\sigma^2 = (\omega - k \cdot u_c)^2 = gk \tanh kh$ (*Phillips*, 1977), where $\omega = 2\pi f$ is the observed (absolute) angular frequency and k is the wave number. The wavenumber and intrinsic angular frequency σ are locally applied along the profile. The dispersion relation is used to calculate the wave group and phase.

Wave dissipation is modelled by extending a wave height transformation formulation (*Thornton and Guza*, 1983) to include the effect of an opposing current on the wave frequency, given by

$$\frac{\partial E c_g}{\partial x} = \varepsilon_b = \frac{3\sqrt{\pi}}{16}\rho g B^3 \sigma \frac{H_{rms}^5}{\gamma^2 h^3}\left\{1 - \left[1 + \left(\frac{H_{rms}}{\gamma h}\right)^2\right]^{-\frac{5}{2}}\right\}, \tag{4.6}$$

where E is energy, B is a breaker coefficient that represents the fraction of foam region on the face of a breaking wave, and the breaker index $\gamma = H_b/h_b$ is an adjustable coefficient relating the height of waves at breaking,

H_b to the water depth at breaking, h_b. Wave height along the profile is given by the solution to equation (4.5).

4.2.2 Sediment Transport

Streamwise sediment transport rates along the jet centreline are determined with the SvR formulation (*Soulsby*, 1997). The formulation assumes that the vertical flux across the boundary between the seabed and suspended sediment is in equilibrium, and therefore does not consider advection of suspended material beyond neighbouring cells caused by a settling lag. For example, if sediment is advected into a cell from a neighbouring cell, it will instantaneously deposit in that cell if the current is less than the critical entrainment threshold. This is an assumption commonly used in systems that are dominated by sandy sediments (e.g. *Bijker*, 1967; *Soulsby*, 1997; van *Rijn et al.*, 2000). Furthermore an unlimited sediment supply at the inlet is assumed (which is governed by the current strength at the inlet boundary condition and the assumption that the sediment concentration is in equilibrium with this current), making the scheme transport-limited. Total load transport Q_x is given by the sum of locally-advected bed load, Q_{bx} and suspended load, Q_{sx} transport rates:

$$\begin{aligned} Q_{bx} &= A_{sb}(u_c\xi + u^s), \\ Q_{sx} &= A_{ss}u_c\xi, \end{aligned} \tag{4.7}$$

where A_{sb} and A_{ss} are bed-load and suspended load multiplication factors,

$$\begin{aligned} A_{sb} &= 0.005\left(\frac{D_{50}/h}{\Delta g D_{50}}\right)^{1.2} \quad , \\ A_{ss} &= 0.012 D_{50}\frac{D_*^{-0.6}}{(\Delta g D_{50})^{1.2}}. \end{aligned} \tag{4.8}$$

Here, $\Delta = (\rho_s - \rho)/\rho$ is the relative sediment density, g is gravitational acceleration, D_{50} is the median sediment grain diameter, and D_* is the dimensionless grain diameter,

$$D_* = \left(\frac{g\Delta}{\nu^2}\right)^{1/3} D_{50}, \tag{4.9}$$

and $\nu = 0.40$ is the kinematic viscosity.

The term ξ is a general multiplicative factor that governs the power of the transport relation, determines the relative effects of current and waves, and includes a critical velocity:

$$\xi = \left[\left({u_c}^2 + \frac{0.018}{C_f} u_{orb}^2 \right)^{1/2} - u_{cr} \right]^{2.4} (1 - 1.6 \tan \beta), \tag{4.10}$$

where C_f is the drag coefficient due to current, β is the bed slope, and u_{cr} is the critical velocity for the threshold of sediment motion (*van Rijn*, 1984),

$$\begin{aligned} C_f &= \left[\frac{\kappa}{\ln\left(\frac{h}{z0}\right) - 1} \right]^2, \\ u_{cr} &= \begin{cases} 0.19 D_{50}^{0.1} \log_{10}\left(\frac{4h}{D_{90}}\right) & \text{for } D_{50} < 0.0005 \text{ m}, \\ 8.5 D_{50}^{0.6} \log_{10}\left(\frac{4h}{D_{90}}\right) & \text{for } 0.0005 < D_{50} < 0.002 \text{ m}, \end{cases} \end{aligned} \tag{4.11}$$

where D_{90} is the 90th percentile of the mass of the sediment distribution by grain diameter.

Stokes drift u^s in equation 4.7 is represented in the bed load transport rate as the depth-averaged velocity of the wave-averaged wave-induced mass flux, $M_x^s = \int_{-h}^{0} \rho u^s dz = \frac{E}{\omega} k$, i.e. $u^s = \cos(\theta) \frac{kE}{\omega \rho h}$ where $\theta = 180°$ for directly opposing waves (e.g. *Dalrymple and Dean*, 1991, p. 287).

4.2.3 Updating Morphology

The gradient in total sediment transport rate is used to determine the location of convergences and divergences of cross-shore sediment flux along the jet centreline. Applying those sediment fluxes for a given time Δt, the change to the depth profile $\Delta h = h_{new} - h_{old}$ is given as

$$\frac{\Delta h}{\Delta t} = \mathrm{MF} \left(\frac{1}{1 - v_p} \right) \left(\frac{dQ_x}{dx} \right), \tag{4.12}$$

where MF is a morphological acceleration factor (*Ranasinghe et al.*, 2011) and v_p is the bed porosity or void space of the seabed composition.

Hydrodynamic flow is highly dependent upon the depth profile so the changes to the depth profile within a single cycle must be small enough that bed forms do not propagate more than one grid cell (dx) in one morphological time step ($\mathrm{MF} \times \Delta t$). *Ranasinghe et al.* (2011) propose a Courant-Friedrichs-Levy (CFL) criterion for morphological changes which includes MF as $CFL_{\mathrm{MF}} = C_{bed}\mathrm{MF}\Delta t/dx < 1$. Assuming a maximum speed for changes to the depth profile of $0.5\ \mathrm{m\ hr^{-1}}$ allows us to safely use $\mathrm{MF} = 85$ and $\Delta t = 5\ \mathrm{min}$ without violating the CFL_{MF} condition for the wide range of conditions trialled in this study.

The model is run until the imposed limit when the depth of the ebb-shoal crest reaches 40% of the inlet depth to avoid growing a bar beyond the capabilities of this model. Investigations of river mouths suggest that mouth bar evolution stagnates once the bar stops prograding as the depth of the crest is shallow enough to create an upstream fluid pressure capable of forcing the fluid around, rather than over the bar. As the flow over the bar decreases below critical, this leads to runaway aggradation. Model experiments using Delft3D show that river mouth bars stagnate at $h/h_0 < 0.40 = 40\%$ (*Edmonds & Slingerland*, 2007; *Nardin et al.*, 2013). This assumption is largely necessary because there is no mechanism to remove sediment in the model, e.g. alongshore drift.

4.2.4 Channelization

A major characteristic of all ebb-tidal deltas is a main channel, bounded laterally by levees on either side, that leads up to the terminal lobe and through which the ebb current flows (*Hayes*, 1980), e.g. Raglan, New Zealand (Figure 4.2a). Fully-developed channels restrict the lateral spreading of ebb jets, and force the flow seaward. To account for channelization in our model (for which the formulation assumes alongshore-uniform topography) a channelization parameter $ch \in [0,1]$ is used in the flow calculations. This simple parameterization enables the model to constrain lateral momentum transfer as fully developed channel morphology might, but without violating the assumption of axial-symmetric self-similarity of cross-jet flow that relies on the condition of alongshore

uniform bathymetry and allows for the lateral-averaging of the depth-averaged equations. The ch parameter limits the jet spreading in the presence of a channel by suppressing the non-stationary change in jet width $\partial b/\partial t$ (equation 4.1) such that the jet half-width at the next iteration becomes

$$b_{new} = b_{old} + (1 - ch)\frac{\partial b}{\partial t}, \tag{4.13}$$

where the channelization parameter ch is specified during initialization of the model as the ratio of the depth of the channel boundary to the depth of the thalweg at each x. Without the channel parameterization, the ebb-shoal migrates continuously shoreward, because the developing bar spreads (and weakens) the jet flow inshore of the bar causing a convergence in sediment flux.

The correct parameterization for channelization is a major source of uncertainty in my model, and is beyond the scope of this study, but is the subject of ongoing work. If the channel walls are set prior to starting the model, then the end point of the channel walls controls the location where the terminal bar forms. Presumably, the channel walls and terminal bar would develop in unison. Therefore, one possibility is to allow the channel walls to dynamically form alongside the lateral jet boundaries as the centreline morphology evolves. This is supported by the formation of channel margin linear bars, swash platforms and lateral delta flanks in natural systems that are shallower than the crest of the main ebb-shoal at the seaward end of the main channel (*Hayes*, 1980; e.g. Figure 4.2a). In the case of initiating the model without an ebb-tidal delta, the channelization is imposed dynamically as soon as a sandbar forms. During each bathymetric update, the channelization parameter is applied from the inlet ($x = 0$) to the crest of the shallowest sandbar along the depth profile. Since the model is stopped once the depth of the sandbar crest reaches 40% of the inlet depth, the scheme does not need to allow for channel bifurcation. Also, since the levees are typically shallower than the ebb-shoal, the jet is considered fully channelized with $ch = 1$ from the inlet to the cross-shore position of the ebb-shoal crest and $ch = 0$ seaward

of the crest. A 100 m long cross-shore taper from 1 to 0 is included seaward of the ebb-shoal crest to reduce sharp discontinuities in the model which can induce instabilities, but is generally not needed. Again, this is one possible channelization parameterization scheme and a major source of uncertainty on which delta morphology is dependent.

4.3 Developmental Scale Dynamics

4.3.1 Developing a Natural Profile

The morphology of an ebb-tidal delta is a function of the interaction of tidal currents and waves (*Hayes*, 1980), and form as a morphodynamic equilibrium solution to those forcing conditions (*van Leeuwen et al.*, 2003). The first challenge was to develop such an equilibrium bathymetry from what are usually non-equilibrium initial conditions. Simulations began with a generic but smooth concave-up inner-shelf basin void of sandbars with a prescribed inlet depth $h_0(0) = 10\ \mathrm{m}$ and offshore boundary $h_{end}(3000) = 15\ \mathrm{m}$, and assumed alongshore uniform depth (Figure 4.4b, black dashed line). Initial flow conditions along the domain were determined by applying a constant inlet velocity at the inlet of width $b = 100\ \mathrm{m}$ for 1 hour, ensuring the initial hydrodynamic conditions fully propagated throughout the model domain before evoking sediment transport calculations. The resulting jet solution was used as the initial flow condition in the coupling between the hydrodynamic and morphodynamic models.

Sediment fluxes along the domain were determined with the SvR formulation. The sediment flux was applied for 5 minutes and enhanced with $\mathrm{MF} = 85$ to calculate the bed level changes to the depth profile. Then the flow was recalculated on the new depth profile, but only for 10 minutes since the small changes to the depth profile result in small hydrodynamic changes. This process was repeated until a natural depth profile was built with an ebb-shoal crest position approaching the imposed stagnation point when the depth of the crest reached 40% of the inlet depth. Although the model simulations were able to continue past the stagnation point, the evolution behaviour was unnatural as ebb-shoal crests grew shallower and moved further shoreward as the ebb-jet was compressed longitudinally

shoreward and expanded laterally over shallower depths. However, using the imposed stagnation point, the ebb-shoal and channel morphologies developed by the model were similar to observations of deltas in the field, for example at Raglan, New Zealand (shown in Figure 4.2a), New River Inlet, NC (shown in Figure 3.4a), and at Langeoog, Germany (shown in Figure 1.2).

However, to build confidence in the modelled morphology, forcing conditions similar to those at Raglan, New Zealand were used to develop an ebb-shoal and channel (Figure 4.2). Figure 4.2a shows a bathymetric surface composed of data from a multi-beam echo-sounder survey through the main channel and ebb-shoal, single-beam echo-sounder surveys along the nearshore delta flanks and levees, and LiDAR on the intertidal zones and beaches. The inlet width is approximately 300 m wide at mid-tide (i.e. $b_0 = 150\ \mathrm{m}$). Multiple combinations of forcing conditions were trialled, but the best comparison of ebb-shoal crest position between predicted and observed depth profiles was achieved with an inlet boundary condition of $u_c(0) = 2.8\ \mathrm{m\ s^{-1}}$ without waves. When waves were included, the ebb-shoal crest formed too far shoreward of the observed position. Previously, the jet model over predicted the effects of waves on the mean-flow on the shallow ebb-shoal at New River Inlet, NC, a limitation of the jet model that also impacts the development of ebb-shoal morphology. The predicted ebb-shoal crest position was 6 m from the (smoothed) measured crest and within 4 cm vertically. The predicted channel width is very similar to that of Raglan, but without the lateral undulations from swash bars as seen in the measurements. Also, the model assumes a flat bottom channel, whereas the Raglan channel is concave, with relatively steep channel walls near the inlet that become less steep with distance – which make it difficult to clearly define observed channel width. The ebb-jet velocity boundary condition $u_c(0) = 2.8\ \mathrm{m\ s^{-1}}$ is within the typical range of ebb-jet velocity ($2.2\text{-}3.0\ \mathrm{m\ s^{-1}}$) at the Raglan (Whaingaroa) Harbour mouth (personal observation). However, the absence of waves is rare at Raglan which has a mean significant wave height of $1.8\ \mathrm{m}$ (*Gorman et al.*, 2003). Further work will calibrate the wave

transformation model with observations, as the shoreward driving force in the model is sensitive to the way in which wave dissipation (e.g. breaking) is parameterized.

4.3.2 Sensitivity to Ebb-Jet and Wave Conditions

Six simulations were run with the aim of identifying the relative impact of flow conditions on the development of ebb-shoal and channel morphology. For the series of simulations, each run was consistent with the others in all but flow boundary conditions. The runs presented here all consisted of sediment with the characteristics of $D_{50} = 200\ \mu\text{m}$ (fine sand), $D_{90} = 500\ \mu\text{m}$ (i.e. $2.5D_{50}$), material density $\rho_s = 2650\ \text{kg m}^{-3}$ (e.g. quartz), and a bed porosity $v_p = 0.6$. The flow boundary conditions varied between runs by varying the inlet velocity applied to the inlet boundary (left) and varying the offshore wave conditions applied at the seaward boundary (right). Two ebb-jet velocity conditions were applied at the inlet, $u_{c,0} = 1.0\ \text{m s}^{-1}$ and $u_{c,0} = 2.0\ \text{m s}^{-1}$ representing common depth-averaged velocity at peak ebb flows during neap and spring tides. Three wave conditions were simulated, each with peak period $T_p = 10\ \text{s}$ and significant wave height $H_s = [0, 0.5, 1.0\ \text{m}]$.

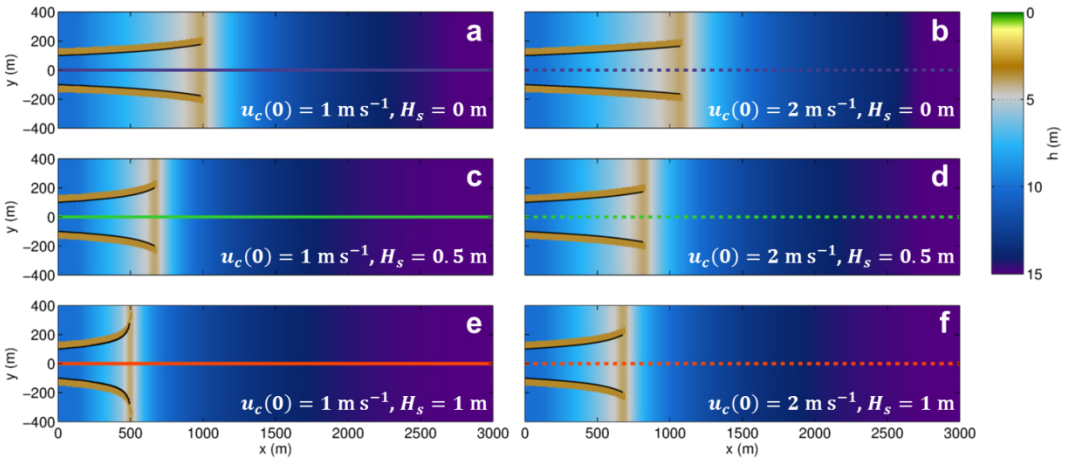

Figure 4.3. Channel and bar morphology developed to $h/h_0 < 0.40$ at the bar crest for (a) $u_0 = 1.0\ \text{m s}^{-1}$, without waves, (b) $u_0 = 2.0\ \text{m s}^{-1}$, without waves, (c) $u_0 = 1.0\ \text{m s}^{-1}$, $H_s = 0.5\ \text{m}$, $T_p = 10\ \text{s}$, (d) $u_0 = 2.0\ \text{m s}^{-1}$, $H_s = 0.5\ \text{m}$, $T_p = 10\ \text{s}$, (e) $u_0 = 1.0\ \text{m s}^{-1}$, $H_s = 1.0\ \text{m}$, $T_p = 10\ \text{s}$, and (f) $u_0 = 2.0\ \text{m s}^{-1}$, $H_s = 1.0\ \text{m}$, $T_p = 10\ \text{s}$. The thalweg positions are marked with colored solid and dashed lines, with corresponding depth profiles shown in Figure 4b.

Figure 4.3 shows the position of the ebb-shoal crests of the developed channel depth profiles and channel widths as they changed when the initial flow and wave conditions were varied, (also compared in Figure 4.4). Final channel half-width, [$b(\mathrm{bar})$], bar crest position [$x(\mathrm{bar})$], and development time [$t(\mathrm{bar})$] for every run are listed in Table 4.1. Without waves (runs 1 and 2), the final depth profile and channel width were very similar for both slow and fast ebb-jet currents at the inlet; then channel widths only differed by $13\ \mathrm{m}$ and the cross-shore ebb-shoal crest positions differed by $85\ \mathrm{m}$ (Figure 4.3a and 4.3b; Figure 4.4a and 4.4b). Run 1, with the slower ebb-jet current at the inlet had a slightly wider channel, shorter distance from the inlet to the bar crest, and steeper sloping terminal lobe than run 2 which had a faster ebb-jet current at the inlet (solid and dashed blue lines, Figure 4.4a and 4.4b). Channel width increased and the cross-shore distance from the inlet to the ebb-shoal crest decreased with wave height (Figure 4.3; Figure 4.4a and 4.4b). The ability of waves to increase channel width was greater for runs with slow ebb-jet current at the inlet (Scenarios 1,3,5) than for scenarios with fast ebb-jet current at the inlet (Scenarios 2,4,6). Also, the ability of waves to decrease cross-shore distance from inlet to ebb-shoal crest was less with slow, rather than fast, ebb-jet current at the inlet. This is seen by differencing the crest position

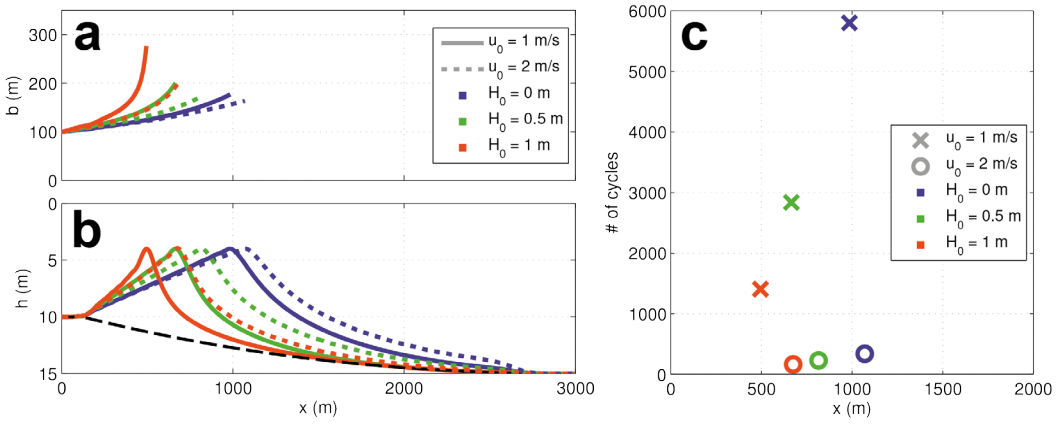

Figure 4.4. Characteristics of developed ebb-tidal delta morphology for 6 different simulations; (a) channel-width, (b) thalweg depth profile, and (c) the number of model-coupling cycles for the bar to develop vs cross-shore bar position of developed bar. Runs with $u_0 = 1.0\ \mathrm{m\ s^{-1}}$ and $u_0 = 2.0\ \mathrm{m\ s^{-1}}$ are indicated with solid lines and dashed lines in (a-b) or 'x' and 'o' symbols in (c), respectively. Color indicates wave height.

$x(\text{bar})$ by inlet condition, i.e.

$$\Delta x(\text{bar})|_{u_{c,0}=2\,-\,u_{c,0}=1} = \begin{cases} 85 \text{ m for } H_s = 0 \\ 150 \text{ m for } H_s = 0.5 \\ 180 \text{ m for } H_s = 1 \end{cases}.$$

The relative effects of waves on the ebb-shoal and channel morphology increased as ebb-jet velocity decreased.

Table 4.1 Flow conditions and sediment characteristics for the developmental model scenarios simulated in this study. *Runs 2 and 6 use default sediment characteristics and are compared to the runs in each of the sediment characteristic subsets.

Run	u_c (m s^{-1})	H_s (m)	T_p (s)	D_{50} (μm)	D_{90} (μm)	ρ_s (kg m^3)	v_p	$b(\text{bar})$ (m)	$x(\text{bar})$ (m)	$t(\text{bar})$ (cyc's)
Flow conditions										
1	1	0.0	n/a	200	500	2650	0.6	177	985	5803
2*	**2**	**0.0**	**n/a**	**200**	**500**	**2650**	**0.6**	**164**	**1070**	**340**
3	1	0.5	10	200	500	2650	0.6	200	665	2838
4	2	0.5	10	200	500	2650	0.6	173	815	229
5	1	1.0	10	200	500	2650	0.6	277	495	1406
6*	**2**	**1.0**	**10**	**200**	**500**	**2650**	**0.6**	**197**	**675**	**164**
Sediment characteristics – Median grain size										
7	2	0	n/a	80	200	2650	0.6	162	1070	173
8	2	1	10	80	200	2650	0.6	192	685	84
9	2	0	n/a	400	1000	2650	0.6	165	1070	549
10	2	1	10	400	1000	2650	0.6	201	675	264
11	2	0	n/a	800	2000	2650	0.6	167	1090	986
12	2	1	10	800	2000	2650	0.6	210	675	467
13	2	0	n/a	1800	4500	2650	0.6	168	1135	2278
14	2	1	10	1800	4500	2650	0.6	230	665	1035
Sediment characteristics – Grain size distribution										
15	2	0	n/a	200	250	2650	0.6	164	1070	350
16	2	1	10	200	250	2650	0.6	196	675	169
17	2	0	n/a	200	1000	2650	0.6	165	1060	327
18	2	1	10	200	1000	2650	0.6	198	675	159
Sediment characteristics – Grain material density										
19	2	0	n/a	200	500	1800	0.6	161	1090	125
20	2	1	10	200	500	1800	0.6	193	695	61
21	2	0	n/a	200	500	3600	0.6	166	1060	635
22	2	1	10	200	500	3600	0.6	203	670	307
23	2	0	n/a	200	500	5000	0.6	166	1060	1158
24	2	1	10	200	500	5000	0.6	208	660	555
Sediment characteristics – Bed void space										
25	2	0	n/a	200	500	2650	0.2	165	1060	675
26	2	1	10	200	500	2650	0.2	202	670	325
27	2	0	n/a	200	500	2650	0.4	165	1065	506
28	2	1	10	200	500	2650	0.4	199	670	244

The amount of time required to develop a bar was substantially dependent on flow conditions. Without waves, the time required to develop final depth profiles differed between runs 1 and 2, as run 2 with fast ebb-jet current at the inlet developed in only 6% of the time required by run 1 with slow ebb-jet current at the inlet. In runs with slow ebb-jet current at the inlet, the time required to develop final depth profiles decreased by approximately 50% for each half-meter increase in wave height (i.e. $H_s = 0 \text{ to } 0.5 \text{ m and } H_s = 0.5 \text{ to } 1.0 \text{ m}$). In contrast, the time required to develop the final depth profile by runs with fast ebb-jet current at the inlet decreased by only 30% per half-meter increase in wave height. All runs with a slow ebb-jet current at the inlet took longer than all of the runs with a fast ebb-jet current at the inlet (Figure 4.4c).

4.3.3 Sensitivity to Sediment Characteristics

Twenty-four simulations were run with the aim of illustrating the sensitivity of sandbar mobility to sediment characteristics. Ebb-tidal deltas are often composed of multiple sediment types within their stratigraphy corresponding to changes in sediment supply during development. However, here we assumed that only a constant sediment type was available throughout the simulation. Two different flow scenarios, (a) 'wave dominated flow' $u_{c,0} = 2.0 \text{ m s}^{-1}$, $H_s = 1.0 \text{ m}$, $T_p = 10 \text{ s}$ and (b) 'jet dominated flow' $u_{c,0} = 2.0 \text{ m s}^{-1}$, $H_s = 0 \text{ m}$ were used to force morphological development with domains consisting of different sediment characteristics, i.e. median grain size (D_{50}), range of grain size distribution (D_{90}), grain material density (ρ_s), and bed porosity or void space (v_p). Although a full grain size distribution was not modelled, the effect of changes to the distribution was parameterized by adjusting the D_{90} grain size relative to the D_{50} grain size. The boundary conditions are described in Table 4.1, scenarios 2, 6, and 7-28. Scenarios 2 and 6 used the default sediment characteristics ($D_{50} = 200 \text{ µm}$, $D_{90} = 2.5D_{50}$, $\rho_s = 2650 \text{ kg m}^{-3}$, and $v_p = 0.6$) and are compared within each subset of sediment characteristic runs. The full range of values for each of the sediment characteristics were $D_{50} = [80, 200, 400, 800, 1800 \text{ µm}]$ (i.e. very fine sand,

fine sand, medium sand, coarse sand, and very coarse sand), $D_{90} = [1.25D_{50}, 2.5D_{50}, 5D_{50}]$, $\rho_s = [1800, 2650, 3600, 5000\ \mathrm{kg\ m^{-3}}]$, and $v_p = [0.2, 0.4, 0.6]$.

All scenarios were initialized with the same depth profile (concave-up and smoothly tapered from $h(0) = 10\ \mathrm{m}$ to $h(3000) = 15\ \mathrm{m}$). Sandbars were tracked during the simulations. Each simulation repeated the model-coupling cycle until the ebb-shoal crest depth reached 40% of the inlet depth.

All four sediment characteristics tested impacted the development of channel/bar morphology less than variations in either ebb-jet current or waves. However, for the characteristics trialled, varying median grain size caused the largest range [i.e. $\max(x(\mathrm{bar})) - \min(x(\mathrm{bar}))$] of bar crest positions ($65\ \mathrm{m}$ without waves, $20\ \mathrm{m}$ with waves), followed by grain material density ($30\ \mathrm{m}$ without waves, $35\ \mathrm{m}$ with waves). Both grain size distribution and bed porosity had very little effect on bar crest position ($\leq 10\ \mathrm{m}$). These ranges are small in comparison to the range of ebb-shoal crest positions for wave conditions on slow ebb-jet currents ($490\ \mathrm{m}$) or fast ebb-jet currents ($395\ \mathrm{m}$).

Ebb-shoal crest position was positively correlated with median grain size

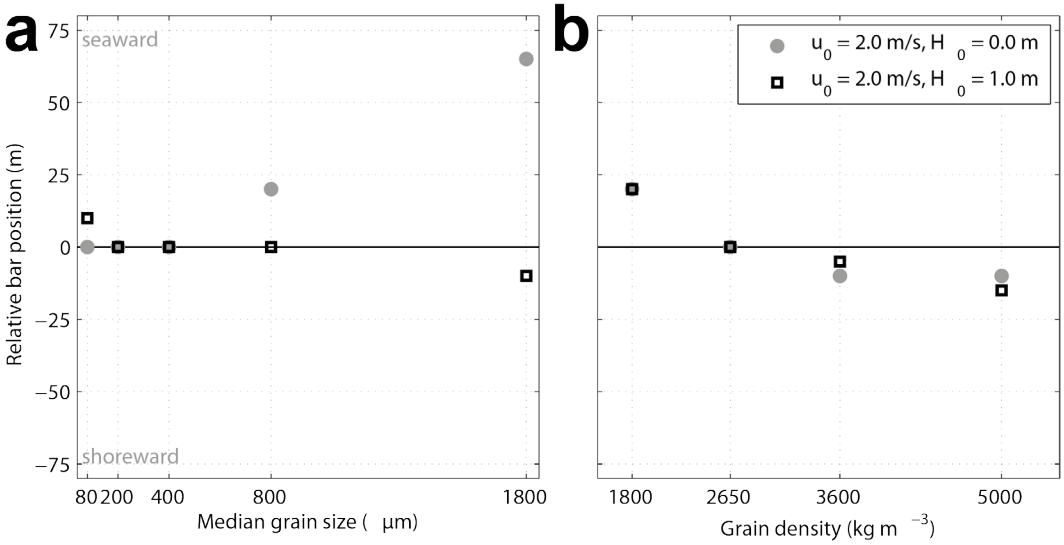

Figure 4.5. The cross-shore position of the developed bar crest by sediment characteristic; (a) median grain size, and (b) material grain density relative to the default values of $D_{50} = 200\ \mu\mathrm{m}$ and $\rho_s = 2650\ \mathrm{kg\ m^3}$.

in the absence of waves (coarser-grained bars were further seaward, grey circles, Figure 4.5a) but negatively correlated with median grain size when waves were present (black squares, Figure 4.5a). The relationship was clearer without waves. Ebb-shoal crest position was negatively correlated with grain material density whether waves were present or not (Figure 4.5b). The relationship between ebb-shoal crest position and grain material density was nearly identical in scenarios with or without waves.

All four sediment characteristics that were tested affected the rate of morphological development (Figure 4.6). The median grain size had the largest impact on ebb-shoal development time (Figure 4.6a), followed by

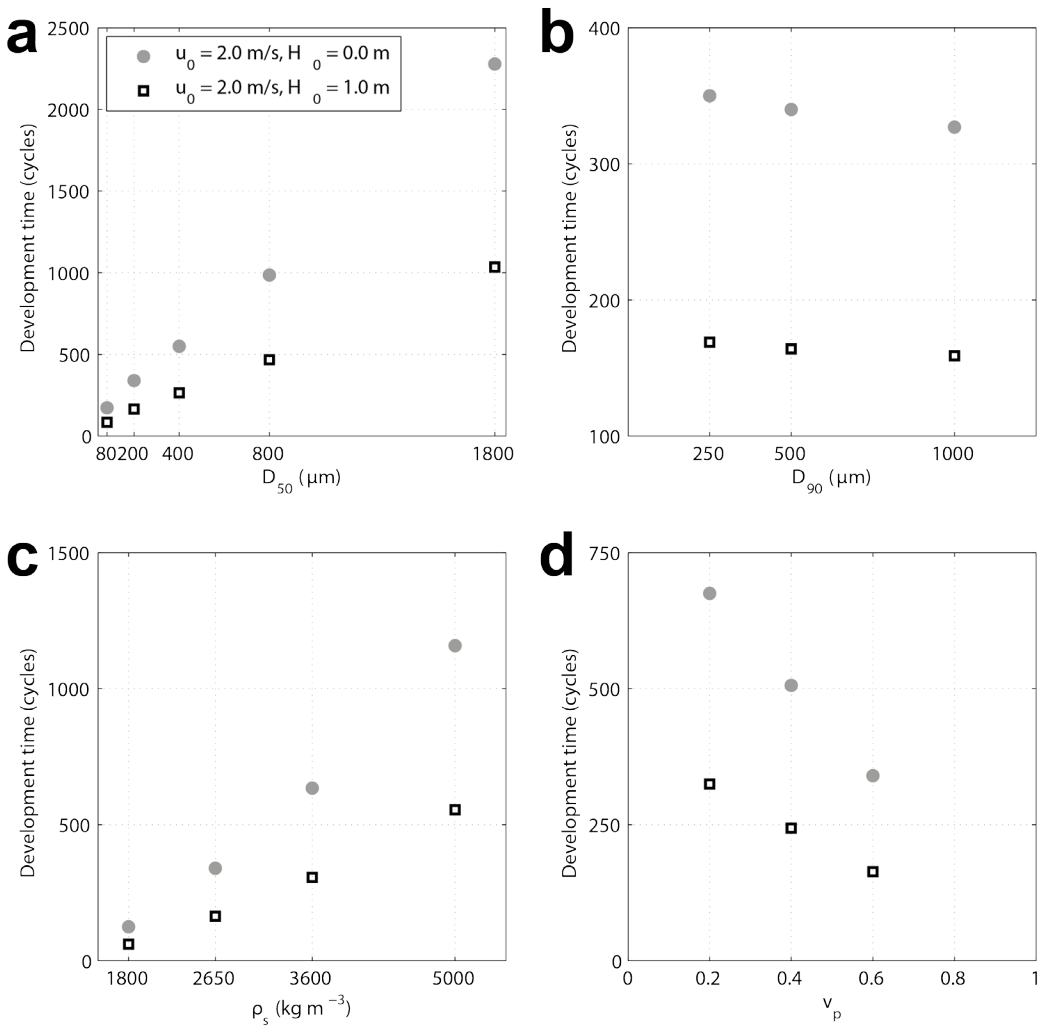

Figure 4.6. Sensitivity of sandbar development to sediment characteristics; Number of model-coupling cycles to bar stagnation by, (a) median grain size, (b) grain size distribution (indicated by D_{90} relative to a median grain size $D_{50} = 200\,\mu m$), (c) material grain density, and (d) the porosity of the bed based on fraction of void space.

grain material density (Figure 4.6c), bed porosity (Figure 4.6b), and finally grain size distribution (Figure 4.6d). Development time was directly dependent on median grain size, ranging from 173 cycles for very fine sand up to 2278 cycles for very coarse sand without waves. Development time was also directly dependent on grain material density, ranging from 125 up to 1158 cycles without waves. Development time was inversely dependent on the D_{90} grain size, or rather the relative range of sediment grain size distribution, but the time difference between runs was only 23 cycles between the narrowest and broadest distributions. Development time was also inversely dependent on the fraction of bed void space, ranging from 675 cycles for the most compacted beds to 340 cycles for the loosest beds. For all sediment characteristics trialled, the development time for runs with $1\ \mathrm{m}$ waves was slightly less than half (~48-49%) of the time required by similar runs without waves.

4.4 Short-Term Response

In situations where an ebb-tidal delta is already well-established and roughly in equilibrium with its long-term (e.g. annual to decadal) forcing climate (e.g. Raglan, see Chapter 2), the exploratory model can also be used to examine the short-term morphological response to changes in forcing patterns. However, a few changes are made in the model assumptions and procedure to bridge gaps in the knowledge of significant morphodynamic processes. Recall that in the previous section (4.3), the assumption was made that the development of ebb-shoals stagnate as $h/h_0 \rightarrow 0.40\ (40\%)$, i.e. ebb-shoal and channel morphology reaches a developmental equilibrium. Here we consider short-term changes to that longer-term equilibrium under changes in the forcing conditions. As the changes are only short-term, the channel width is held constant over the period of time considered and the crest of the ebb-shoal is permitted to grow slightly larger to $h/h_0 < 0.20\ (20\%)$ under the assumption that short-term responses can vary from the longer-term equilibrium conditions because they occur at shorter timescales.

The first assumption, that channel width remains constant, is necessary in the absence of a mechanism for lateral channel infilling (i.e. the channel cannot contract). Without the ability for the channel to contract, it will always grow wider whenever the ebb-shoal grows in size and moves shoreward, eventually leading to a complete inlet closure. Of course, in reality this does not happen, as the ebb-jet deposits sediment along its margins where the local shear velocity of the jet falls below the critical shear velocity for entrainment into suspension and which grow into levees (*Rowland et al.,* 2010). Once formed, levees were observed in flume experiments to increase turbulence in the ebb-jet by 3-5 times, and produce lateral shear stresses and momentum diffusivities that are one to two orders of magnitude greater than by bed friction alone (*Rowland et al.*, 2009). The increased turbulence, lateral shear stresses and momentum diffusivities also contribute to further levee growth and inhibit further lateral spreading of jet momentum. These processes are not represented in the exploratory model, but their effects are partially met by setting the channel width to be fixed during the short-term simulations.

The second assumption, allowing the crest of the ebb-shoal to grow up to a depth 20% of the inlet depth, is reasonable given that the simulations are short-term. Since channel width is fixed, the additional height on the ebb-shoal will not cause channel bifurcation.

Without field evidence, we speculate that the alongshore position of channel levees changes at a slower timescale than the cross-shore position of an ebb-shoal. This notion is supported by the observation of nearshore coastal change along beaches, with intra-annual changes being dominated by cross-shore fluxes, and inter-annual to decadal coastal change attributed to alongshore fluxes (e.g. *Ruggiero et al.*, 2009). However, it was not evident in the video observations at Raglan (Chapter 2), likely due to occurrence of swash bars moving into the channel margins during wave events with a non-zero incident angle.

Starting with quasi-realistic ebb-shoal and channel model domains, we examine the response of the depth profile to boundary and initial conditions, identifying sensitivities within the model.

4.4.1 Sensitivity to Channel Width

Initial states of channel morphology were approximated with support from rectified video observations of the ebb-tidal delta at Raglan. The depth profile of the channel thalweg was measured from the multibeam bathymetry data provided by Waikato Regional Council (Figure 2.1 and Figure 4.2) of the ebb-tidal delta at Raglan (see Appendix A for details). Levee positions were digitized from video images of a few characteristic channel morphologies, 'narrow', 'medium', and 'wide' and are shown in Figure 4.7a-c with black lines. The digitized levee positions were rotated into coordinates based on the channel thalweg line (Figure 4.2), then differenced and approximated by a 4th order polynomial along the thalweg axis smoothly approximate channel width. Those idealized channel width approximations are shown in Figure 4.7d-f and were then used to simulate

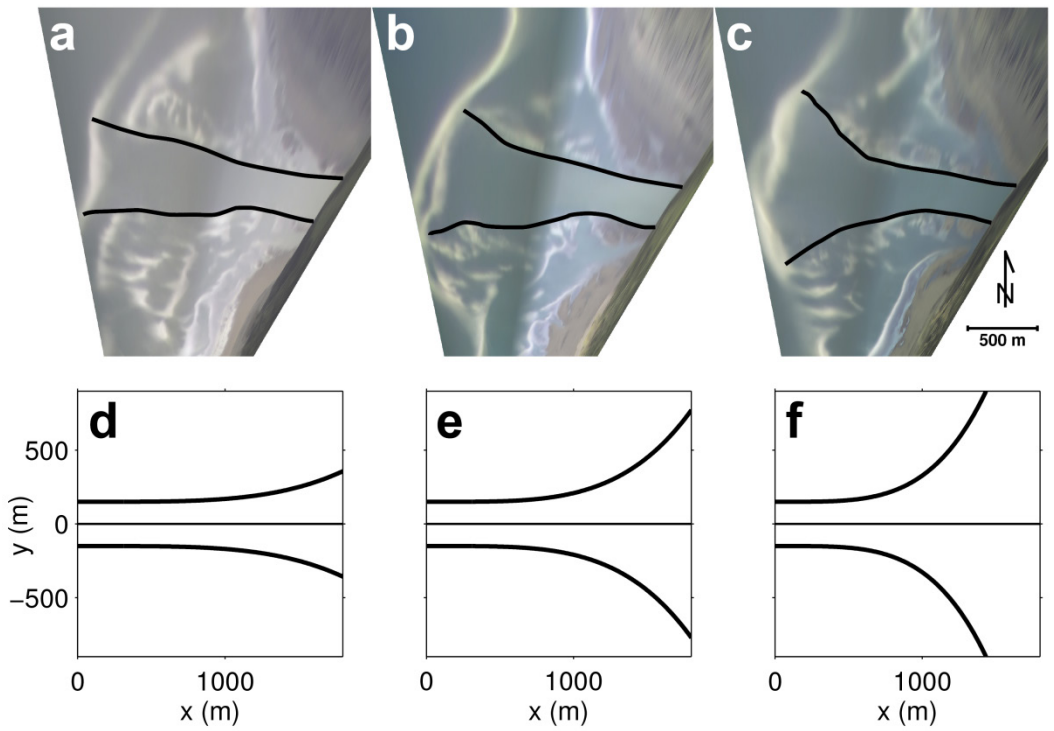

Figure 4.7. Geo-rectified video time-exposure observations of the ebb-tidal delta at Raglan with (a) narrow, (b) medium and, (c) wide channel width morphology, with levee position is indicated with black lines. The idealized channels are shown below with (d) narrow, (e) medium, and (f) wide widths.

the short-term depth profile response to boundary conditions.

Each of three idealized channel scenarios differing only by the initial, static channel width (narrow, medium, and wide, Figure 4.7d-f) were run with two different forcing scenarios, 'jet dominant' and 'wave dominant'. The jet dominant and wave dominant forcing scenario were defined as $H_s = 1\ \mathrm{m}$, $T_p = 10\ \mathrm{s}$, and $u_{o,c} = 2.2\ \mathrm{m\ s^{-1}}$ and $H_s = 2\ \mathrm{m}$, $T_p = 10\ \mathrm{s}$, and $u_{o,c} = 1.2\ \mathrm{m\ s^{-1}}$, respectively. The initial depth profile was the same in all six simulations and was the simplified Raglan thalweg measured from multibeam data (Figure 4.2b, black line; Figure 4.8a and 4.8b, dashed black line). Each of six simulations ran until the shallowest crest depth along the depth profile reached 20% of the inlet depth (~2m below msl).

The resultant depth profiles (Figure 4.8a and 4.8b) differed substantially between the two forcing scenarios. The depth profiles from each of the wave dominant cases were characterized by the formation of a relatively narrow ($< 190\mathrm{m}$ wide at the base) pronounced sandbar at the seaward edge of the ebb-shoal. The depth profiles from each of the jet dominant cases were characterized by a broad sandbar (almost a shoreward extension of the ebb-shoal) inshore from the initial bar crest. For the wave dominant forcing scenarios, the effects of channel width to morphological response influenced the cross-shore position of the sandbar crest and rate

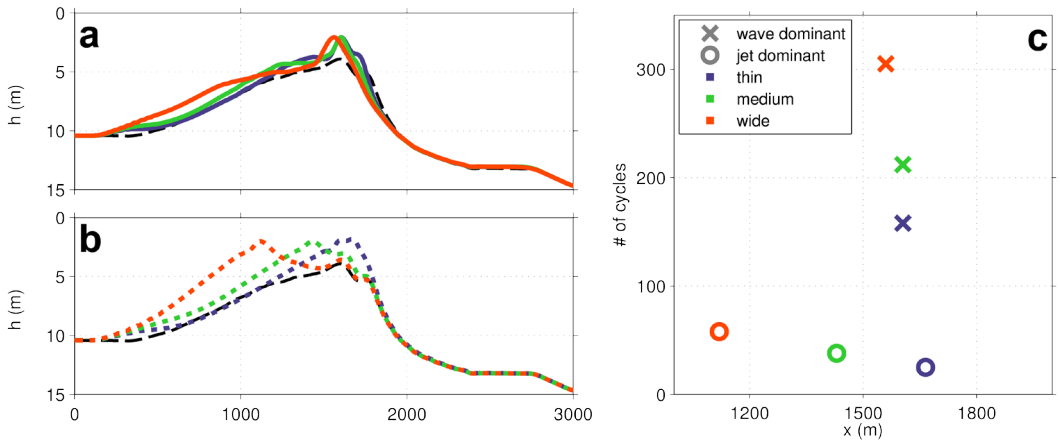

Figure 4.8. Three static channel widths, narrow (blue), medium (green), and wide (red) with wave dominant (solid lines and 'x's) and jet dominant (dashed lines and circles) forcing scenarios; (a) Wave dominant and (b) jet dominant depth-profiles h vs. distance from the inlet x. (c) Response rate of the 6 simulations based on the number of cycles before reaching stopping criteria.

of bar response. The sandbar crest was nearly $100\ \mathrm{m}$ further shoreward in the wide channel run than the other two channel configurations (Figure 4.8a). Also, the narrow channel maintained a steeper seaward edge of the terminal lobe (Figure 4.8a, blue line). The rate of response was greater with channel width, with the wide channel run taking roughly twice the number of cycles as the narrow channel (over 300 cycles for wide compared to 160 cycles for narrow) run to reach the 20% of the inlet depth target. The channel width had a greater influence on the sandbar crest position for the jet dominant rather than wave dominant forcing scenarios. The crest position in the wide channel run was nearly $570\ \mathrm{m}$ further shoreward than in the narrow channel run, and $320\ \mathrm{m}$ shoreward from the medium channel width sandbar crest (Figure 4.8b). The response rate was also faster with channel width in the jet dominant runs, but the response rate of all jet dominant runs were much faster than the wave dominant runs (Figure 4.8c circles vs 'x's). The narrow channel jet dominant depth profile was most similar to the wave dominated depth profiles.

4.4.2 Sensitivity to Forcing Conditions

Starting with a developed depth profile that has a relatively deep ($5\ \mathrm{m}$ or 50% of inlet depth) and broad ebb-shoal free from sandbar crests (i.e. flat on top), a series of model runs were carried out, each differing only by the forcing conditions applied to the inlet and seaward boundaries. Significant wave height varied between $0.5\ \mathrm{m}$ to $2.5\ \mathrm{m}$ with half metre increments, but remained constant throughout each model run. Wave period was $10\ \mathrm{s}$ in all events. The centreline ebb-jet current speed at the inlet also varied between runs with values between $0.5\ \mathrm{m\ s^{-1}}$ to $2.5\ \mathrm{m\ s^{-1}}$ at increments of $0.5\ \mathrm{m\ s^{-1}}$. In all, 25 model runs were allowed to run, with evolving depth profiles, until a sandbar crest reached 20% of the inlet depth (i.e. 2m). However, depth profiles from the runs were compared at a particular time along during their evolution to emphasize their relative response rates. The 25 depth profiles after 150 cycles (or less for simulations that reached the 20% inlet depth cut-off before 150 cycles) are shown in Figure 4.9 with the inlet current speed boundary conditions increasing in axes toward the right of the figure and wave height boundary conditions increasing in axes

down the figure. In each axes, the black solid line indicates the evolved depth profile after the number of cycles (indicated in the upper left corner in orange font), the position of sandbar crest is indicated with a red dot, and the cross-shore crest position written with red font. The grey dashed lines indicate the initial depth profile.

In the model runs with slow current at the inlet ($u_{0,c} = 0.5$ and $1\ \mathrm{m\ s^{-1}}$) there was very little bathymetric response. In each of these runs, a single small sandbar formed at positions increasingly seaward with increased wave height and increased current speed. The response was greater with the $1\ \mathrm{m\ s^{-1}}$ runs than the $0.5\ \mathrm{m\ s^{-1}}$ runs. In the model runs with faster inlet current ($u_{0,c} > 1\ \mathrm{m\ s^{-1}}$) the influence of the inlet current became more dominant and formed broader shoreward sandbars. Sandbar crests formed further shoreward with increased wave height in runs with faster inlet current. All of the runs with $u_{0,c} > 1.5\ \mathrm{m\ s^{-1}}$ had double barred depth profiles, with the seaward bar becoming dominant only in the strongest wave case ($H_s = 2.5$ m). The model runs with fast inlet current ($u_{0,c} = 2$

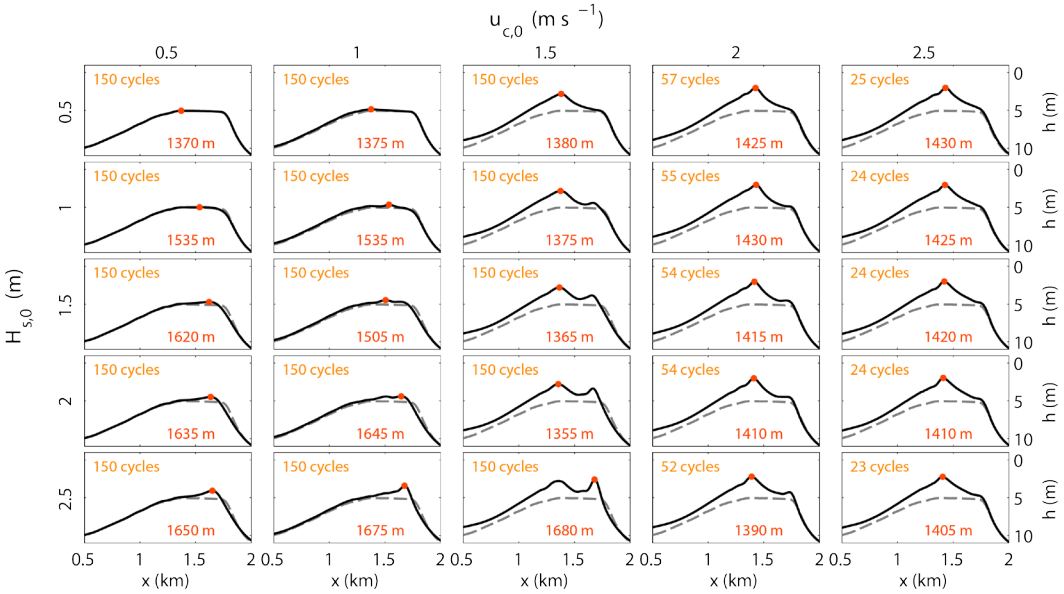

Figure 4.9. Depth profiles from 25 model runs after 150 cycles (or less if bar crest reached stopping criteria). The inlet current speed $u_{0,c}$ increases in axes toward the right and significant wave height $H_{s,0}$ increases in axes downward. In each axes, the black solid line indicates the evolved depth profile after the number of cycles (indicated in the upper left corner in orange font), and the sandbar crest is indicated with a red dot and the written below with red font. The grey dashed lines indicate the initial depth profile, which was the same in all runs.

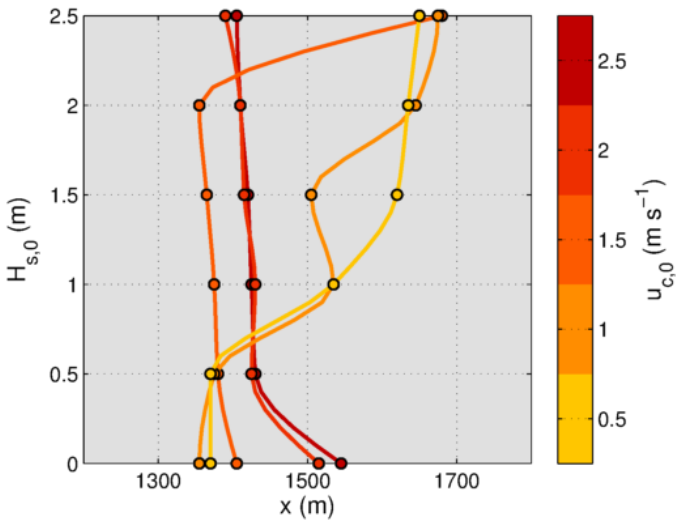

Figure 4.10. The sandbar crest positions x by significant wave height $H_{s,0}$ and inlet velocity $u_{0,c}$.

and $2.5\ \mathrm{m\ s^{-1}}$) reached the shallow depth limit before 150 cycles and have a broad dominant bar further shoreward than the rest of the ebb-shoal. Figure 4.10 shows the bar crest positions based on wave height and current strength at the boundaries.

4.4.3 Sensitivity to Initial Depth Profile

Another 6 model runs were designed and ran with the intent to test the sensitivity of short-term morphological evolution to the initial depth profile. Three different initial depth profiles, differing only by the cross-shore position of a single $1\ \mathrm{m}$ tall sandbar with an $150\ \mathrm{m}$ wide base, are shown in Figure 4.11a-c. For each of the depth profiles, two forcing scenarios were trialled: 'wave dominant' and 'jet dominant'. All six of the model runs were left to evolve until the bar crest reached 20% of the inlet depth ($2\ \mathrm{m}$).

The sandbar crest position and depth during the 6 simulations are shown in Figure 4.11d. Runs with jet dominant forcing conditions are indicated with circles, while runs with wave dominant forcing conditions are indicated with triangles. The shading of the marker symbols indicates the relative time of each simulation, with white indicating the initial position, and black indicating the final position. The simulations each required a different number of cycles to meet the ending criteria, so the shading and position of the marker symbols indicate the relative position at increments of 1/10th of the total number of cycles. The sandbar crests in all of the runs

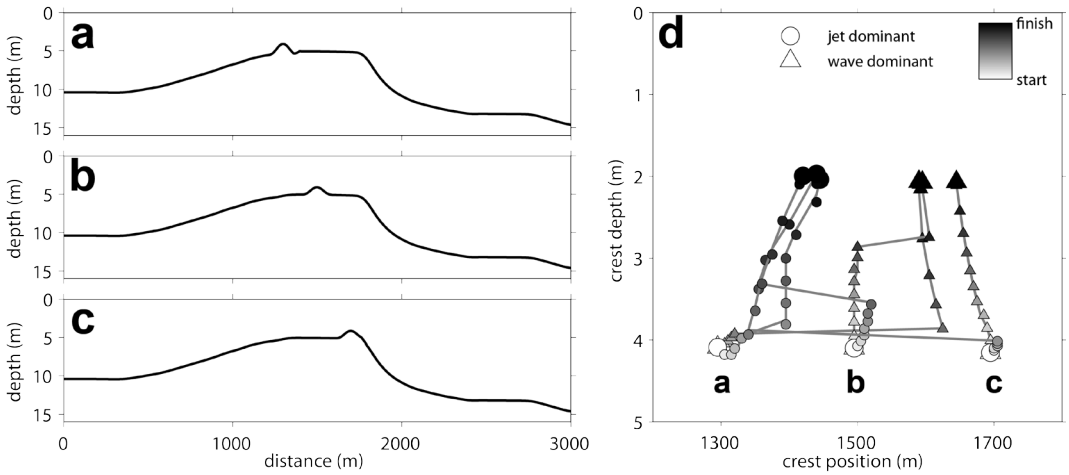

Figure 4.11. (a-c) Three different initial depth profiles, differing only by the cross-shore position of a single 1 m tall sandbar with an 150 m wide base, and (d) their subsequent evolution under forcing by jet dominant (circles) and wave dominant (triangles) conditions. The initial and final crest positions are indicated with white and black marker symbols, respectively, at increments of 1/10th of the total simulation time for each run.

with jet dominant conditions migrated to a cross-shore position within 25 m of each other. Similarly, the sandbar crests in all of the runs with wave dominant conditions migrated to a cross-shore position within nearly 50 m of each other. The crests from wave dominant conditions were over 160 m seaward from the jet dominant crest positions. In the jet dominant scenarios, depth profiles that began with the sandbar seaward of the final position (e.g. Figure 4.11b and 4.11c) initially trended seaward, but then quickly jumped shoreward as the inshore current-generated sandbar became shallower. Similar behaviour was observed for the wave dominant conditions, where the growth of the inshore bars (e.g. Figure 4.11a and 4.11b) was surpassed by the seaward wave-generated bars (Figure 4.11d).

4.5 Discussion

4.5.1 Relative Sensitivity

Of all of the parameters tested in this study, the effect of waves has the greatest impact on the development of ebb-shoal and channel morphology. The shoreward radiation stress induced by breaking waves slows the ebb-jet currents which is added to the shoreward Stokes drift (which was not included in the hydrodynamics, but in the sediment transport formulation).

Both of these combined to increase sediment flux convergence. Ebb-jet current speed at the inlet also greatly impacted the morphology. Faster currents transport more sediment and increase bed shear-stress and turbulent mixing, which results in stronger sediment flux convergence than with slow currents. Sediment characteristics were less significant to controlling morphological change, with median grain size and grain material density being the most significant of the sediment characteristics to impact morphology.

The general multiplicative factor, ξ that governs the power of sediment transport increased when mean-flow and wave orbital velocities are above the critical velocity threshold (Equation 4.10). This explains why the rate of morphological development is increased dramatically by an increase in ebb-jet current speed at the inlet from $u_{c,0} = 1\ \mathrm{m\ s^{-1}}$ to $u_{c,0} = 2\ \mathrm{m\ s^{-1}}$, and for every increase in wave height.

The result that correlation of ebb-shoal crest position with median grain size is positive without waves but negative with waves may seem counter-intuitive. However, this result comes from SvR formulation (Equations 4.7-4.11). The suspended load multiplier, A_{ss} (Equation 4.8) is 36 times greater for very fine sand than for very coarse sand, which leads to more transport of sediment for finer grain sizes. Furthermore, the critical velocity, u_{cr} (Equation 4.11) for sediment transport is greater for larger grain sizes, with the critical velocity of very coarse sand nearly double that of very fine sand. Increasing the critical entrainment velocity associated with larger grain sizes decreases the general multiplicative factor, ξ that governs the power of sediment transport (Equation 4.10). Therefore, more sediment is introduced through the inlet and deposited during the slowing of the mean-flow during the scenarios with finer grained sediments. The multiplicative factor is increased with waves through wave orbital velocity, which counteracts some of the increased transport capabilities associated with finer grains, and leads to a slight negative dependence of ebb-shoal crest position on sediment median grain size with waves.

The negative correlation between ebb-shoal crest position and grain material density is due the dependence of the dimensionless grain diameter, D_* on relative density, and D_* is in the denominator of equations (4.6) and (4.7) for the bed and suspended load multipliers. There is no dependence on density that impacts the effectiveness of waves, so the slight variations between runs 21 and 22 and runs 23 and 24 in Figure 4.5b are likely due to the variation in the rate of development and the rate of bed level change between cycles.

Negative correlation between morphological development time and grain size distribution is due to decreased critical velocity for larger distributions in Equation 4.10, which directly decreases the general multiplicative factor that governs the power of sediment transport.

Bed porosity is only accounted for when updating morphology (Equation 4.11), where it is in the denominator as $\Delta h/\Delta t \propto 1/(1-v_p)$, increasing the rate of change as the bed gets more porous.

4.5.2 Sources of Uncertainty

A major source of uncertainty in my model of the development of ebb-tidal deltas is the parameterization of a channelization scheme. We do not understand the key controls on the interaction between levees and the ebb-shoal, or the way they determine how the delta morphology develops. Levees and the ebb-shoal are strongly connected by some mechanism for lateral transfer of momentum and sediment that is not well represented in this model. Delta morphology and the position of the ebb-shoal depend on the transfer mechanism which shapes the channel (with levees) and impacts the extent and lateral spreading of the ebb-jet. Essentially a process question, this issue is beyond the scope of this paper, but is the subject of our ongoing work.

The effect of waves on the mean-flow is over represented in the ebb-jet model, which was seen to impact on the predictive capabilities of morphological development (in Section 4.3.1). Until the transfer of momentum from waves to mean-flow current can be better captured in the

jet model over shallow bathymetry, morphological predictions are likely to be quantitatively impacted by the simplified physics.

Another source of uncertainty is in parameterizing time. Morphological time is represented by cycling the flow, sediment transport, and morphological evolution steps. However how often the sediment transport model is invoked will in part determine how transient hydrodynamic behaviour is treated in the model. If the morphological update is frequent, these transient behaviours will feedback into the bed changes, and vice versa unnaturally enhancing or suppressing the feedback mechanism. Furthermore, this parameterization of time complicates the translation of model development time (in cycles) to a more meaningful time (e.g. years). At best, the timing presented in this study is qualitative.

The quantity of sediment introduced to the model domain in the set of model simulations of Section 4.4.2 is not constant between scenarios. Runs with slower ebb-jet velocity received less sediment through the inlet than did runs with faster ebb-jet velocity. However, many ebb-tidal deltas such as Raglan are composed primarily of marine sediments (*Sherwood and Nelson*, 1979) which may be delivered from either the seaward or inlet boundaries. Therefore, while the comparisons represent various quantities of sediment input, they show qualitatively the relative impacts of the various forcing conditions.

4.5.3 Role of Interplay Between Levees and Ebb-Shoal

At developmental timescales, the jet and wave forcing interact along with poorly understood lateral spreading mechanisms, upon which the formation of levees and ebb-shoals are dependent. Making the assumption that changes to the alongshore channel width occur at a slower timescale than the cross-shore changes to the ebb-shoal, short-term responses are made assuming a fixed channel width.

In situations where ebb-shoal and channel morphology have already been developed, we have shown that the short-term response of the depth profile is sensitive to the channel width. Wider channels allow for the

momentum of an ebb-jet to spread wider reducing the centreline current velocity. When ebb-current speeds from the inlet are high, the jet capacity is high. Decreases in centreline velocity along the channel therefore drive a strong accretion response. This effect is less in narrow channels.

4.5.4 Dual Influence in Short-Term Bar Formation

The relative influence of fast current speeds at the inlet was greater than the influence of strong waves on the depth profiles. When forced with relatively strong ebb-jet currents, the depth profiles experienced broad and rapid accretion shoreward of established ebb-shoals and of any wave-generated sandbars. It is likely that if flood-tide events were included in the simulations that the accretion in the channel and region inshore of the ebb-shoal would be less, because flood-tide currents increase shoreward near the inlet causing a divergent flux in sediment transport. The counteracting effect of flood-tidal current would be much less on the ebb-shoal because it is less channelized due to its shallow depth. Because of this, it is likely that a double-barred ebb-shoal would exist in more conditions than observed during model testing. For example, double bars were regularly observed to be roughly $200\ \mathrm{m}$ apart at Raglan and called the central terminal lobe and mouth bar (Chapter 2, Figure 2.9a). In those observations, the mouth bar (shoreward bar of the double bar ebb-shoal) was measured to be shallower than the central terminal lobe on two occasions (e.g. multibeam hydrographic survey, Appendix A and during ADCP survey, Appendix C), but not necessarily always true. Perhaps during wave dominated conditions, the central terminal lobe becomes the dominant shallow feature.

4.5.5 Long-Term Equilibrium as Attractors

The result that various initial depth profiles migrated towards similar positions based on the forcing conditions has many implications. It suggests that there must be stable equilibrium depth profiles for the morphodynamic ebb-jet / ebb-shoal system. It is possible that if some sort of system equilibrium does exist, that it is inherent to the model formulation, as we have effectively created a damped, forced nonlinear

system. But, do equilibrium depth profiles also exist in the natural ebb-tidal delta systems? Answering that in the field would be difficult as it would require consistent forcing conditions over timescales long enough for the morphology to approach equilibrium, and multiple times for a series of initial depth profiles. It would be possible to investigate this question further with a scaled physical model in the lab.

4.5.6 Future Work

Similarly to most morphological models for sandy coastal systems (e.g. *Lesser et al.,* 2004), the procedure presented here does not include non-local sediment transport. We assume that suspended sediment is in vertical equilibrium and that the vertical suspended sediment profile reflects a local balance between turbulence and settling velocity. In other words, the settling lag is smaller than the spatial grid structure of the model. Natural ebb-jet currents are likely strong enough to advect suspended sediment over hundreds of meters until hydrodynamic conditions no longer facilitate suspension (e.g. *Nowacki et al.*, 2012). For instance, a sediment grain with fall velocity $\omega_s = 0.04\ \mathrm{m\ s^{-1}}$ suspended in a current moving at $2\ \mathrm{m\ s^{-1}}$ will travel $500\ \mathrm{m}$ ($\gg dx = 5\ \mathrm{m}$) with the current in the time, $250\ \mathrm{s}$ ($< \Delta t = 300\ \mathrm{s}$) that it takes to fall $10\ \mathrm{m}$ vertically. If the non-local transport assumption proves not to be justified, then an extra module would need to be included where the advection-diffusion equations governing the sediment concentration profile at each time step would be calculated (such as occurs in models that have been developed for mud-transport within estuaries).

In all runs presented here, the forcing conditions applied at the boundaries were held constant for the full duration of the morphological development. In nature, ebb-jet current strength will vary with tidal and runoff conditions and waves will vary with weather conditions. The morphology and rate of development will certainly be sensitive to the nature of variations in forcing conditions. Further investigations should be done to identify the impact to delta morphology from variation in the intensity, frequency, and duration of

forcing events. Including the effects of flood-tides on the depth-profile evolution is also recommended.

The SvR sediment transport formulation and morphological updating scheme assume an unlimited sediment supply, and therefore the results presented here are transport-limited. In many coastal regions, finite sediment supply limits sediment flux and evolution of morphology. Future studies could attempt to identify how supply-limited variation impacts the development of ebb-tidal delta morphology.

As presented here, the morphological model considers only one pathway of sediment bypassing – into and out of the inlet. It does not consider alongshore transport of any kind. Alongshore sediment bypassing is a major process occurring at ebb-tidal deltas, and in many locations the primary supplier of sediment to the delta (e.g. *Hicks et al.*, 1999). Others have had success modelling ebb-tidal shoal evolution in regions with high rates of alongshore bypassing using reservoir-type schemes (*Kraus*, 2000). Future efforts could incorporate similar ideas to address alongshore bypassing.

4.6 Conclusions

An exploratory morphodynamic model was used to show the sensitivity of ebb-tidal delta channel and ebb-shoal morphology development to ebb-jet strength, waves, and sediment characteristics. The model was able to reasonably predict the ebb-shoal and channel morphology observed in the field, building confidence in the procedure used to develop natural depth profiles. Thirty-six model runs were used to identify the order of significance of parameters impacting the position of the ebb-shoal bar crest and the rate of development. Currents above a threshold velocity increased the rate of bar growth, and were further enhanced by waves. Waves also increased channel width and shortened distances from inlet to bar crest. Median grain size and grain material density of sediment slightly impacted the ebb-shoal crest position. All sediment characteristics impacted the rate of morphological development, from greatest to least

being median grain size, grain material density, bed porosity, and grain size distribution.

The parameterization of the effect of channelization on the jet outflow in the model enabled the reduction of spatial dimensions, but was identified as a major source of uncertainty and raises questions about the natural mechanisms for lateral transfer of sediment between the ebb-shoal bar crest and channel margin linear bars.

Further tests were done under the assumption that cross-shore sediment fluxes in line with the ebb-jet occur at a faster timescale than adjustments to the alongshore channel width. Short-term responses of the depth-profile were found to be sensitive to the channel width, with channel width affecting the position and rate of sandbar migration along the ebb-shoal differently between jet-dominant and wave-dominant conditions. Short-term responses to depth profiles were strongly influenced by ebb-jet current speeds at or greater than $1.5\ \mathrm{m\ s^{-1}}$. Waves tended to decrease the seaward extent of jet-influenced bar migration, but also increased the growth of sandbars positioned on the seaward end of the ebb-shoal. Stronger jet currents have greater capacity and lead to greater accretion as the jet slows than caused by wave events. Current-driven sandbar formations were much broader than wave-driven sandbar formations. The migration of sandbars originating at different locations along an established ebb-shoal all trended toward specific positions dependent upon forcing conditions, implying the existence of equilibrium depth profiles.

Chapter 5

General Conclusions

5.1 Review

With this study, I set out to learn more about ebb-tidal delta morphodynamics in order to support the idea that ebb-tidal delta morphology forms as a result of dynamic balance between the dominant forces responsible for sediment transport (ebbing tidal currents and waves). To do so, I used video-based techniques to observe geomorphic ebb-tidal delta features and related the observed movements to seasonal and interannual forcing trends. A model describing the speed and extent of ebb-jet currents was developed based on the balance of momentum from fundamental first-order physical processes, extending previous work from the literature by including the presence of breaking waves. The ebb-jet model was then coupled to sediment transport formulae to form an exploratory type morphological model for ebb-shoal and channel morphology. The exploratory tool was used to test the sensitivity of ebb-shoal and channel development to changes in forcing conditions and short-term morphodynamic response to forcing conditions, sediment characteristics, and bathymetric properties, revealing their relative significance to delta morphology. Further, I proposed that observing detailed geomorphic changes at the Raglan Bar and using fundamental physics-based exploratory models would be useful for improving our understanding of ebb-tidal delta morphodynamics.

Indeed, the approach taken in this thesis was useful to improve understanding of ebb-tidal delta morphodynamics. See Figure 5.1 for a visual summary.

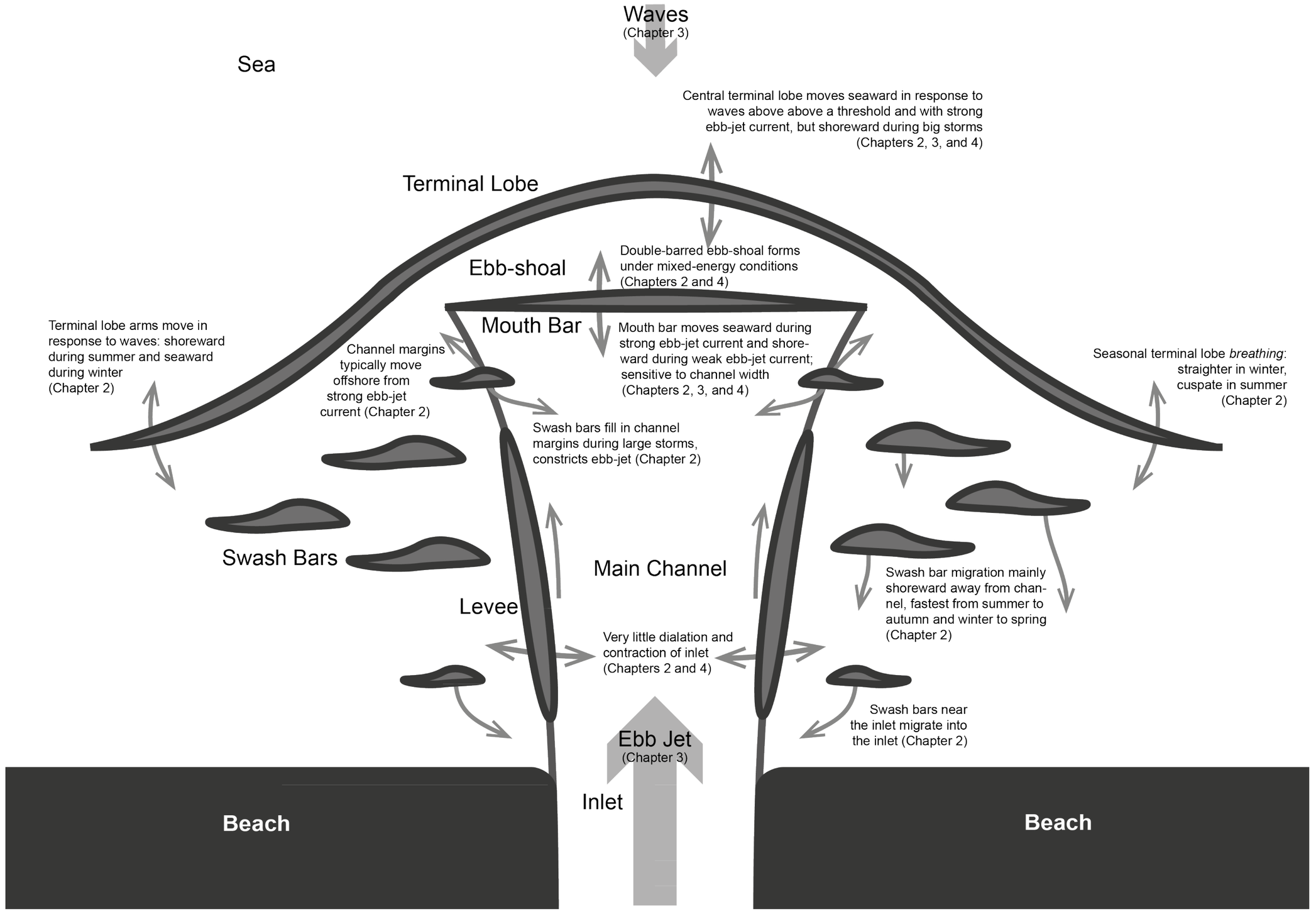

Figure 5.1. Schematic of key findings from this study about the morphodynamics of ebb-tidal deltas.

5.2 Key Findings

5.2.1 Proof of Concept

There were two techniques which were adapted in a novel way to study the dynamics of the ebb shoal. Using the Raglan Cam-Era video-observational dataset to measure the position and movement of geomorphic features in response to environmental forcing provided evidence from the field of characteristic morphology and behaviour. The development of exploratory tools, namely a semi-analytical ebb-jet model to describe ebb-jet currents in the presence of breaking waves and a coupled sediment transport and morphological evolution model were able to provide insight to the interaction of wave and tidal current forces, their competition for dominance, and sensitivity of morphological response to the environmental forcing, sediment characteristics, and bathymetric influence.

Using depth-limited wave-breaking patterns as a proxy for the position of shallow sandbars, video-based remote-sensing proved to be a useful method to capture the position of geomorphic features of the ebb-tidal delta at Raglan. Video methods are already proven useful for beach morphodynamics and have been used for few short-term deployments at ebb-tidal deltas, but this is the first long record of continuous sampling at an ebb-tidal delta like that at Raglan. Observations were frequent over the 5 year duration and were collected in conditions that would not be possible by boat. Coupled with concurrent environmental conditions, the video record captured the dependence of ebb-tidal delta morphology on wave and jet strength. Movements of the terminal lobe, mouth bar, swash bar migration, and channel width were measurable, revealing relationships and connectivity between the various features. The video method described in Chapter 2 is a plausible solution for the wider need of better geomorphic data to further our understanding about (sub-decadal timescale) morphodynamics and guide the realistic development of numerical morphodynamic models.

The development of simplified modelling tools based on fundamental first-order physical processes was also helpful in exploring the interactions and relationships responsible for determining ebb-shoal and channel morphology. The jet model revealed the influence of opposing breaking waves on ebb-jet currents and jet width, along with the emergence of a point of flow convergence. Further, the contribution of wave effects to the momentum balance were shown to impact the rapid slowing of jet flow, overall extent of an ebb-jet, and increase the jet width, qualitatively in line with known jet behaviour (*Nardin and Fagherazzi* 2012; *Nardin et al*., 2013; *Olabarrietta et al*., 2014). On flat bathymetry with non-breaking waves, the model was able to reproduce ebb-jet currents from laboratory (*Ismail and Wiegel*, 1983) and numerical modelling simulations (*Nardin et al.*, 2013). By including wave-breaking-induced shoreward momentum flux in the jet model, waves above a threshold caused the jet current to stop and a convergence point to develop, which was not predicted in the numerical simulation that included wave effects only through the bed friction term.

When compared to field observations of a tidal jet at a location with well-established channel/levee features, the need to constrain jet spreading within the model was identified which led to the introduction of the channelization parameter (Equation 3.10). With the channelization parameter representing the jet constraining action of established levees, the jet model was calibrated for nine ebb-events (3 from each of 3 event classes) and validated over sixty-one ebb-events. Wave breaking parameters were determined for each ebb-event in order to reduce error associated with the wave dissipation model and more closely focus on the jet model performance. Overall, the jet model predicted the measured currents with excellent skill. The jet model skill was worst at the shallow region around the ebb-shoal where the model consistently over-predicted the influence of waves on slowing the jet current. Qualitatively, the predicted trend of increased wave-induced slowing and even the emergence of a flow convergence with increased wave energy flux matched measurements, but over predicted the effect.

In all cases, the friction coefficient in the calibrated jet model was nearly an order of magnitude larger than measured in the field or specified in numerical simulations. This result is attributed to unresolved processes being incorporated into the bed-friction term. Lacking vertical structure and a pressure gradient term precluded the accurate representation of higher-order processes known to exist at an ebb-tidal delta (like Stokes drift, wave setup, and the adjustment of sea-surface elevation). Nevertheless, the ebb-jet model was fast and effective for simulating ebb-jet currents, and coupled nicely to sediment transport formulae to form a useful exploratory morphological modelling tool.

5.2.2 Dependence on Environmental Conditions

This study highlights again a key outcome of many previous studies that the shape of ebb-tidal deltas is governed by complex interplay of waves and tidal currents (*Walton and Adams*, 1976; *Hayes*, 1980; *Hicks and Hume*, 1996). The modelling tools showed that opposing waves act to slow ebb-jet currents and increase jet spreading, effectively causing a convergence of sediment flux where competing forces meet. Under higher-energy wave forcing, ebb-shoals formed closer to the inlet and the terminal end of the main channel and was wider than morphology developed under low-energy wave forcing. This occurred because the effect of waves spread the ebb-jet and subsequently led to a wider channel. The ability of waves to develop wide channels was greatest when ebb-jet current at the inlet was slow. Faster ebb-jet current decreased the influence of waves on the development of ebb-shoal and channel morphology. However, ebb-jet current had the largest influence on rate of development – more than waves, or sediment characteristics. Sediment characteristics were hardly influential to the position of the equilibrium ebb-shoal position, but did impact the rate of development. The response rate increased dramatically with increased ebb-jet current speed and with wave height driven by the general multiplicative factor of the SvR sediment transport formulation. For example, the suspended load multiplier was 36 times greater for very fine sand than for very coarse sand, leading to greater transport of finer sands. However, the morphology dictates the

level of interaction between waves and currents, and when given ample time for development the equilibrium morphology.

5.2.3 Seasonal and Interannual Trends

The positions of the main features of the Raglan ebb-tidal delta (terminal lobe, mouth bar, and channel levee) were shown to vary in response to seasonal and interannual forcing trends about a long-term average. Generally, the low-energy restorative summer waves led to a more cuspate terminal lobe, while in the high-energy erosive winter waves straightened the terminal lobe and moved it further seaward than the mean. Movements throughout the delta were intermittent between less active periods, with the fastest swash bar migrations occurring during the transition between seasons, namely winter to spring and summer to autumn. This transitional behaviour is similar to observations of geomorphic cycles by *Oertel* (1977) where the young deltas were characterized by accretion and old deltas by erosion. In our observations at Raglan, sandbar migration and changes in the terminal lobe occurred as transitions between the seasonal cycles of delta morphology.

The exploratory morphological evolution model showed similar behaviour as the Raglan observations. Multiple (different) depth profiles trended toward the same 'attractor' profile when forced by the same conditions, with the rate of change depending on the relative difference of the initial profile from equilibrium. This finding could explain why different responses were observed for the central terminal lobe position at Raglan under similar forcing conditions over time.

Interannual patterns were observed, particularly in the cross-shore position of the ebb-shoal, distance between the central terminal lobe and mouth bar, and alongshore distance between levees (or channel width). Potential causes of non-seasonal behaviour could be interannual trends in forcing conditions (e.g. related to ENSO or PDO) or possibly related to pulses of sediment supply that enter from around the headland (as in *Phillips*, 2004). Interannual trends in morphology were not investigated in this study because the record considered was only 5 years long, shorter

than would be useful for relating to various climatic oscillation cycles and we lacked information about available sediment supply. It is possible that the morphological system was highly sensitive to initial conditions and that the system may have self-organised into the observed interannual behaviour as do many other morphological systems.

5.2.4 Double-Barred Ebb-Shoal

The observation of two separate bar features on the ebb-shoal at the seaward end of the main channel, the central terminal lobe and the mouth bar has not been described before. The double-barred ebb-shoal was seen in the multibeam data (Figure 2.1c; Appendix A), common in the video data (Figure 2.9a), and also occurred in the exploratory model sensitivity testing as a solution to mixed wave and jet dominant conditions (Figure 4.9). In the video observations, the distance of the central terminal lobe (or seaward bar of the double-barred ebb-shoal) from the inlet was weakly positively correlated to the wave power and tidal range (a proxy for ebb-jet current speed at the inlet), while the distance from the inlet of the mouth bar (or inner bar of the double-barred ebb-shoal) more strongly positively correlated to tidal range. Again, the morphological model showed similar results, where the seaward bar grew faster and further seaward with increasing wave height, but only in situations where the inlet current was relatively slow. The inner bar grew faster with increasing ebb-jet speed at the inlet, an effect that decreased with wave height. For cases with medium to fast ebb-jet current speed at the inlet, the inner bar formed quicker and further shoreward with increased wave height. The model results suggest competing influences of the waves, which act to compress the ebb-jet currents driving a convergence in flow and sediment inshore and the strong shoreward excess flux of momentum generated as the larger waves break at terminal lobe, which is less dominant when ebb-jet currents are strong enough to initiate wave dissipation offshore of the terminal lobe. This competition could explain why the correlations of the cross-shore position of the ebb-shoal bars in the video data were not strongly related to any single variable. The occurrence of double-barred

ebb-shoals is a nice example of the type of complicated interactions and competing processes that occur at ebb-tidal deltas.

5.2.5 Interplay Between the Ebb-Shoal and Channel Margins

In the morphological model unknown details about how sediment is transferred laterally at an ebb-shoal contributed to a major source of uncertainty. The assumption that alongshore levee position (i.e. channel width) moves more slowly than cross-shore fluxes along the ebb-shoal led to the assumption that details about the lateral transfer of sediment could be avoided by holding the channel width fixed during short-term simulations. Using this assumption, I found that the width of the channel impacted the effects of waves on ebb-shoal response. With a wide channel, waves were effective at compressing the extent of the ebb-jet and therefore causing accretion further inshore, which did not happen in the case with a narrow channel. The weak correlations of ebb-shoal position to wave power and tidal range in the video data hint that the response of the ebb-shoal is different depending on something not included in the comparison. Watching video observations (as an animation) of the ebb-shoal and channel margins at Raglan, sometimes large storm events would cause sandbars to form inshore from the terminal lobe and inward toward the ebb-jet, effectively narrowing the seaward end of the main channel. The formation of sandbars along the channel margins originating from cross-shore fluxes makes it difficult to see any relationship between the cross-shore ebb-shoal position and the width of the channel in the video data. This type of behaviour is not included in the morphological model. However, the mechanism does provide justification for a levee contraction term in the model, dependent on waves, and could alleviate the need for a static, pre-existing channel.

5.3 Suggestions for Future Research

5.3.1 Exploratory Models

The ebb-jet model would likely benefit from the introduction of a pressure gradient. In the formulation presented in Chapter 3, the jet spreading term

$\partial b/\partial x$ acts like a pressure gradient term, except in the case when the jet is confined by levees. However, in theory by including a proper pressure gradient term, it would be easier to specify lateral fluxes and therefore include the ability to build levees in the morphological model. I am interested to see how the experiment results would differ with the inclusion of a pressure gradient term from those presented in this research.

I would like to determine mechanisms for lateral transfer of momentum and channel spreading. This is a fundamental issue and would help the progression of simplistic models like the morphological model presented in Chapter 4.

The introduction of a wave-breaking-dependent turbulence term (like in *Zippel et al.*, 2015) into the jet-model would allow for better tuning of turbulent mixing along the length of the ebb-jet, and would likely improve the over prediction of wave effects on ebb-jet flow at the ebb-shoal and seaward.

Many simple sediment transport models do not include the ability for advection of suspended material beyond neighbouring cells (e.g. *van Rijn et al.*, 2001). This ability is essential when modelling the transport of mud (e.g. *Whitehouse et al.*, 2000) and might be relevant at ebb-tidal deltas where sediment is much finer than the ebb-jet competence (e.g. *Nowacki et al.*, 2012). I would like to modify the sediment transport formulation in the morphological model to include advection of suspended material to distant cells based on current thresholds for sediment to fall out of suspension, and local suspended sediment concentration. Then we could examine the difference between local-advection and non-local advection on morphological development of ebb-shoal and channel morphology.

5.3.2 Raglan Cam-Era Dataset

The Raglan Cam-Era video record is extensive and detailed, and is probably the best observational dataset in existence of the morphodynamics of an ebb-tidal delta. This thesis only surficially explores

this exceptional dataset, using less than 1% of image pairs in the 5 year period of interest.

The image field of view covers not only the delta, but also Ngarunui Beach. Sandbars are clearly visible migrating onshore and merging into the beach during certain times. At other times the formation of shoreline irregularities (e.g. rip-current channels) form and can be seen migrating northward along the beach nearshore. It would be worthwhile to link periods of beach accretion and erosion to the activity at the ebb-tidal delta. For example, does the shoreward migration of the terminal lobe arms correspond to times of beach erosion or accretion? What are the mechanisms for sediment exchange and storage between the beach and delta? Do certain ebb-tidal delta morphologies lead to the increased occurrence of rip currents on Ngarunui Beach?

I would like to use the video data to track individual sequences of morphological progression, and use a sequence or more to calibrate and validate the predictive abilities of 1) the morphological model presented in this thesis, and 2) a detailed process-based numerical morphodynamic model, like Delft3D.

It is worthwhile to document evidence for the idea that channel margins (at least sometimes) push inward (laterally and shoreward) toward the jet during storm events rather than landward. This would entail examining the video record for multiple examples of different morphodynamic responses to similar wave events based on the width of the channel at the time of event.

In the long term, I envisage a regional sediment transport model that includes the Raglan Bar, the adjacent beaches, headland, and nearby coastline using a detailed process-based numerical morphological model. The model would be coupled with video observations of the Raglan ebb-tidal delta. Video data could be used to guide development and calibration / validation of events. The model would be able to resolve fluxes moving into the local embayment from around the headland and resolve local

circulation cells of flow and fluxes throughout the delta and along the adjacent coastline. It would be able to predict the relative rate of transfer and storage in each of these connected systems. Predictions of sediment fluxes around the headland would be useful for estimating sediment supply and delivery to the ebb-tidal delta, which could be compared to interannual variation in the position of geomorphic features at the delta in order to gauge the significance of sediment supply variation to delta morphology.

It is worthwhile to develop an iterative refinement process for the Raglan Cam-Era system to estimate the Raglan ebb-tidal delta bathymetry based on comparisons between video-derived wave dissipation and numerical model results (similar to *van Dongeran et al*., 2008). The procedure/software could be used to provide near real-time bathymetric updates to Coastguard and other boats requiring safe passage through the delta. Also, the technique could be adapted to other ebb-tidal deltas with video observation equipment.

5.4 **Summary**

In summary, the work presented here adapted two techniques in a novel way to study the dynamics of ebb-tidal delta morphology. Geomorphic ebb-tidal delta features where observed with video-based techniques and their movements were related to seasonal and interannual forcing trends. A semi-analytical ebb-jet model describing the speed and extent of ebb-jet currents was developed based on the balance of momentum from fundamental first-order physical processes and included the presence of breaking waves. The ebb-jet model was then coupled to sediment transport formulae to form an exploratory type morphological model for ebb-shoal and channel morphology. The results and implications from this approach helped improve our understanding of ebb-tidal delta morphodynamics, and support the idea that ebb-tidal delta morphology forms as a result of dynamic balance between the ebbing tidal currents and waves.

Appendix A

Raglan Hydrographic Data

DML survey vessel *Discovery II* preparing for launch at the Raglan Wharf, 18th November 2013.

A.1 Introduction

Bathymetry data was gathered and used to generate a bathymetric surface map of Whaingaroa (Raglan) Harbour (*Harrison and Hunt*, 2014). Bathymetry data was used in this study for a number of applications such as investigating ebb-jet structure, observations of ebb-tidal delta morphology, and validation of video rectification process. The data was also used by fellow PhD student Steve Hunt to generate a numerical model domain in Delft3D. Additionally, University of Waikato promotional posters were created using the bathymetry data overlain on aerial photography (*WRAPS*, 2012) and were distributed as A2-sized posters to local groups (e.g. Raglan Volunteer Coastguard, Trust Waikato Raglan Surf Life Saving Club, and Raglan Area School) with hopes to foster active relationships between those groups and the University of Waikato Coastal Marine Group. Approximately 150 A4-sized maps (Figure 1) were distributed to conference participants at the New Zealand Coastal Society's 22nd Annual Conference ('NZCS 2014') in Raglan.

A.2 Description of Data and Map Composition

Bathymetric data for the Whaingaroa Harbour map comes from multiple sources, coverage areas, and surveys, which was combined into a single composite surface. The composite is composed of boat-mounted multibeam echo-sounder ('MBES') surveys, aerial Laser illuminated Detection And Ranging ('LiDAR') surveys, jet ski-mounted singlebeam echo-sounder ('SBEM') surveys, and digitization of navigational charts and orthophotos. Where ever possible the highest accuracy, finest resolution, and most recently acquired data were used.

The most recent survey was conducted by Discovery Marine Limited ('DML') commissioned by the University of Waikato and Waikato Regional Council specifically for this PhD research, consisting of boat-mounted MBES measurements of the ebb-tidal delta and main channels of the inner harbour taken during 18-20 November 2013. The DML data was initially processed for boat movement (e.g. heave, roll, etc.), sound conductivity through water, and water level variation by DML, extracted to a 1 m

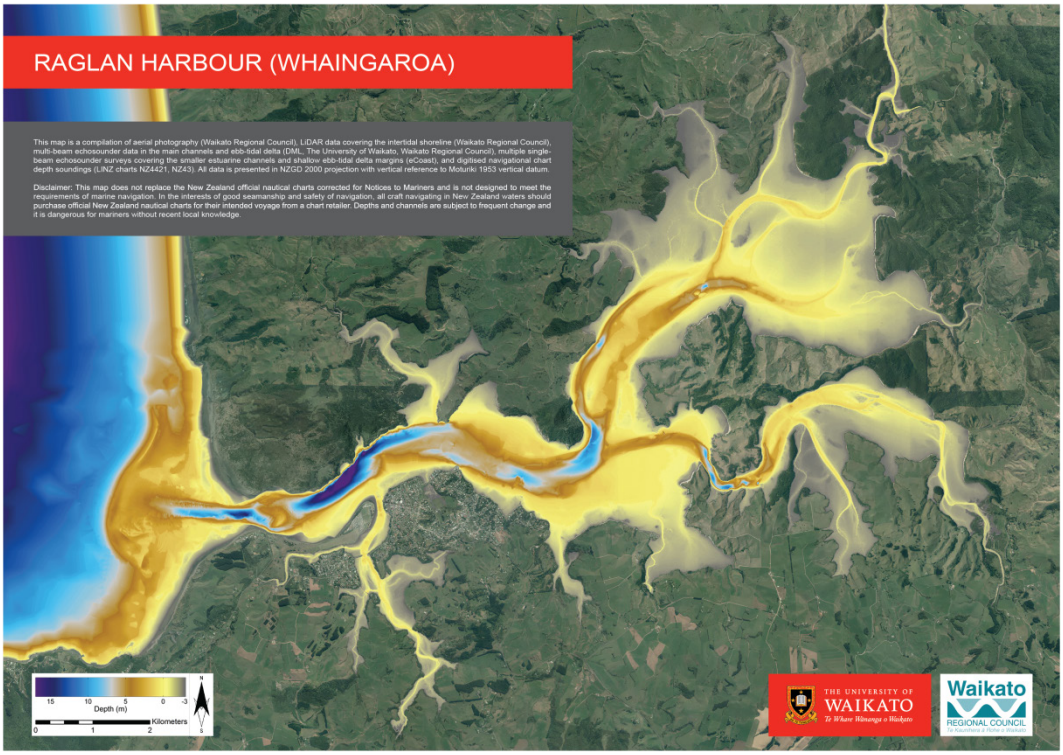

Figure A.1. Whaingaroa Harbour map (A4-size) showing the depths of the harbour and entrance. Bathymetric information is overlain on WRAPS 2012 aerial photography GIS layer.

sampling size and provided to University of Waikato as an ASCII text file of 5,506,835 points (i.e. northings, eastings, and elevations). The DML MBES data is provided in NZGD 2000 Mount Eden Circuit projection coordinate system, with vertical reference to Moturiki 1953 vertical datum.

The next most recent data set covers the intertidal zone and was derived from the aerial LiDAR survey from 2010/2011 of the entire Waikato Region (*WRC*, 2011), commissioned and owned by the Waikato Regional Council. The data was made available for this research through a licence agreement between the Waikato Regional Council, University of Waikato, and Shawn R. Harrison (the author).

LiDAR data has full coverage within the Harbour intertidal zones and shoreline, with horizontal accuracy of ± 0.5 m and vertical accuracy of ± 0.15 m. The data was originally provided by WRC as an ESRI ASCII GRD at 1.0 m grid resolution, but was resampled to 10 m due to computer memory constraints. The WRC LiDAR data is provided in NZTM2000

Table A.1. Description of bathymetric data sources used in the generation of a composite bathymetry map. The sources are listed in order of preference from most to least.

Source	Date of measurements	Initial coordinate system	Horizontal resolution	Primary coverage
DML MBES Survey	18-20 Nov 2013	NZGD2000 Mount Eden Circuit, Moturiki 1953	1 m	Ebb-tidal delta, main channels
WRC LiDAR Survey	2010/2011	NZTM2000, Moturiki 1953	10 m	Intertidal zones, shorelines, beaches
ASR SBES Bar Survey	Jan 2009	WGS1984, local chart datum	~40 m	Ebb-tidal delta, delta flanks
ASR SBES Upper Estuary Survey	Dec 2008	WGS1984, local chart datum	~40 m	Upper estuary main channels
LINZ Chart NZ4421	1977, 1961	WGS1984, local chart datum	100 m	Inner-shelf

projected coordinate system with vertical reference to Moturiki 1953 vertical datum.

In the regions lacking coverage by the MBES and LiDAR data, older data was used. A jet-ski-mounted SBES survey was conducted during January 2009 by ASR Ltd (and the author) of the ebb-tidal delta. The coverage of

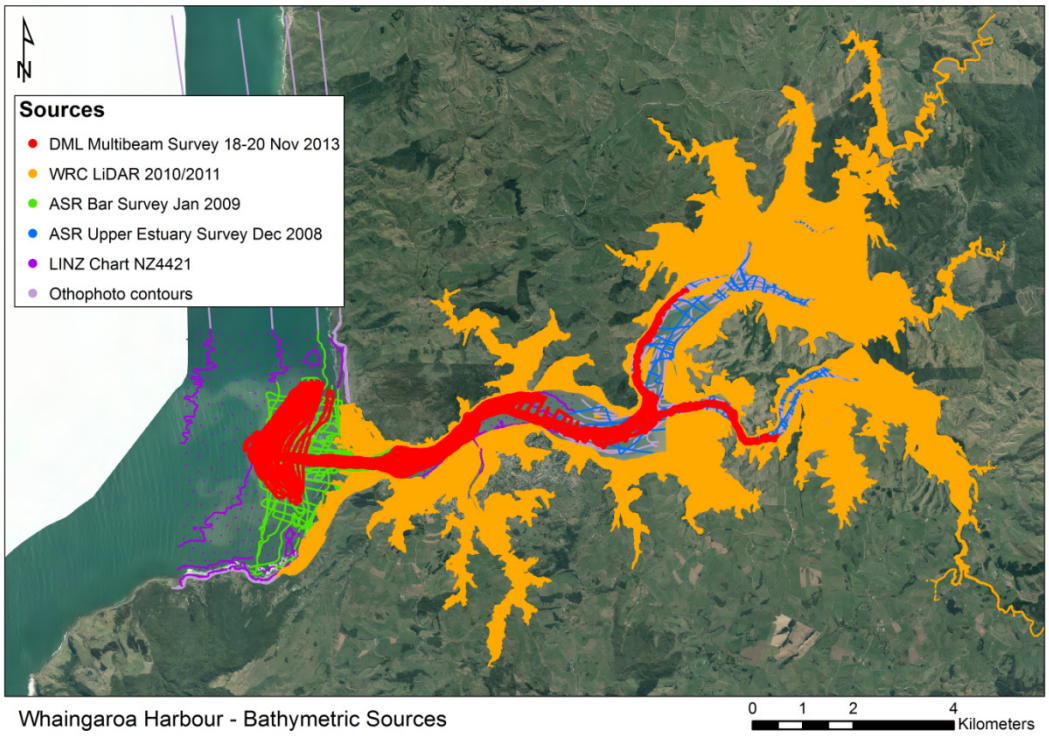

Figure A.2. Sources of bathymetric data used to make the composite map. The locations of bathymetry data points are overlain on WRAPS 2012 aerial photography GIS layer.

Figure A.3. DML survey boat *Discovery II* collecting MBES depth measurements at the ebb-tidal delta and main channels of Whaingaroa Harbour. DML surveyors were joined by Shawn Harrison and Dean Sandwell on 18-20th November 2013.

the SBES ebb-tidal delta survey was broad but not fine, unable to capture the level of detail of bedforms observed in the MBES data. Another jet-ski-mounted SBES survey was conducted in the channels of the upper estuary during December 2008 by ASR Ltd. The data was generously made available to this PhD research by ASR Ltd through a verbal agreement. The data was provided in WGS1984 geographic coordinates with vertical reference to local chart datum.

Regions still lacking coverage were supplemented by digitizing depth soundings and contour lines from published Land Information New Zealand ('LINZ') navigation chart NZ4421 (*LINZ*, 2010). The depth soundings on the NZ4421 were actually measured on voyages by HMNZS Takapu & Tarapunga during 1977 and 1961. Although old, the data was mainly used in the inner-shelf seaward of the ebb-tidal delta. NZ 4421 does not cover any of the upper harbour, so contours were digitized of channels, and intertidal platform features from an OrthoPhoto. These points are the least represented and least preferred. All digitized material originated in WGS1984 geographic coordinates with vertical reference to local chart datum.

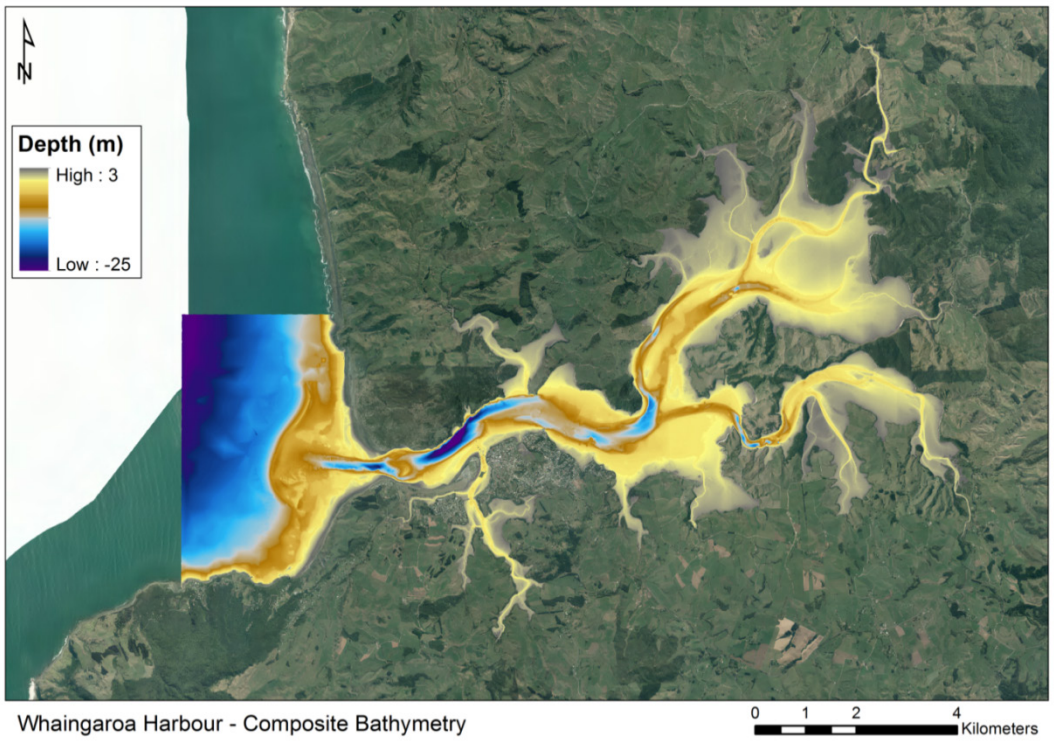

Figure A.4. The composite bathymetry surface resulting from combining the multiple data sources, generating a TIN, and extracting to a 1 m raster grid. Bathymetry data is overlain on WRAPS 2012 aerial photography GIS layer.

The local chart datum is approximately lowest astronomical tide (LAT), which is 5.06 m below Benchmark AGE6 (located next to the Raglan Wharf boat ramp). Moturiki 1953 mean sea level is 3.4605 m below Benchmark AGE6, which means that local chart datum is 1.60 m below Moturiki 1953 vertical datum.

All of the data points were combined in ESRI ArcGIS, arranged in order of preference so that most recent data sources supersede older data where coverage overlapped, and interpolated in to TIN surface model. The TIN was then output to a raster grid at whatever spatial resolution required by the individual needs. For example, 1 m raster grid was extracted to generate the Whaingaroa Harbour map, but a 40 m raster grid was extracted for generating a numerical model domain.

Appendix B

Sediments at Raglan

Black sand dunes at the beach on the northern side of the entrance to Whaingaroa Harbour at Raglan, New Zealand.

B.1 Introduction

Sediment characteristics are significant in determining the ability of waves and currents to transport sand grains (e.g. Chapter 4). More information about the local sediment at Raglan was desired, namely sediment grain size and material grain density for modelling purposes.

Two sediment sample sets were available for analysis of sediment grain size and material density. Firoz Badesab and Christian Winter provided sediment samples from Raglan. Samples were analysed for sediment grain size by laser diffraction and with sieves, and for material density by helium gas pycnometer. An overview showing the locations where sediment was sampled is shown in Figure B.1.

Two different sediment samples were later available for viewing under a scanning electron microscope. During a visit on 8th April 2013 to the Taharoa ironsands mine (operated by Bluescope Steel), I was given a jar of titanomagnetite that had been mined from the aeolian dunes at Taharoa. Another jar of titanomagetite from Ruapuke Beach was provided

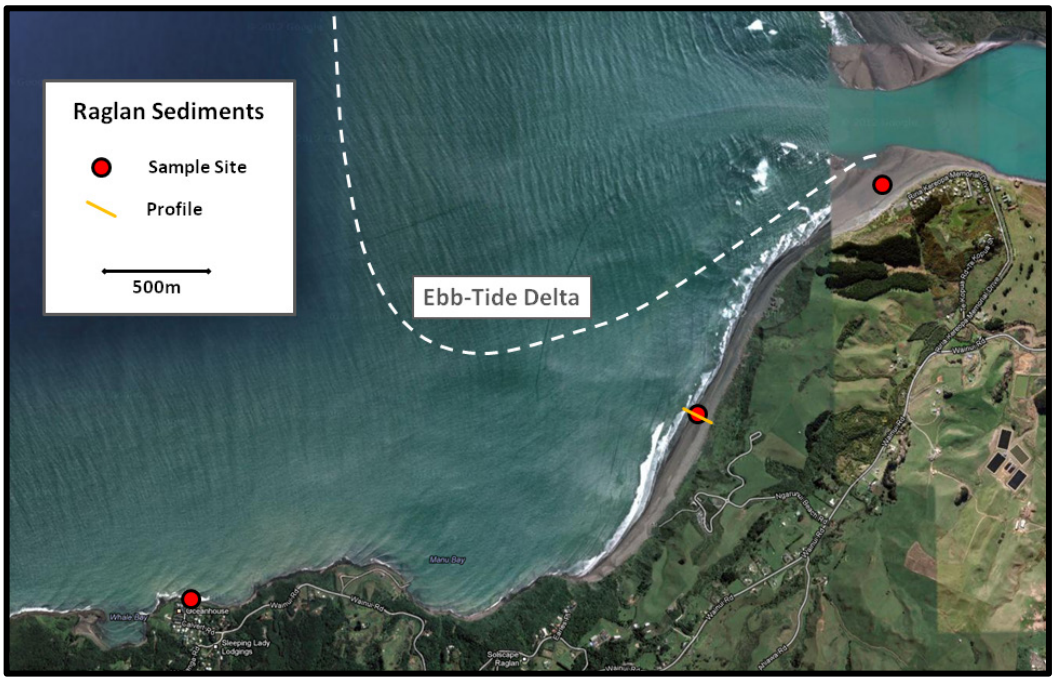

Figure B.1. Overview showing the locations of the sediment samples near Raglan. From bottom left to top right the sample sites are called “Whale Bay”, “Ngarunui Beach”, and “Wainamu Beach”.

by Ruggero Capperucci in September 2011. Both of these samples consisted of fine black sand and looked very uniform in grain size to the naked eye. The Ruapuke sample appeared blacker than the Taharoa sample. With free access to a scanning electron microscope, I took the opportunity to look more closely at these rich black sand samples. Ruapuke Beach sand looked very similar to the dark fractions of sand at Wainamu Beach in size, colour, and texture.

The description of these sediments and my findings are presented below.

B.2 Grain Size and Material Density

The sediment samples used to determine grain sizes and material density came from two contributing parties. Firoz Badesab and Roger Briggs conducted sediment sampling along an $150\ \mathrm{m}$ cross-shore transect at

Figure B.2. Sediment sampling transect on Ngarunui Beach, Raglan, NZ. Samples were taken along a 150 m cross-shore transect at 10m intervals from the toe of the dune into the intertidal beach near low tide on 1 March 2012 by Firoz Badesab and Roger Briggs.

Figure B.3 Sediment was sampled at (a) Whale Bay during low tide from in between boulders (b), and at (c) Wainamu Beach. Provided by Christian Winter.

Ngarunui Beach from the toe of the dune into the intertidal beach near low tide at $10\ \mathrm{m}$ intervals on 1st March 2012 (Figure B.2). These samples were analysed for sediment grain size using laser diffraction. The density of the material was calculated using a helium gas pycnometer. The other set of samples was contributed by Christian Winter, with sediment taken from Wainamu Beach near the end of Riria Kereopa Memorial Drive and from Whale Bay behind 1 Calvert Road (Figure B.3). These samples were sieved to determine grain size. Density was determined along with the Ngarunui Beach samples using the helium gas pycnometer.

Table B.1 describes the material density and grain size of the sediment samples. In general, the sediment decreases in grain size and increases in material density from Whale Bay to Wainamu Beach. The sediment at Whale Bay consisted of small black and brown gravel with shell fragments, mostly between $[1 - 4\ \mathrm{mm}]$ with a mean grain size of $1.4\ \mathrm{mm}$. At the Ngarunui Beach transect, the largest grains occurred furthest from the dunes near the surfzone. The sediment grain size decreased and density increased with distance from the surfzone towards the dune. The Ngarunui Beach grains were dominated by fractions between $[0.15 - 0.5\ \mathrm{mm}]$ with

mean grain sizes shown in Figure B.2. The Ngarunui Beach sediment is a mixture of black and grey fine sand fractions. The samples nearer the surfzone had a larger portion of grey than those samples nearer the dunes, which were predominately black. The black sediment fractions appeared “glittery” in light. The smallest grained and most dense sediment of those sampled occurs at the Wainamu Beach site. The Wainamu Beach grains were dominated by fractions between [$0.063 – 0.25\ \mathrm{mm}$] with a mean grain size of $0.18\ \mathrm{mm}$. The Wainamu Beach sediment consisted of black, brown, grey, and blue tinted fine sand to silt fractions and was notably darker than the other sediments. The Ngarunui and Wainamu Beach sediments were strongly magnetite rich as they were observed to move quickly in presence of a magnet.

Table B.1. Density and mean grain size of the Raglan beach sediment samples.

Sample Name	Material Density (kg/m3)	Mean Grain Size (mm)
10 m	3168	0.237
40 m	2826	0.294
60 m	2729	0.227
80 m	2724	0.388
90 m	2808	0.369
110 m	2705	0.454
Wainamu Beach	3535	0.177
Whale Bay	2804	1.398

B.3 Sediments in Detail

The Ruapuke Beach and Taharoa dune sediment samples were each prepared on their own standard sample holder and then inserted into the Phenom ProX desktop scanning electron microscope. For each sample, the sediment was examined first at very low magnification to gauge the distribution of grains in the sample. The grains were very similar in size and shape to other grains in the same sample, for both samples. A single representative grain in each sample was chosen for increased magnification.

The grain morphology was different between the two samples. The Ruapuke grains were generally smaller ($100 \leq d \leq 200\mu m$) and edgier (Figure B.4a) than the Taharoa grains, which were larger ($300 \leq d \leq 400\mu m$) and rounded (Figure B.4c). The Ruapuke grains were smooth on the surface, free of debris (Figure B.4b), with some very small pitting ($< 1\mu m$) on some surfaces (not shown). In contrast, the surface of Taharoa grains appeared worn and well tumbled, with small flecks of debris collected in the runnels and hollows of the grain (Figure B.4d).

The difference in grain size could be attributed to the relative distances of each sample site to the likely source of the sediment, nearly 200 km south

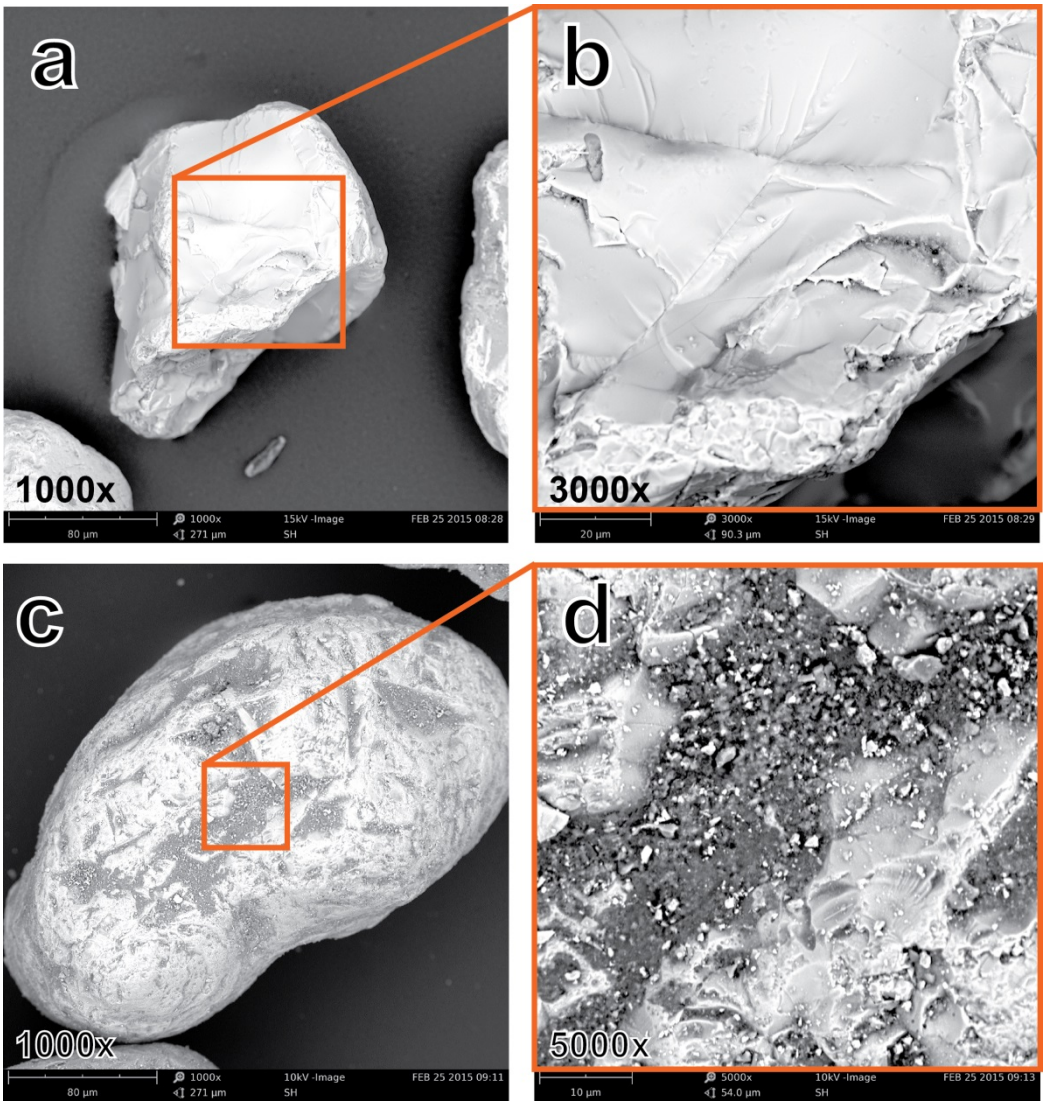

Figure B.4. Scanning electron microscope images of sand grains at (a) and (b) 1000x magnification, and at (b) 3000x and (d) 5000x from Ruapuke Beach and Taharoa dunes, respectively.

at Taranaki (see Chapter 2). Alternatively, the sediments could be from different geological periods which could explain the difference in size. The Ruapuke sand was taken from an active beach and was most likely transported through littoral processes along the coast, whereas the Taharoa sand was mined from dunes, where the grains have been covered for an unknown (but likely longer) amount of time. Also, the Taharoa sand was processed to separate the undesirable (non-titanomagnetite) which could have damaged the natural grain morphology.

The scanning electron microscope had the ability to identify elements in the grain composition. Using 'precise spot mode' at a single point on the sand grains, elements were identified and listed in Table B.2 by relative atomic concentration. Both grains had large amount of oxygen, iron, titanium and magnesium. The Ruapuke grain had bromine, which Taharoa did not. Taharoa had aluminium, manganese, silicon, and tellurium, while Ruapuke did not. Both grains types were dominated by oxygen, iron and titanium. The additional elements in the Taharoa grain may have come from the sorting process at the Taharoa ironsand mine.

Table B.2. Element identification by the Phenom scanning electron microscope in spot mode.

	Ruapuke grain	Taharoa grain
Element	Atomic concentration (%)	Atomic concentration (%)
Aluminium	-	2.1
Bromine	0.9	-
Carbon	0.8	0.9
Iron	14.5	30.6
Magnesium	2.4	1.5
Manganese	-	0.1
Oxygen	79.3	61.2
Silicon	-	1.0
Tellurium	-	0.1
Titanium	2.2	2.5

Appendix C

Raglan Ebb-Jet Measurements

University of Waikato research vessel *Taitimu* during ebb-jet measurements at Raglan, New Zealand, with *Karioi* in the background.

C.1 Introduction

The structure of ebbing tidal jets ('ebb-jets') has mainly been studied using analytical (e.g. *Özsoy and Ünlüata*, 1982) and numerical models (e.g. *Spiers et al*., 2009; *Nardin et al*., 2013), and scaled physical models in laboratory flumes (e.g. *Ismail and Wiegel*, 1983; *Rowland et al*, 2007) Few field measurements of ebb-jets exist in the literature (e.g. *Old and Vennell*, 2001; *Nowacki et al*. 2012), but no detailed measurements have been made of the ebb-jet at Raglan.

To satisfy my curiosity and learn more about the hydrodynamic forces associated with an ebbing tide at Raglan, multiple downward-pointing acoustic Doppler profiler ('ADCP') transects were surveyed along the ebb-jet longitudinal (or along-jet) axis and transverse (or cross-jet) axis between high and low tide. The description of field measurements, processed results, and implications are presented herein.

C.2 Description of Data Collection

The date of measurement 14 April 2014 was chosen mainly based on the occurrence of fine weather during a time when the boat and crew were available on the west coast. The swell conditions for the day were 'very calm' with forecasts suggesting $H_s = 0.5\ \mathrm{m}$ and $T_p = 8 \text{ to } 12\ \mathrm{s}$. During the day, we visually observed the swell drop off, as it was much smaller at 3 pm than at 10 am. The sky was overcast for the majority of the day with occasional patches of direct sunlight. Wind data was taken from the Raglan Kitesurfing Club's wind gauge located atop the toilet block at the harbour entrance The wind was from the east at $10\text{-}15\ \mathrm{knots}$ (gusts up to $17\ \mathrm{knots}$) in the morning and increased to $18\text{-}20\ \mathrm{knots}$ (gusts up to $24\ \mathrm{knots}$) during midday. By 3 pm, the wind had dropped to below $10\ \mathrm{knots}$. Since the wind was directed offshore the entire day, there was very little (wind associated) chop ($O(5\mathrm{cm})$). The predicted tidal difference between high and low was $2.9\ \mathrm{m}$, roughly the mean spring tidal range. The actual observed water levels at the Raglan Wharf (provided by Waikato Regional

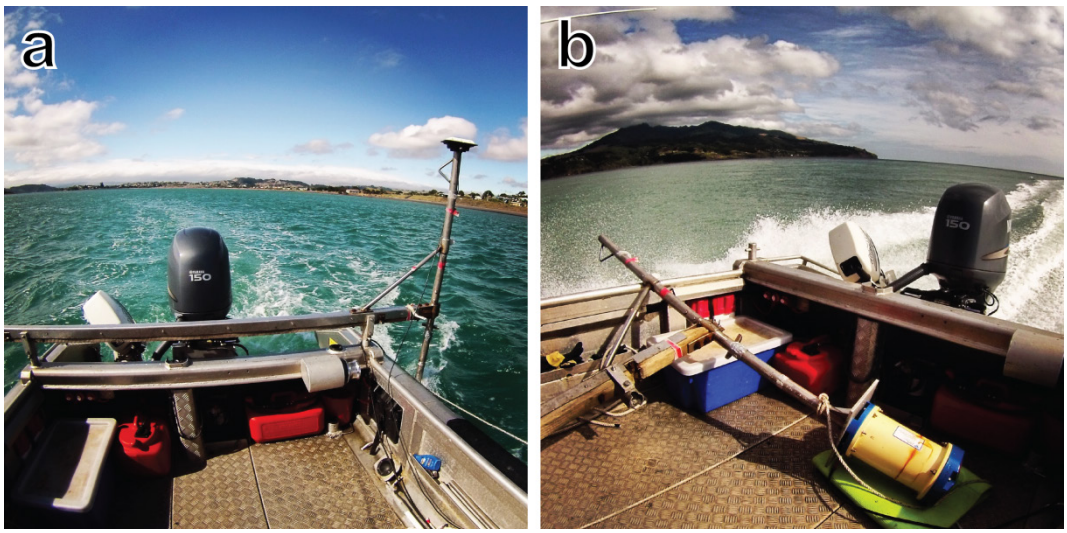

Figure C.1. Downward-pointing ADCP (a) deployed off the port quarter of *Taitimu*, and (b) shown mounted to the bottom of pole and removable boom assembly when travelling at high-speed against the ebb-jet current.

Council) was $1.39\ \mathrm{m}$ (above msl) at high-tide and $-1.35\ \mathrm{m}$ (below msl) at low tide ($2.74\ \mathrm{m}$ range).

To access the region between inlet of Whaingaroa Harbour and seaward past the terminal lobe of the ebb-tidal delta, we used *Taitimu*, a $6\ \mathrm{m}$ pontoon boat with $150\ \mathrm{Hp}$ outboard motor. *Taitimu* was chosen for shallow draft, speed and agility to negotiate possibly shoaling waves and shallow sandbars. An RDI Workhorse ADCP was mounted to a downward pointing pole extending off port quarter of the boat and fixed to a sturdy but removable boom. A GPS receiver was mounted to the top of the pole and recorded continuously during the ADCP transects (see Figure C.1a). The pole was further secured with rope to avoid torsion under loading. The head of the ADCP was roughly $0.6\ \mathrm{m}$ below the water surface and required an $0.8\ \mathrm{m}$ blanking distance, allowing for measurements as close as $1.5\ \mathrm{m}$ beneath the water surface with $0.25\ \mathrm{m}$ vertical bins.

The original plan was to travel along east-to-west transects (longitudinal) centred on the main channel during as many states of the ebb-tide as possible, and to make cross-jet transects at multiple distances from the inlet as water conditions would allow. However, as the ebb-jet developed and current increased, travelling upstream with the ADCP deployed became difficult. Therefore we adjusted our measurement strategy to cope

with fast-moving water. We decided to deploy the ADCP and measure current only while travelling downstream (Figure C.1a), seaward from the inlet across the bar, and then disassemble the ADCP boom and travel at full speed (Figure C.1b) back to the entrance of the harbour to reassemble the ADCP boom and repeat. A few zig-zag transects were made in lieu of the cross-jet transects as driving the boat in a path perpendicular to the strong current was also difficult. For navigational safety, the boat did not get close enough to the channel margin linear bars to measure current near the lateral extents of the ebb-jet. In total, 23 separate ADCP tracks were recorded over a single falling tide, of which 16 (six longitudinal and ten transverse) were considered useful.

C.3 Results

Downward pointing ADCP transects were are measured during many times through the outgoing tide as shown in Figure C.2a for longitudinal tracks and Figure C.2b for transverse tracks. The falling tide is indicated with red lines, while labelled black lines indicate the time and water level during which each transect was measured.

Throughout the entire falling tide, the ebb-jet currents were aligned with the main channel orientation flowing from the inlet seaward over the ebb-

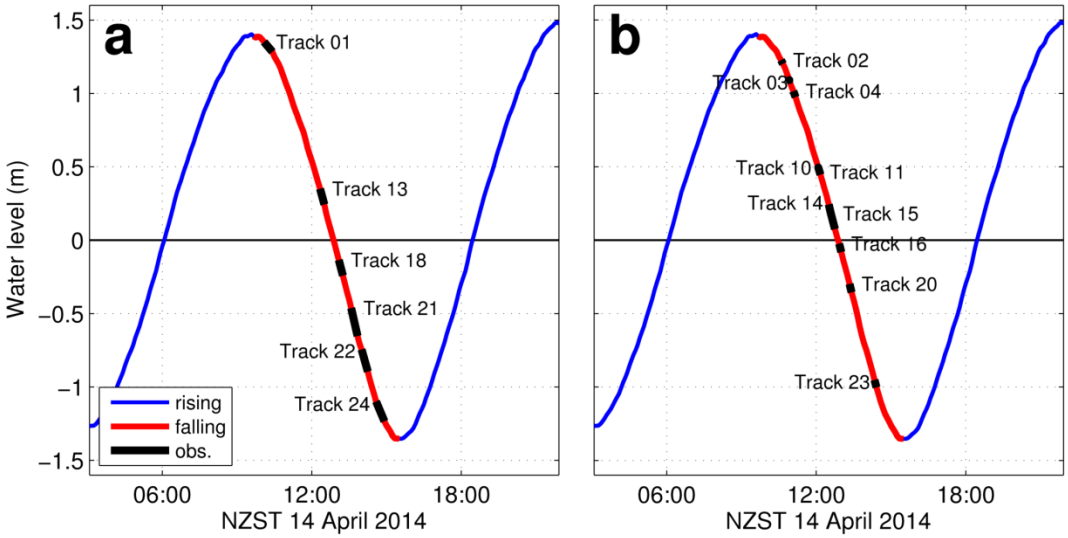

Figure C.2. Time of (a) longitudinal and (b) transverse tracks (indicated with black lines) relative to the observed water level at Raglan Wharf (data courtesy of Waikato Regional Council) during the falling tide (red line).

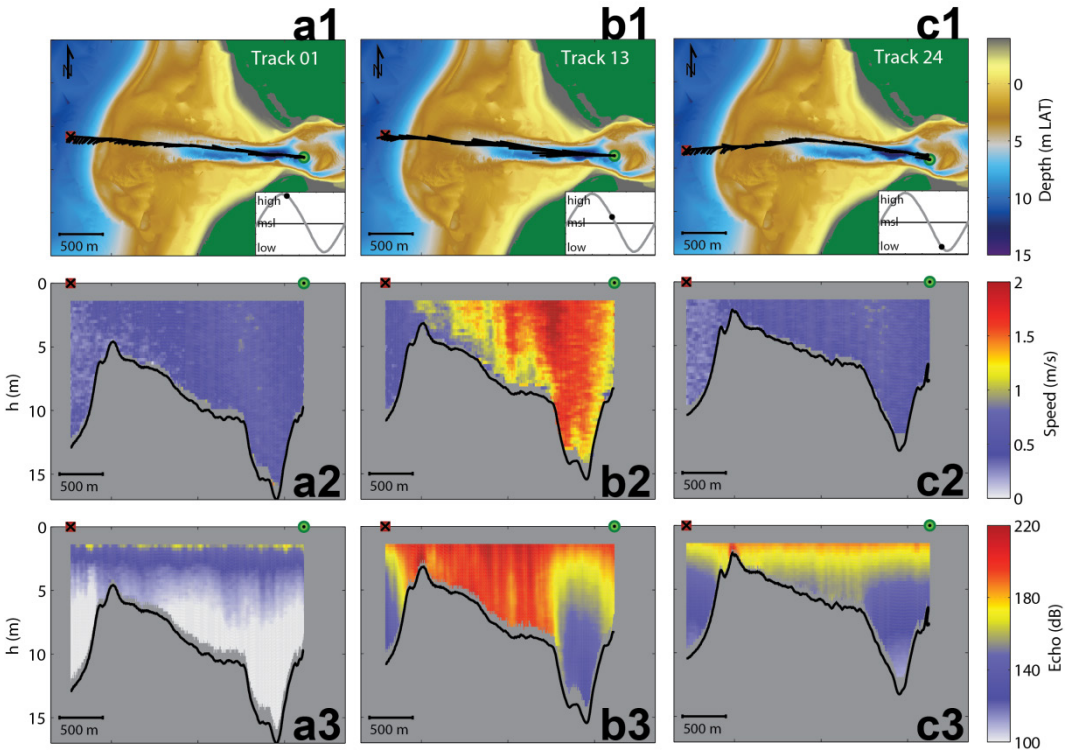

Figure C.3. Longitudinal transects, (a) Track 1 at the start of the falling tide, (b) Track 13 just before mid-tide, and (c) Track 24 near the end of the falling tide. The path of each track is shown in a1, b1 and c1 with quiver arrows showing the depth-averaged current direction. The vertical profile of current speed along each track is shown in a2, b2, and c2 along the observed depth profile, relative to the height of the water column $h(x)$. The backscatter intensity along each track is shown in a3, b3, and c3.

shoal (Figure C.3). Seaward of the ebb-shoal, the current was slow ($< 0.5\ \mathrm{m\ s^{-1}}$) and directed towards slightly south of west (Figure C.3a1). As the tide progressed from high to low, the speed of the ebb-jet current increased and then decreased.

At the start of the falling tide, the ebb currents were slower than $0.5\ \mathrm{m\ s^{-1}}$ throughout the main channel (Figure C.3a), with the fastest current occurring near the inlet gorge and decreasing with seaward distance. Seaward of the ebb-shoal, the current was directed to the south. Backscatter echo intensity was relatively low and uniform along the main channel and ebb-shoal isolated to the top few metres of the water column (Figure C3.a3).

At mid-tide, the ebb-jet current was the fastest (Figure C.3b2), extending throughout the entire main channel, longitudinally from the inlet seaward over the terminal lobe and filling the full width of the main channel.

Seaward of the ebb-shoal the current was directed to the west. The ebb-jet currents were fastest in the middle of the channel along the thalweg, tapering slightly near the channel margins. The fastest current at mid-tide was roughly $2\ \mathrm{m\ s^{-1}}$ in the main channel roughly $400\ \mathrm{m}$ seaward of the deepest part of the inlet gorge. Backscatter echo intensity was relatively high along much of the longitudinal transect (Figure C3.b3), with highest values occurring over the swash platform and ebb-shoal. The least observed backscatter during mid-tide was in the deepest part of the inlet gorge and with depth seaward of the ebb-shoal.

Near low-tide, the ebb-jet current slowed again to speeds similar to the start of the falling tide (compare Figure C.3d and Figure C.3a), but the height of the water column decreased by nearly $3\ \mathrm{m}$. Seaward of the ebb-shoal, the current was again directed to the south (Figure C3.d1). The

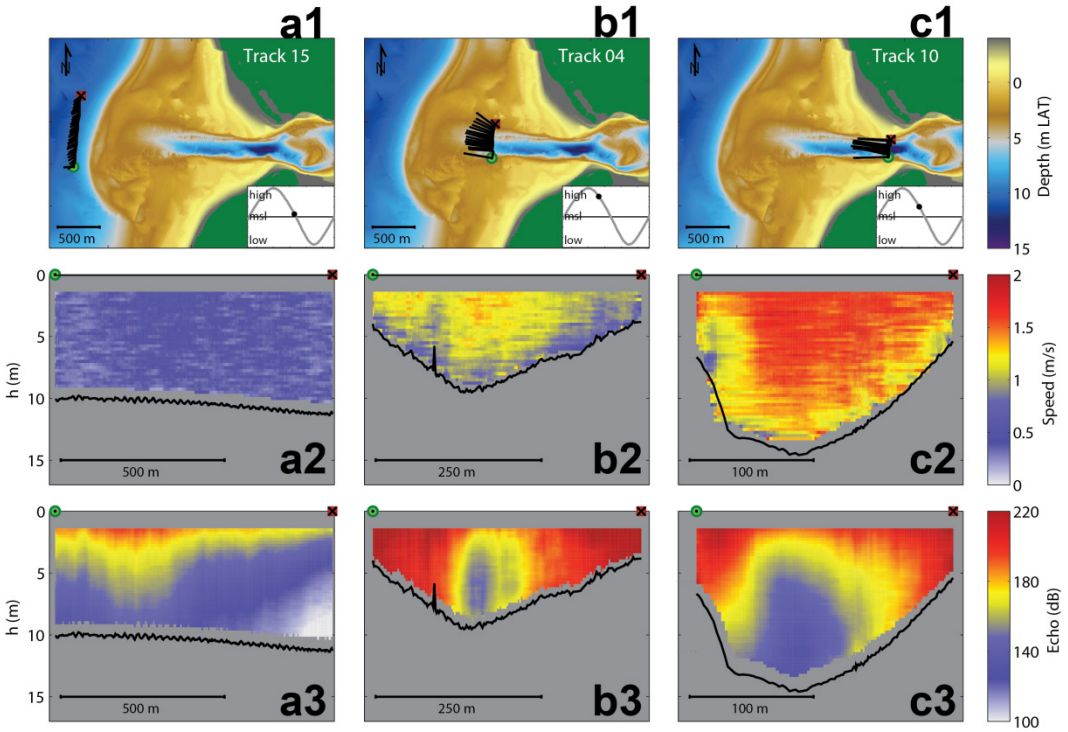

Figure C.4. Transverse transects during ebb tide at (a) Track 15 offshore of the ebb-shoal, (b) Track 4 on the swash platform, and (c) Track 10 at the inlet gorge. The path of each track is shown in a1, b1 and c1 along with a plot indicating the relative tide during measurement and with quiver arrows showing the depth-averaged current direction. The vertical profile of current speed along each track is shown in a2, b2, and c2 along the observed depth profile, relative to the height of the water column $h(x)$. The backscatter intensity along each track is shown in a3, b3, and c3.

backscatter intensity was higher than at the start of the falling tide, but less than at mid-tide, and highest along the top few metres of the water column, swash platform and ebb-shoal (Figure C3.d3).

The lateral structure of the jet during mid-tide can be seen in Figure C.4. The current at the inlet filled the entire width of the channel all flowing seaward in alignment with the channel, and with the fastest currents (1.5-$2.0\ \mathrm{ms}^{-1}$) above the thalweg in the middle to upper portions of the water column (Figure C.4c2). Backscatter intensity was less in the main part of the channel transect, with the highest intensity near the channel margins and at the surface (Figure C.4c3). Roughly $650\ \mathrm{m}$ seaward of the inlet gorge, the cross-jet transect Track 4 was over the swash platform (Figure C.4b). Currents there were less than at the inlet gorge (1.0-$1.5\ \mathrm{ms}^{-1}$), but still filled the entire width of the channel, with the fastest current over the thalweg and slight decay in speed near the northern margin. The backscatter intensity was higher at the swash platform than at the inlet gorge and filled more of the channel (compare Figures D4.b3 and D4.c3). Seaward of the ebb-shoal (Figure C.4a), the ebb-jet current was relatively uniform and directed slightly south of west. The backscatter intensity was less than Tracks 4 and 10, with the highest intensity located near the water surface. The magnitude of backscatter decayed diffusely with distance from the surface toward the seabed and centred offshore from the main channel opening in the ebb-shoal (Figure C.4a3).

C.4 Discussion and Conclusion

The ebb-jet current was fastest at mid-tide and filled the entire main channel (Figure C.3b and Figure C.4). The fastest currents occur in the middle of the channel, over the thalweg, and near the inlet gorge, decaying with distance seaward from the inlet.

The ‘fully-developed’ mid-tide ebb-jet observed at Raglan is an example of the type of ebb-jet event referred to previously in Chapter 3 and Chapter 4. The depth-averaged centreline current profiles during mid-tide (Track 13) decreased almost linearly with distance from the inlet (Figure C.5b). The

transverse depth-averaged current profile at the inlet gorge during mid-tide (Track 11) was fastest over the deepest part of the channel and decayed slightly near the channel margins (Figure C.5d). The transverse depth-averaged current profile further seaward along the swash platform (Track 4) was again fastest over the channel thalweg, but decayed only slightly over the length of the transect (Figure C.5c). Unfortunately, we did not get close enough to the channel levees to observe the full lateral decay of currents on the cross-jet profile.

The backscatter in the ebb-jet was strongest during the full outgoing tide (at mid-tide). The patterns of high backscatter intensity look as if they correspond to something in the water, most likely suspended sediment that may be stirred up by small waves in the shallow areas. Future attempts could make an effort to identify the source of elevated backscatter intensity in the mid-tide ebb-jet.

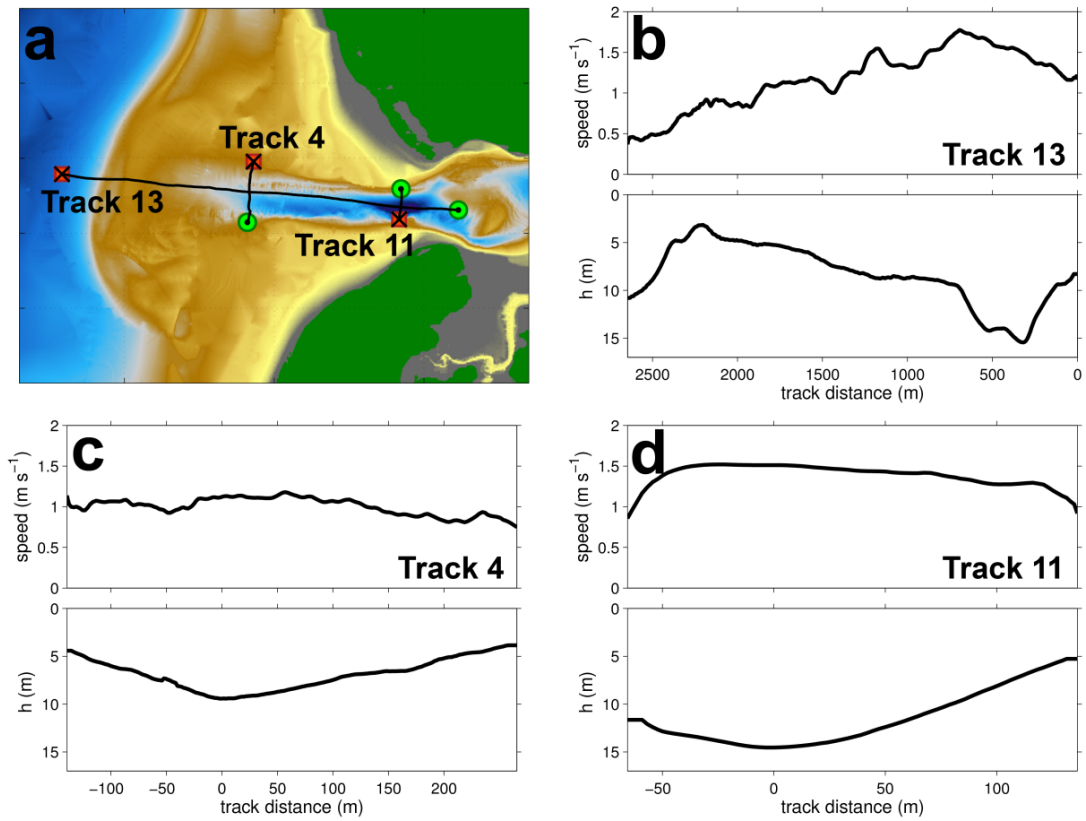

Figure C.5. Depth averaged current profiles at transect locations (a) for (b) longitudinal Track 13, (c) transverse Track 4 and (d) Track 11. For each track, the depth averaged speed and height of water column profiles $h(x)$ are shown.

Downward-pointing ADCP transects were able to reveal aspects of the longitudinal and transverse structure of the ebb-jet during a falling tide. The requirement for calm wind and waves restricts the types of ebb-jets able to measure. In future attempts, it could save time to focus more attention to gathering measurements during the mid-tide. More coverage is required to measure the cross-jet current profile on the transverse transects extending to the shallow channel margin linear bars, conditions permitting.

Appendix D

Nice Waves on the Raglan Bar

Large waves ($H_s \approx 2$ m) breaking on the Raglan Bar, captured on 14th April 2013. Photo courtesy Pieter ten Broek (aka '*social_advances*').

Note: Appendix D presents an article entitled *Nice Waves on the Raglan Bar* which was included in the New Zealand Coastal Society's Coastal News intended as a means to communicate research among coastal-interest groups. The article is reproduced here as it appeared in the Coastal News with permission from editor Shelly Biswell.

Harrison, S.R. (2013). Nice Waves on the Raglan Bar. Coastal News, No. 53, New Zealand Coastal Society, July 2013.

Nice Waves on the Raglan Bar

by Shawn Harrison, PhD student, Earth & Ocean Sciences, University of Waikato

This past summer and early autumn, Raglan surfers found themselves enjoying long, smooth barrelling waves (Figure 1). While this is a normal occurrence on Raglan's famed left-hand point breaks, these waves were being ridden to the right on "The Bar", the ebb-tide delta that sits off the entrance of Whaingaroa Harbour. The Bar is well known as a surfing spot; however, despite abundant swell that consistently breaks over its shallow sandbars, the shape of The Bar only occasionally produces high-quality breakers suitable for surfing. Indeed, before this year, the last time The Bar was working consistently was in early 2005.

Figure 1: Surfers enjoying crisp, overhead, right-handed barrels on the southern end on the ebb-tide delta at Raglan on 2 April 2013. Courtesy: B-rex.

As part of my research into the morphology of ebb-tidal deltas (ETDs), I thought it would be interesting to explore the physical characteristics of The Bar that lead to these optimum surfing conditions. In general, ETDs are morphological structures occurring naturally on the seaward side of tidal constrictions. They form at the interface between a tidal inlet and the open sea where tidal currents and wave action meet in a complex, highly dynamic way – shaping the available sediment into coherent arrangements of bars and channels.

ETDs are a characteristic of the entrances to many of New Zealand's estuaries, and can pose a significant navigational hazard to vessels entering and leaving a harbour. At locations where shipping traffic is important (such as at Tauranga and Otago harbours), maintenance dredging is necessary to stop the natural dynamics of ETDs from impacting on port operations. Moreover, the size and shape of ETDs can greatly impact the nearby coastal zone. The shallow bars of a delta dissipate wave energy offshore, protecting the tidal inlet and redirect waves onto neighbouring beaches. They also provide a bypassing mechanism in the littoral system, allowing sediment to cross tidal inlets on its along-coast journey. There is a strong correlation with ETD size and nearby beach volume due to the repositioning of wave energy by the mobile sandbars of an ETD.

The Raglan Bar (Figure 2) is a complex, multi-component example of an ETD extending approximately 1800 metres offshore of the west coast. Most of the sand is derived from the northerly transport of sediment originating from Taranaki. Tidal and wave action transport the sediment up the west coast along most of the North Island. The sediment is pushed shoreward by waves and seaward by strong ebbing tidal currents exiting the harbour. The heavy, black sand accumulates where these opposing forces meet. The Bar includes an ebb-dominated main channel with spring ebb currents reaching three metres per second. The deepest point of the main channel occurs at the inlet gorge and is approximately 15 metres below low tide. The channel extends seaward to the west, with depths becoming shallower with distance from the inlet. The shallowest part of the main channel is at its terminal lobe, which moves cross-shore and changes depth depending on the combination of wave and tidal conditions. The terminal lobe is the seaward-most extent of the delta where approaching waves break in-line with the jet-axis of the main channel.

Broad sheets of consolidated accumulations of sand, called "swash platforms" flank both sides of the main channel. The swash platforms are composed of large intertidal sandbars called "swash bars". These sandbars tend to control the course of the tidal flow, forcing flood and ebb currents through different channels. Also, excess water mass from breaking waves is returned through these channels. The terminal lobe connects the swash platforms along the seaward-most limit of the delta. The terminal lobe tends to be the first point for advancing waves to break. Often the terminal lobe can take the shape of a shield.

Part of my work involves the analysis of geo-rectified high-resolution video images, collected by NIWA's Cam-Era system for Waikato Regional Council, used to track wave-breaking patterns which correspond to the evolving position and shape of the Raglan

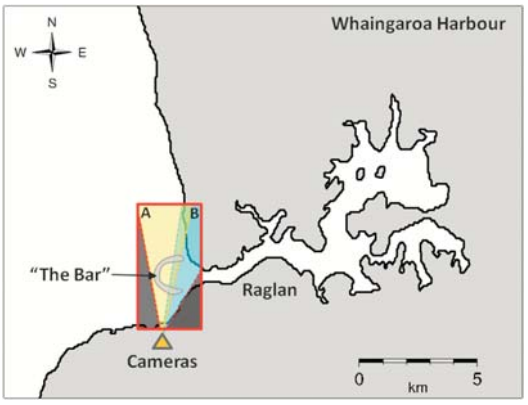

Figure 2: Map showing the location of "The Bar" seaward of the inlet to Whaingaroa Harbour at Raglan. The position and view of Waikato Regional Council's "Raglan A" and "Raglan B" Cam-Era cameras are indicated.

Bar. The movements are linked to the prevailing wave and tidal conditions in order to correlate variation in the hydrodynamic climate with morphological response. Although a local example, these video-based measurements of the morphological responses at Raglan are used to guide development of a model that can be used at ETDs in other parts of the world. Video-based techniques are a useful tool in observing nearshore coastal processes, particularly in areas like ETDs where conditions are often too dangerous to make measurements *in situ*. Also, observations can be made much more frequently than is possible with standard instrumentation. Other studies using similar techniques have been successfully applied to observe rip currents, swash, groundwater seepage, and beach morphology.

The sequence of imagery over recent years shows the evolution of The Bar from unsurfable to surfable (Figure 3). In 2010 and 2011, the terminal lobe was an almost straight, linear shape with the southern end situated relatively far offshore from Ngarunui Beach. This configuration caused waves to break too quickly to provide a surfable wave face. By late 2011, the southern end of the terminal lobe began migrating shoreward while the terminal lobe directly offshore of the main channel moved slightly offshore, increasing the curvature. Also, during this time, a breach in the southern arm caused the formation of a channel through the southern swash platform allowing tidal and wave return flow currents to move between the inlet and the southern lobe. The presence of this channel provided a mechanism for sediment mobilised by waves to be carried away from the beach.

By late 2012, this channel had become compressed and reoriented to almost shore parallel in the very nearshore of the beach. The presence of this nearshore channel corresponded with a substantial loss of sediment from Ngarunui Beach leaving large exposed rocks and a two-metre scarp in the vegetated dunes in some spots. The loss of sand from Ngarunui Beach was paired with an accretion of sand on the beach to the north of the inlet. Previously exposed rocks along that beach are now well covered; the northern terminal lobe has extended and the beach has a full profile with the high-water line well away from the toe of the vegetated dunes.

Meanwhile the southern end of the terminal lobe continued to advance shoreward making an almost shore-perpendicular angle. The long, smooth, curved terminal lobe of early 2013 allowed waves to peel slowly enough for surfing, but quickly enough to make a challenge. Local surfer, Miles Ratima, described the waves as "fast peeling with clean, hollow barrels – shaped similarly to waves in Indonesia". During early April 2013 (Figure 4) a

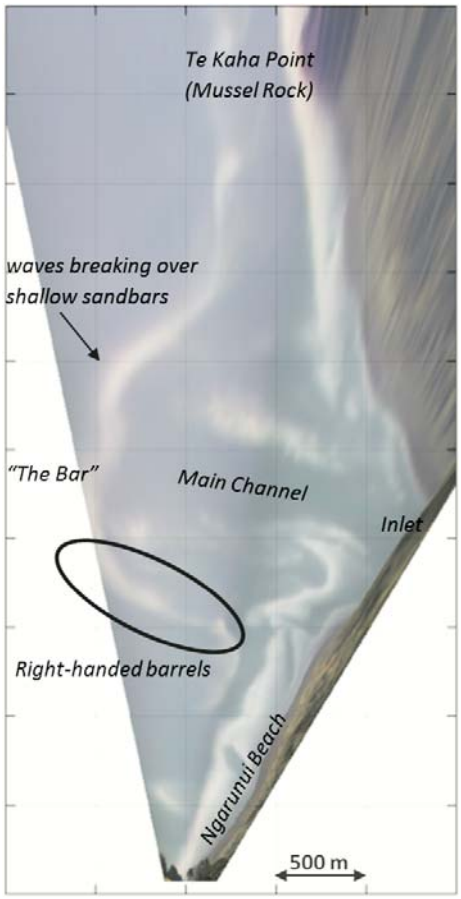

Figure 4: Geo-rectified, 10-minute averaged mosaic of video images during the afternoon of 2 April 2013. The white areas indicate wave breaking and imply shallow sandbar position.

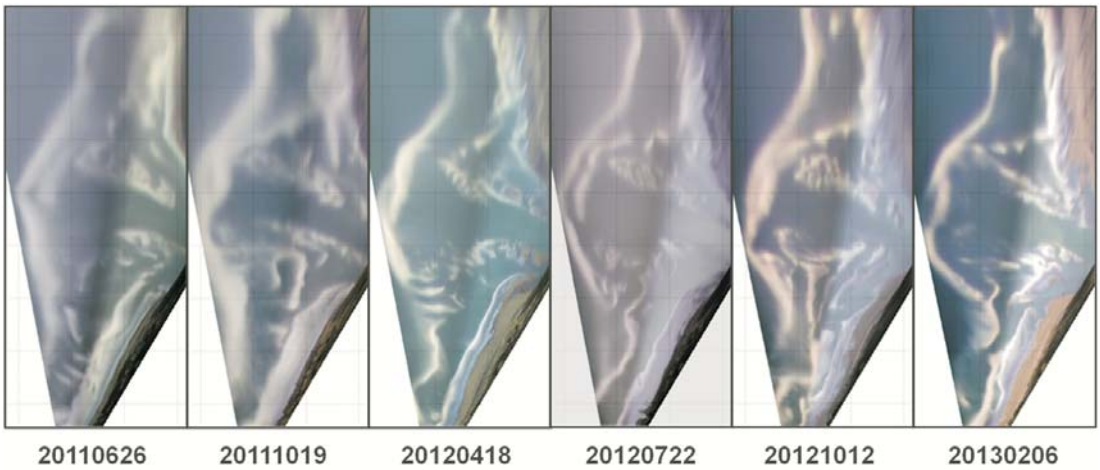

Figure 3: Sequence of geo-rectified, time-averaged video image mosaics showing the evolving configuration of the ebb-tidal delta at Raglan, New Zealand (The Bar) from 26 June 2011 (left) to 6 February 2013 (right).

combination of calm, fine weather and a series of well-organised long-period swells brought The Bar to life with excited surfers claiming minute-long barrels and turn after turn of right-handed pleasure.

The size and shape of the ebb-tidal delta at Raglan are near equilibrium on decadal timescales; however, the positions of the shoals and bars can move dramatically over a period of days to weeks in response to changing energetic conditions such as storms or large swell events. Indeed, as this article is being written, The Bar has changed shape again and is no longer consistently surfable.

The Raglan Bar is an example of a morphological system, which just like beaches, undergoes state changes. My doctoral work explores the hypothesis that upstate geometries are more along-coast uniform, whereas the more complex bar patterns develop during downstate changes which accompany lower energy conditions. My challenge is to find the trigger that forces these state changes. These sandbar patterns drive wave focusing and currents on The Bar, which apart from being good for surfing, also control the navigation hazard. My thesis will ultimately contribute to better hazard management in this highly dynamic environment.

Figure 5: Perfect waves breaking on the southern end of The Bar at Raglan on 2 April 2013. Courtesy: Brad George.

NZCS Management Committee

Chairperson:	Deirdre Hart	deirdre.hart@canterbury.ac.nz
Deputy Chairperson/IPENZ Coordinator:	Rick Liefting	rick.liefting@waikatoregion.govt.nz
Treasurer:	Eric Verstappen	eric.verstappen@tasman.govt.nz
Deputy Treasurer:	Andrew Swales	a.swales@niwa.co.nz
Membership & Partners Liaison:	Paul Creswell	paul.creswell@mpi.govt.nz
Regional Coordinator:	Hugh Leersnyder	hugh.leersnyder@beca.com
Education & University Coordinator:	Christopher Gomez	christopher.gomez@canterbury.ac.nz
Central Government Coordinator:	Sarah McRae	smcrae@doc.govt.nz
***Coastal News* Coordinator:**	Amy Robinson	amy.robinson@waikatoregion.govt.nz
Website & Digest Coordinator:	Jose Borrero	jose@ecoast.co.nz
Other NZCS Contacts		
Administrator & Communications Coordinator:	Renee Foster	nzcoastalsociety@gmail.com
***Coastal News* Editor:**	Shelly Biswell	shelly@biswell.net

NZCS Regional Coordinators

Every region has a NZCS Regional Coordinator who is available to help you with any queries about NZCS activities or coastal issues in your local area.

North Island

Northland	Michael Day André Labonté	michaeld@nrc.govt.nz labonte@xtra.co.nz
Auckland	Hugh Leersnyder	hugh.leersnyder@beca.com
Waikato	Christin Atchinson	christin.atchinson@waikatoregion.govt.nz
Bay of Plenty	Mark Ivamy Sharon De Luca	MIvamy@tonkin.co.nz sharon.deluca@boffamiskell.co.nz
Hawke's Bay	Neil Daykin	Daykin@hbrc.govt.nz
Taranaki	Emily Roberts	emily.roberts@trc.govt.nz
Wellington	Iain Dawe	iain.dawe@gw.govt.nz

South Island

Upper South Island	Eric Verstappen	eric.verstappen@tasman.govt.nz
Canterbury	Justin Cope	justin.cope@ecan.govt.nz
Otago	Mike Hilton	mjh@geography.otago.ac.nz
Southland	Nick Ward	nick.ward@es.govt.nz

References

Aarninkhof, S. G., Turner, I. L., Dronkers, T. D., Caljouw, M., & Nipius, L. (2003). A video-based technique for mapping intertidal beach bathymetry.*Coastal Engineering*, *49*(4), 275-289.

Abramovich, G. N. (1963). The theory of turbulent jets, 1963. *The Massachusetts Institute of Technology Press, Cambridge*.

Apotsos, A., Raubenheimer, B., Elgar, S., & Guza, R. T. (2008). Testing and calibrating parametric wave transformation models on natural beaches. *Coastal Engineering*, *55*(3), 224–235.

Ashton, A. D., & Giosan, L. (2011). Wave-angle control of delta evolution. *Geophysical Research Letters*, *38*(13).

Balouin, Y., Morris, B. D., Davidson, M. A., & Howa, H. (2004). Morphology evolution of an ebb-tidal delta following a storm perturbation: assessments from remote sensed video data and direct surveys. *Journal of coastal research*, 415-423.

Barnard, P. L., & Warrick, J. A. (2010). Dramatic beach and nearshore morphological changes due to extreme flooding at a wave-dominated river mouth. *Marine Geology*, *271*(1), 131-148.

Bertin, X., Fortunato, A. B., & Oliveira, A. (2009). A modelling-based analysis of processes driving wave-dominated inlets. *Continental Shelf Research*, *29*(5), 819–834.

Bijker, E. W. (1967). Some considerations about scales for coastal models with movable bed. *Tech. Rep.* 50, (WL) Delft Hydraulics, Delft, The Netherlands .

Bliss, P.P. (1871). Let the Lower Lights Be Burning. (No. 335) in *Hymns of The Church of Jesus Christ of Latter-day Saints*, The Church of Jesus Christ of Latter-day Saints, Salt Lake City, 1985, 434pp.

Borichansky, L. S., & Mikhailov, V. N. (1966). Interaction of river and sea water in the absence of tides. *Scientific problems of the humid tropical zone deltas and their implications*, 175–180.

Bowen, A. J., Inman, D. L., & Simmons, V. P. (1968). Wave 'set‐down' and set‐Up. *Journal of Geophysical Research, 73*(8), 2569-2577.

Bryan, K. R., Robinson, A., & Briggs, R. M. (2007). Spatial and temporal variability of titanomagnetite placer deposits on a predominantly black sand beach. *Marine Geology*, *236*(1), 45-59.

Cacina, N. (1989). Test and evaluation of surf forecasting model. M.Sc. Thesis, Naval Postgraduate School, Monterey, CA, 41pp.

Chen, J. L., Hsu, T. J., Shi, F., Raubenheimer, B., & Elgar, S. (2015). Hydrodynamic and sediment transport modelling of New River Inlet (NC) under the interaction of tides and waves. *Journal of Geophysical Research: Oceans.* doi: 10.1002/2014JC010425

Clark, D. B., Lenain, L., Feddersen, F., Boss, E., & Guza, R. T. (2014). Aerial imaging of fluorescent dye in the near shore. *Journal of Atmospheric and Oceanic Technology*, *31*(6), 1410-1421.

Cowell, P. J., & Thom, B. G. (1994). Morphodynamics of coastal evolution. In: R. W. G. Carter, & C. D. Woodroffe (Eds.), *Coastal Evolution – Late Quaternary Shoreline Morphodynamic*s. Cambridge University Press, Cambridge, United Kingdom and New York, NY, USA, pp 33-46.

Dalrymple, R. A., & Dean, R. G. (1991). *Water wave mechanics for engineers and scientists,* Vol. 2 of *Advanced series on ocean engineering*. World Scientific Publishing Company. 235pp.

Daly, C. J., Bryan, K. R., Gonzalez, M. R., Klein, A. H. F., & Winter, C. (2014). Effect of selection and sequencing of representative wave conditions on process-based predictions of equilibrium embayed

beach morphology. *Ocean Dynamics*, *64(6)*, 863-877, doi:10.1007/s10236-014-0730-9.

De Jong, D. (1998). Crossing the bar: Stories. Auckland: David Ling. 159 pp.

de Swart, H. E., & Zimmerman, J. T. F. (2009). Morphodynamics of tidal inlet systems. *Annual Review of Fluid Mechanics*, *41*, 203-229.

de Vriend, H.J., 1991a. Mathematical modeling and largescale coastal behavior, part I: physical processes. J. Hydraul. Res., 29(6): 727-740.

de Vriend, H.J., 1991b. Mathematical modeling and largescale coastal behavior, part II: predictive models. J. Hydraul. Res., 29(6): 741-753.

de Vriend, H. J., Capobianco, M., Chesher, T., De Swart, H. D., Latteux, B., & Stive, M. J. F. (1993). Approaches to long-term modelling of coastal morphology: a review. *Coastal Engineering*, *21*(1), 225-269.

de Vriend, H. J., Bakker, W. T., & Bilse, D. P. (1994). A morphological behaviour model for the outer delta of mixed-energy tidal inlets. *Coastal Engineering*, *23*(3), 305-327.

Dodet, G., Bertin, X., Bruneau, N., Fortunato, A. B., Nahon, A., & Roland, A. (2013). Wave-current interactions in a wave-dominated tidal inlet. *Journal of Geophysical Research: Oceans*, *118*(3), 1587–1605.

Edmonds, D. A., & Slingerland, R. L. (2007). Mechanics of river mouth bar formation: Implications for the morphodynamics of delta distributary networks. *Journal of Geophysical Research: Earth Surface*, *112*(F2), doi:10.1029/2006JF000574.

Environment Waikato (2002). The Whaingaroa environment catchment plan. Report No. 793960. Hamilton, Environment Waikato.

Fagherazzi, S., & Overeem, I. (2007). Models of deltaic and inner continental shelf landform evolution. *Annual Review of Earth and Planetary Sciences*, *35*, 685–715.

Feddersen, F. (2012). Observations of the surf-zone turbulent dissipation rate. *Journal of Physical Oceanography, 42*(3), 386-399.

Fitzgerald, D. M. (1984). Interactions between the ebb-tidal delta and landward shoreline: Price Inlet, South Carolina. *Journal of Sedimentary Research*, *54*(4), 1303–1318.

Fredsøe, J. (1984). Turbulent boundary layer in wave-current motion. *Journal of Hydraulic Engineering*, *110*(8), 1103-1120.

French, J. L. (1960). *Tidal flow in entrances*. Committee on Tidal Hydraulics, Corps of Engineers, US Army, 73 pp.

Gallop, S. L., Bryan, K. R., & Coco, G. (2009). Video observations of rip currents on an embayed beach. *Journal of Coastal Research*, 49-53.

Galloway, W.E. (1975). Process framework for describing the morphologic and stratigraphic evolution of deltaic depositional systems. *Deltas: models for exploration*, Broussard, M.L. (Ed.). *Houston Geologic Society, Houston*, 99-149.

Gelfenbaum, G., Sherwood, C.R., Peterson, C.D., Kaminsky, G.M., Buijsman, M.C., Twichell, D.C., Ruggiero, P., Gibbs, A.E., Reed, C. (1999). The Columbia River littoral cell: a sediment budget overview. *Proceedings of Coastal Sediments 1999.* ASCE, pp 1660-1675.

Gorman, R. M., Bryan, K. R., & Laing, A. K. (2003). Wave hindcast for the New Zealand region: nearshore validation and coastal wave climate. *New Zealand Journal of Marine and Freshwater Research*, *37*(3), 567-588.

Grant, W. D., & Madsen, O. S. (1979). Combined wave and current interaction with a rough bottom. *Journal of Geophysical Research: Oceans (1978–2012)*,*84*(C4), 1797-1808.

Guedes, R., Bryan, K. R., & Coco, G. (2013). Observations of wave energy fluxes and swash motions on a low-sloping, dissipative beach. *Journal of Geophysical Research: Oceans*, *118*(7), 3651-3669.

Guza, R.T., & Thornton, E.B. (1980). Local and shoaled comparisons of sea surface elevation, pressures and velocities. *Journal of Geophysical Research, 85*(C3), 1524–1530.

Harrison, S.R. and Hunt, S. (2014). Whaingaroa Harbour, New Zealand. *Hydrographic Chart.* Distributed by University of Waikato and Waikato Regional Council at NZCS 2014, Raglan. 1 p.

Hayes, M. O. (1979). Barrier island morphology as a function of tidal and wave regime. In: S.P. Leatherman (Editor), *Barrier Islands from the Gulf of St. Lawrence to the Gulf of Mexico.* Academic Press, New York, pp 1-27.

Hayes, M. O. (1980). General morphology and sediment patterns in tidal inlets.*Sedimentary geology*, *26*(1), 139-156.

Heath, R. A. (1975). Stability of some New Zealand coastal inlets. *New Zealand Journal of Marine and Freshwater Research*, *9*(4), 449-457.

Herodotus. *An Account of Egypt*. Translated by G.C. Macaulay. Produced by J. Bickers, Dagny, and D. Widger. Project Gutenburg, eBook #2131, accessed online on May 30, 2015 at http://www.gutenberg.org/files/2131/.

Heath, R. A. (1976). Broad classification of New Zealand inlets with emphasis on residence times. *New Zealand Journal of Marine and Freshwater Research*,*10*(3), 429-444.

Hicks, D. M., & Hume, T. M. (1996). Morphology and size of ebb tidal deltas at natural inlets on open-sea and pocket-bay coasts, North Island, New Zealand. *Journal of Coastal Research*, *12*(1), 47–63.

Hicks, D. M., Hume, T. M., Swales, A., & Green, M. O. (1999). Magnitudes, spatial extent, time scales and causes of shoreline change adjacent to an ebb tidal delta, Katikati inlet, New Zealand. *Journal of Coastal Research*, *15*(1), 220-240.

Holman, R. A., & Stanley, J. (2007). The history and technical capabilities of Argus. *Coastal Engineering*, *54*(6), 477-491.

Huisman, C. E., Bryan, K. R., Coco, G., & Ruessink, B. G. (2011). The use of video imagery to analyse groundwater and shoreline dynamics on a dissipative beach. *Continental Shelf Research*, *31*(16), 1728-1738.

Ismail, N. M. (1980). Wave-Current Interaction. PhD thesis. University of California at Berkeley, Berkeley, California.

Ismail, N. M., & Wiegel, R. L. (1983). Opposing wave effect on momentum jets spreading rate. *Journal of Waterway, Port, Coastal, and Ocean Engineering*,*109*(4), 465–483.

Joshi, P. B. (1982). Hydromechanics of tidal jets. *Journal of the Waterway Port Coastal and Ocean Division*, *108*(3), 239-253.

Joshi, P. B., & Taylor, R. B. (1983). Circulation induced by tidal jets. *Journal of Waterway, Port, Coastal, and Ocean Engineering*, *109*(4), 445–464.

Kang, K., & Di Iorio, D. (2006). Depth-and current-induced effects on wave propagation into the Altamaha River Estuary, Georgia. *Estuarine, Coastal and Shelf Science*, *66*(3), 395–408.

Kilcher, L. F., & Nash, J. D. (2010). Structure and dynamics of the Columbia River tidal plume front. *Journal of Geophysical Research: Oceans*, *115*(C5), doi:10.1029/2009JC006066.

Kilcher, L. F., Nash, J. D., & Moum, J. N. (2012). The role of turbulence stress divergence in decelerating a river plume. *Journal of Geophysical Research: Oceans*, *117*(C5), doi:10.1029/2011JC007398.

Komar, P. D. (1971), The mechanics of sand transport on beaches, *J. Geophys.Res., 76(3)*, 713–721, doi:10.1029/JC076i003p00713.

Kovesi, P. (2012). Phase preserving tone mapping of non-photographic high dynamic range images. *Proceedings of the Australian Pattern Recognition Society Conference on Digital Image Computing Techniques and Applications (DICTA 2012).* Fremantle. 2012.

Kraus, N. C. (2000). Reservoir model of ebb-tidal shoal evolution and sand bypassing. *Journal of Waterway, Port, Coastal, and Ocean Engineering*, *126*(6), 305-313.

Kuznetsov, I. A. (1998). *Elements of applied bifurcation theory* (Vol. 112). Springer Science & Business Media. 591 pp.

Leonardi, N., Canestrelli, A., Sun, T., & Fagherazzi, S. (2013). Effect of tides on mouth bar morphology and hydrodynamics. *Journal of Geophysical Research: Oceans, 118*(9), 4169-4183.

Lesser, G. R., Roelvink, J. A., Van Kester, J. A. T. M., & Stelling, G. S. (2004). Development and validation of a three-dimensional morphological model. *Coastal Engineering*, *51*(8), 883-915.

Lesser, G.R. (2009). An approach to medium-term coastal morphological modelling. PhD thesis, UNESCO-IHE & Delft University of Technology, Delft. CRC Press/Balkema. ISBN 978-0-415-55668-2.

Li, M. Z., Wright, L. D., & Amos, C. L. (1996). Predicting ripple roughness and sand resuspension under combined flows in a shoreface environment. *Marine Geology*, *130*(1), 139-161.

LINZ (2010). *Raglan Harbour (Whaingaroa)*, NZ4421, Edition I. Scale 1:12,500. New Zealand, North Island – West Coast. Originally

published, October 1978, by the Hydrographer RNZN. New Edition published, July 2001, under the authority of Land Information New Zealand. Reprinted January 2010.

Lippmann, T. C., & Holman, R. A. (1989). Quantification of sand bar morphology: A video technique based on wave dissipation. Journal of Geophysical Research, 94(1), 995-1011. doi:10.1029/JC094iC01p00995

Lippmann, T. C., Brookins, A. H., & Thornton, E. B. (1996). Wave energy transformation on natural profiles. *Coastal Engineering*, *27*(1), 1–20.

Liu, P. L., & Dalrymple, R. A. (1978). Bottom frictional stresses and longshore currents due to waves with large angles of incidence. *Journal of Marine Research*, *36*(2), 357-375.

Longuet-Higgins, M. S., & Stewart, R. W. (1964). Radiation stresses in water waves; a physical discussion, with applications. In *Deep Sea Research and Oceanographic Abstracts* (Vol. 11, No. 4, pp. 529–562). Elsevier.

Malhadas, M. S., Leitão, P. C., Silva, A., & Neves, R. (2009). Effect of coastal waves on sea level in Óbidos Lagoon, Portugal. *Continental Shelf Research*, *29*(9), 1240–1250.

Marino, J. N., & Mehta, A. J. (1987). Inlet ebb shoals related to coastal parameters. In *Coastal Sediments (1987)* (pp. 1608-1623). ASCE.

McKergow, L. A., Pritchard, M., Elliott, A. H., Duncan, M. J., & Senior, A. K. (2010). Storm fine sediment flux from catchment to estuary, Waitetuna-Raglan Harbour, New Zealand. *New Zealand Journal of Marine and Freshwater Research*, *44*(1), 53-76.

Murray, A. B., & Thieler, E. R. (2004). A new hypothesis and exploratory model for the formation of large-scale inner-shelf sediment sorting

and “rippled scour depressions”. *Continental Shelf Research*, *24*(3), 295-315.

Nardin, W., & Fagherazzi, S. (2012). The effect of wind waves on the development of river mouth bars. *Geophysical Research Letters*, *39*(12), doi:10.1029/2012GL051788.

Nardin, W., Mariotti, G., Edmonds, D. A., Guercio, R., & Fagherazzi, S. (2013). Growth of river mouth bars in sheltered bays in the presence of frontal waves. *Journal of Geophysical Research: Earth Surface*, *118*(2), 872–886.

Nearshore Processes Community. (2015). The future of nearshore processes research: Coastal forum Dec 2014. *Shore and Beach, 83*(1), 13-38.

NIWA (2015a). *Raglan, Karioi, 2027, Daily Rain data*. CliFlo: NIWA’s National Climate Database on the Web. url: http://cliflo.niwa.co.nz/. Retrieved 7-April-2015.

NIWA (2015b). *Port Tahoroa AWS, 2136, Hourly MSLP data*. CliFlo: NIWA’s National Climate Database on the Web. url: http://cliflo.niwa.co.nz/. Retrieved 7-April-2015.

Nowacki, D. J., Horner-Devine, A. R., Nash, J. D., & Jay, D. A. (2012). Rapid sediment removal from the Columbia River plume near field. *Continental Shelf Research*, *35*, 16-28.

Oertel, G. F. (1972). Sediment transport of estuary entrance shoals and the formation of swash platforms. *Journal of Sedimentary Research*, *42*(4), 857-863.

Oertel, G. F. (1977). Geomorphic cycles in ebb deltas and related patterns of shore erosion and accretion. *Journal of Sedimentary Research*, *47*(3).

Oertel, G. F. (1988). Processes of sediment exchange between tidal inlets, ebb deltas and barrier islands. In *Hydrodynamics and sediment dynamics of tidal inlets.* Springer New York, pp. 297–318.

Olabarrieta, M., Warner, J. C., & Kumar, N. (2011). Wave-current interaction in Willapa Bay. *Journal of Geophysical Research: Oceans*,*116*(C12), doi:10.1029/2011JC007387.

Olabarrieta, M., Geyer, W. R., & Kumar, N. (2014). The role of morphology and wave-current interaction at tidal inlets: An idealized modeling analysis. *Journal of Geophysical Research: Oceans*, *119*(12), 8818-8837, doi:10.1002/2014JC010191.

Old, C. P., & Vennell, R. (2001). Acoustic Doppler current profiler measurements of the velocity field of an ebb tidal jet. *Journal of Geophysical Research: Oceans*, *106*(C4), 7037–7049.

Orescanin, M., Raubenheimer, B., & Elgar, S. (2014). Observations of wave effects on inlet circulation. *Continental Shelf Research*, 82, 37–42.

Ortega-Sánchez, M., Losada, M. A., & Baquerizo, A. (2008). A global model of a tidal jet including the effects of friction and bottom slope. *Journal of Hydraulic Research*, *46*(1), 80–86.

Özsoy, E. (1977). Flows and Mass Transport in the Vicinity of Tidal Inlets. PhD thesis, 206 pp., Coastal and Oceanographic Engineering Laboratory, University of Florida. Gainesville, Florida, October, 1977.

Özsoy, E., & Ünlüata, Ü. (1982). Ebb-tidal flow characteristics near inlets. *Estuarine, Coastal and Shelf Science*, *14*(3), doi:10.1016/S0302-3524(82)80015-7.

Özsoy, E. (1986). Ebb-tidal jets: a model of suspended sediment and mass transport at tidal inlets. *Estuarine, Coastal and Shelf Science*, *22*(1), 45-62.

Pawlowicz, R., Beardsley, B., & Lentz, S. (2002). Classical tidal harmonic analysis including error estimates in MATLAB using T_TIDE. *Computers & Geosciences, 28(8),* 929-937.

Phillips, D.J. (2004). Sediment Dynamics of a Shallow Exposed Surfing Headland. PhD thesis. University of Waikato, Hamilton, New Zealand.

Phillips, D., Black, K., & Healy, T. (2009). Issues Surrounding the Construction of Artificial Reefs by Detailed Examination of a Natural Headland. *Reef Journal*,*1*(1), 162-176.

Phillips, O. M. (1977). *The Dynamics of the Upper Ocean*. Cambridge Univ. Press, Cambridge, 309pp.

Plant, N. G., Holman, R. A., Freilich, M. H., & Birkemeier, W. A. (1999). A simple model for interannual sandbar behavior. Journal of Geophysical Research C: Oceans, 104(7), 15755-15776. doi:10.1029/1999JC900112

Plant, N. G., Stefan G. J. Aarninkhof, Turner, I. L., & Kingston, K. S. (2007). The performance of shoreline detection models applied to video imagery. Journal of Coastal Research, 23(3), 658-670.

Ranasinghe, R., Swinkels, C., Luijendijk, A., Roelvink, D., Bosboom, J., Stive, M., & Walstra, D. (2011). Morphodynamic upscaling with the MORFAC approach: Dependencies and sensitivities. *Coastal Engineering*, *58*(8), 806-811.

Raubenheimer, B., Guza, R. T., & Elgar, S. (1996). Wave transformation across the inner surf zone. *Journal of Geophysical Research: Oceans*, *101*(C11), 25589–25597.

Roelvink, J. A. (1993). Dissipation in random wave groups incident on a beach. *Coastal Engineering*, *19*(1), 127–150.

Roelvink, J. A. (2006). Coastal morphodynamic evolution techniques. *Coastal Engineering*, *53*(2), 277-287.

Roelvink, J. A., & Reniers, A. (2011). *A Guide to Modeling Coastal Morphology* (Vol. 12). World Scientific, 292 pp

Rowland, J. C., Stacey, M. T., & Dietrich, W. E. (2009). Turbulent characteristics of a shallow wall-bounded plane jet: experimental implications for river mouth hydrodynamics. *Journal of Fluid Mechanics*, *627*, 423-449, doi:10.1017/S0022112009006107.

Rowland, J. C., Dietrich, W. E., & Stacey, M. T. (2010). Morphodynamics of subaqueous levee formation: Insights into river mouth morphologies arising from experiments. *Journal of Geophysical Research: Earth Surface*, *115*(F4), doi:10.1029/2010JF001684.

Ruggiero, P., Gelfenbaum, G., Sherwood, C. R., Lacy, J., & Buijsman, M. C. (2003). Linking nearshore processes and morphology measurements to understand large scale coastal change. In *Proceedings of Coastal Sediments '*03. ASCE Press.

Ruggiero, P., Walstra, D. J. R., Gelfenbaum, G., & Van Ormondt, M. (2009). Seasonal-scale nearshore morphological evolution: field observations and numerical modelling. *Coastal Engineering*, *56*(11), 1153-1172, doi:10.1016/j.coastaleng.2009.08.003.

Saint-Venant, A.J.C. de. (1871). Théorie du mouvement non permanent des eaux, avec application aux crues des rivières et à l'introduction de marées dans leurs lits. *Comptes rendus des seances de l'Academie des Sciences*, *36*, 174-154.

Scheffer, M. (2010). Complex systems: foreseeing tipping points. *Nature*,*467*(7314), 411-412.

Schlichting, H. (1968). Boundary-layer theory. Engineering Technology & Applied Sciences, *23*, 12 pp.

Sha, L. P. (1989). Variation in ebb-delta morphologies along the West and East Frisian Islands, The Netherlands and Germany. *Marine Geology*, *89*(1), 11–28.

Sherwood, A. M., & Nelson, C. S. (1979). Surficial sediments of Raglan harbour. *New Zealand Journal of Marine and Freshwater Research*, *13*(4), 475-496.

Sherwood, C. R., Gelfenbaum, G., Howd, P. A., & Palmsten, M. L. (2001). Sediment transport on a high-energy ebb-tidal delta. In *Proceedings of Coastal Dynamics* (Vol. 1, pp. 473-482).

Shi, F., Hanes, D. M., Kirby, J. T., Erikson, L., Barnard, P., & Eshleman, J. (2011). Pressure-gradient-driven nearshore circulation on a beach influenced by a large inlet-tidal shoal system. Journal of Geophysical Research C: Oceans, 116(4) doi:10.1029/2010JC006788

Soulsby, R. L. (1987). Calculating bottom orbital velocity beneath waves. *Coastal Engineering*, 11(4), 371–380.

Soulsby, R. (1997). *Dynamics of marine sands: a manual for practical applications*. Thomas Telford, London.131pp.

Soulsby, R. L., & Clarke, S. (2005). Bed shear-stresses under combined waves and currents on smooth and rough beds. *HR Wallingford, Report TR137*, 52 pp.

Spiers, K. C., Healy, T. R., & Winter, C. (2009). Ebb-Jet dynamics and transient eddy formation at Tauranga Harbour: Implications for entrance channel shoaling. *Journal of Coastal Research*, *25(1)*, 234–247.

Spydell, M., Feddersen, F., Olabarrieta, M., Chen, J., Guza, R.T., Raubenheimer, B., & Elgar, S. (2014). Observed and modelled drifters at a tidal inlet. J*ournal of Geophysical Research, sub judice.*

Stolzenbach, K. D., & Harleman, D. R. (1971). Analytical and experimental investigation of surface discharges of heated water. Report PB-210134; W-72-09729; EPA-WQO-16130-DJU-02/71.

Massachusetts Inst. of Technology, Ralph M. Parsons Lab., Water Resources and Hydrodynamics, Dept. Civil Engineering Rept. 135, 212pp.

Syvitski, J. P., & Saito, Y. (2007). Morphodynamics of deltas under the influence of humans. *Global and Planetary Change*, *57*(3), 261–282.

Tennyson, A. (1889).*Crossing the Bar.* In: Ricks, C., editor.*Tennyson: A Selected Edition*. London: Pearson Education Ltd; 2007. p.665-66.

Thornton, E. B., & Guza, R. T. (1983). Transformation of wave height distribution. *Journal of Geophysical Research: Oceans, 88*(C10), 5925–5938.

Thornton, E.B., & Kim, C.S., (1993). Longshore current and wave height modulation at tidal frequency inside the surf zone. *Journal of Geophysical Research, 98*(C9): 16509–16519.

Traykovski, P. (2007). Observations of wave orbital scale ripples and a nonequilibrium time-dependent model. *Journal of Geophysical Research: Oceans (1978–2012)*, *112*(C6).

USACE (2012). Evaluation Report: Mouth of the Columbia River Jetty Rehabiliation, Executive Report. 5 pp. Accessed online 11 Feb 2015at URL http://www.nwp.usace.army.mil/Portals/24/docs/projects/MCR_Report_Exec_Summary.pdf.

van de Lageweg, W. I., Bryan, K. R., Coco, G., & Ruessink, B. G. (2013). Observations of shoreline–sandbar coupling on an embayed beach. doi:10.1016/j.margeo.2013.07.018

van der Vegt, M., Schuttelaars, H. M., & de Swart, H. E. (2006). Modelling the equilibrium of tide-dominated ebb-tidal deltas. *Journal of Geophysical Research: Earth Surface*, 111(F2), doi:10.1029/2005JF000312.

Van Dongeren, A., Plant, N., Cohen, A., Roelvink, D., Haller, M. C., & Catalán, P. (2008). Beach Wizard: Nearshore bathymetry estimation through assimilation of model computations and remote observations. *Coastal Engineering*, *55*(12), 1016-1027.

van Leeuwen, S. M., van der Vegt, M., & de Swart, H. E. (2003). Morphodynamics of ebb-tidal deltas: a model approach. *Estuarine, Coastal and Shelf Science*, *57*(5), 899-907.

van Rijn, L. C. (1984). Sediment transport, part III: bed forms and alluvial roughness. *Journal of hydraulic engineering*, *110*(12), 1733-1754.

van Rijn, L. C. (1990). *Principles of fluid flow and surface waves in rivers, estuaries, seas and oceans* (Vol. 11). Amsterdam, The Netherlands: Aqua Publications.

van Rijn, L. C. (2007). Unified view of sediment transport by currents and waves. I: Initiation of motion, bed roughness, and bed-load transport. *Journal of Hydraulic Engineering*, *133*(6), 649-667.

van Rijn, L. C., Roelvink, J. A., & Horst, W. T. (2001). Approximation formulae for sand transport by currents and waves and implementation in DELFT-MOR. Deltares (WL). 44 pp.

van Rijn, L. C., Walstra, D. J. R., Grasmeijer, B., Sutherland, J., Pan, S., & Sierra, J. P. (2003). The predictability of cross-shore bed evolution of sandy beaches at the time scale of storms and seasons using process-based profile models. *Coastal Engineering*, *47*(3), 295–327.

Waikato Regional Council (2013). *Bar crossings*. Retrieved May 1, 2015, from http://www.waikatoregion.govt.nz/barcrossing/

Walton, T. L., & Adams, W. D. (1976). Capacity of inlet outer ears to store sand. *Coastal Engineering Proceedings*, *1*(15).

Wargula, A., Raubenheimer, B., & Elgar, S. (2014). Wave-driven along-channel subtidal flows in a well-mixed ocean inlet. *Journal of Geophysical Research: Oceans*, 119, doi:10.1002/2014JC009839.

Whitehouse, R. J., Soulsby, R. L., Roberts, W., & Mitchener, H. J. (2000). Dynamics of estuarine muds. 210 pp.

Winter, C. (2007). On the evaluation of sediment transport models in tidal environments. *Sedimentary Geology*, *202*(3), 562–571.

Wood, A. (2010). Episodic, seasonal, and long term morphological changes of Coromandel beaches. University of Waikato Masters Thesis (Marine Science), Hamilton, New Zealand.

WRAPS (2012). Imagery sourced from Waikato Regional Council. © Waikato Regional Aerial Photography Service (WRAPS) 2012. Licensed for re-use under the Creative Commons Attribution 3.0 New Zealand license. URL: http://www.waikatoregion.govt.nz /Environment/Environmental-information/REDI/2310412/

WRC (2011). LiDAR Data. © Waikato Regional Council & NZ Aerial Mapping Ltd 2010 – 2011. Licensed for limited use under licence agreement EWDOC#3029206/v2 between Waikato Regional Council, University of Waikato, and Shawn R Harrison.

Wright, L. D. (1977). Sediment transport and deposition at river mouths: a synthesis. *Geological Society of America Bulletin*, *88*(6), 857–868.

Wright, L. D., & Short, A. D. (1984). Morphodynamic variability of surf zones and beaches: A synthesis. Marine Geology, 56(1), 93-118. doi:10.1016/0025-3227(84)90008-2

Zippel, S. and Thomson, J. (2015). Wave breaking and turbulence at a tidal inlet. *Journal of Geophysical Research: Oceans*, *120(2)*, doi:10.1002/2014JC010025.